Chem Soc Rev

Atomically Dispersed Metal-Nitrogen-Carbon Catalysts for Fuel Cells: Advances in Catalyst Design, Electrode Performance, and Durability Improvement.

Journal:	*Chemical Society Reviews*
Manuscript ID	CS-REV-12-2019-000903.R1
Article Type:	Review Article
Date Submitted by the Author:	30-Mar-2020

Complete List of Authors:	He, Yanghua; University at Buffalo, SUNY, Chemical and Biological Engineering Liu, Shengwen; University at Buffalo - The State University of New York, Dept of Chemical & Biological Engineering Shi, Qiurong ; University at Buffalo, SUNY, Chemical and Biological Engineering Priest, Cameron ; University at Buffalo - The State University of New York, Dept of Chemical & Biological Engineering Wu, Gang; University at Buffalo, SUNY, Chemical and Biological Engineering

Atomically Dispersed Metal-Nitrogen-Carbon Catalysts for Fuel Cells: Advances in Catalyst Design, Electrode Performance, and Durability Improvement

Yanghua He[1], Shengwen Liu[1], Cameron Priest, Qiurong Shi*, and Gang Wu*

Department of Chemical and Biological Engineering, University at Buffalo,

The State University of New York, Buffalo, NY 14260, United States

Corresponding authors: qiurongs@buffalo.edu (Q. Shi) and gangwu@buffalo.edu (G. Wu)

[1] These two authors contributed equally

Abstract. The urgent need to address the high-cost issue of proton-exchange membrane fuel cell (PEMFC) technologies, particularly for transportation applications, drives the development of simultaneously highly active and durable platinum group metal-free (PGM-free) catalysts and electrodes. The past decade has witnessed remarkable progress in exploring PGM-free cathode catalysts for the oxygen reduction reaction (ORR) to overcome sluggish kinetics and catalyst instability in acids. Among others, scientists have identified the newly emerging atomically dispersed transition metal (M: Fe, Co, or/and Mn) and nitrogen co-doped carbon (M-N-C) catalysts as the most promising alternative to PGM catalysts. Here, we provide a comprehensive review of significant breakthroughs, remaining challenges, and perspectives regarding the M-N-C catalysts in terms of catalyst activity, stability, and membrane electrode assembly (MEA) performance. A variety of novel synthetic strategies demonstrated effectiveness in improving intrinsic activity, increasing active site density, and attaining optimal porous structures of catalysts. Rationally designing and engineering the coordination environment of single metal MN_x sites and their local

structures are crucial for enhancing intrinsic activity. Increasing the site density relies on the innovative strategies of restricting the migration and agglomeration of single metal sites into metallic clusters. Relevant understandings provide the correlations among the nature of active sites, nanostructures, and catalytic activity of M-N-C catalysts at the atomic scale through a combination of experimentation and theory. Current knowledge of the transferring catalytic properties of M-N-C catalysts to MEA performance is limited. Rationally designing morphologic features of M-N-C catalysts play a vital role in boosting electrode performance through exposing more accessible active sites, realizing uniform ionomer distribution, and facilitating mass/proton transports. We outline future research directions concerning the comprehensive evaluation of M-N-C catalysts in MEAs. The most considerable challenge of current M-N-C catalysts is the unsatisfied stability and rapid performance degradation in MEAs. Therefore, we further discuss practical methods and strategies to mitigate catalyst and electrode degradation, which is fundamentally essential to make M-N-C catalysts viable in PEMFC technologies.

Keywords: Single metal site catalysts; oxygen reduction reaction; PGM-free electrocatalysis; electrode design; proton-exchange membrane fuel cells

1. Introduction

The increasing demands for electric vehicles (EVs) and mobile devices have garnered a consistently growing interest in the development of durable and low-cost energy power sources with high energy and power densities. Compared to traditional Li-ion batteries, proton-exchange membrane fuel cells (PEMFCs), which generate electricity by using redox reactions involving hydrogen and oxygen (air), have many standing advantages of high efficiency, high power/energy density, fast refueling, and zero carbon emissions.[1-5] The current performance of PEMFCs is insufficient yet for widespread use, which is limited primarily by the fuel cell's cathode for the oxygen reduction reaction (ORR). The ORR is kinetically sluggish, especially at low-pH environments, and relies heavily on the use of platinum-group metal (PGM) based catalysts. These PGMs make fuel cell electric vehicles (FCEVs) very expensive and, therefore, not yet competitive with battery-based EVs and internal combustion engine vehicles. The U.S. Department of Energy (DOE) set an ultimate cost target of US$30/kW to make FCEVs more economically feasible. The utmost goal is to significantly reduce PGM loadings while maintaining sufficient activity, durability, and power density. Although encouraging progress has been made in the past few decades in developing a variety of innovative low-PGM catalysts and electrodes to address the high cost of PEMFCs,[6-12] it would be ideal for exploring completely PGM-free cathode catalysts for large-scale and sustainable applications of PEMFCs in the future.[13-16] Therefore, PGM-free ORR catalysts represent a high-reward research approach to PEMFCs in the long term.[17-22] In addition to the cost-effectiveness, unlike PGM catalysts, PGM-free catalysts are highly tolerant of nearly all contaminants and impurities (*e.g.*, alcohols and other organics, ammonia, carbon monoxide, sulfur oxides) commonly found in fuel cell hardware and air feed streams.[23, 24] PGM-free active sites have no affinity to large quantities of various contaminants, and their ORR activity

does not change significantly. Thus, when compared to traditional PGMs, PGM-free cathodes are also expected to be more suitable for using alternative fuels, instead of pure H_2, such as methanol, ethanol, or ammonia in fuel cells.[25, 26]

A variety of PGM-free catalyst formulations have been studying for a few decades. Macrocyclic compounds such as metal phthalocyanine were initially found active toward the ORR in the 1960s.[27] Then high-temperature pyrolysis approaches were discovered in the 1970s to be effective for significant improvements of activity and stability for these macrocyclic-derived catalysts in acids.[28-32] In the first decade of 2000, instead of expensive metal-macrocyclic, common nitrogen-containing precursors, inorganic metal sources, and high-surface-area carbon supports were explored to prepare metal and nitrogen co-doped carbon (M-N-C) catalysts, which showed significantly enhanced catalytic performance.[33-35] Among the studied metals (M), Fe is the most active metal species used in M-N-C catalysts, followed by Co and Mn.[35-39] Selections of nitrogen, carbon, and metal precursors are crucial for performance improvement during the synthesis. In particular, structurally and chemically defined metal-organic frameworks (MOFs) simultaneously consist of three key components (*i.e.*, N, C, and M). Therefore, scientists recently explored them as effective precursors to yield atomically dispersed and nitrogen-doped single metal active sites that can be stabilized by carbon supports with homogeneous morphologies.[22,40,41] These unique features are responsible for significant performance improvements of M-N-C catalysts for the ORR in challenging acidic media.[22,41,42] Advances in catalyst characterization techniques such as high-resolution electron microscopy and X-ray absorption spectroscopy are critical for identifying atomically dispersed and nitrogen coordinated metal sites (*e.g.*, FeN_4, CoN_4, MnM_4) in M-N-C catalysts. Elucidating insightful understanding of the active site structure and reaction pathway, therefore, becomes possible. However, to replace PGM catalysts,[43-45] continuous advancements of

M-N-C catalysts are highly demanded by simultaneously enhancing intrinsic activity (*i.e.*, TOF) of MN_4 active sites and increasing their site density. In particular, designing optimal precursors combined with favorable thermal activation and post-treatments are effective to engineer coordination environments of MN_4 active sites for improved intrinsic activity.[46-48] Catalyst morphology optimizations in nanostructures, porosities, surface areas can increase the density of active sites and facilitate mass transport.[18, 42, 46, 49] Importantly, the structurally defined isolated single metal atoms with homogeneous morphologies can be characterized as model systems for fundamental investigations on active sites and reaction mechanisms to establish a correlation between catalyst structures and properties.[19, 35, 48, 50-55]

In this review, we firstly highlight effective synthetic approaches to enhancing the intrinsic and mass activities of M-N-C catalysts. Specifically, four approaches are effective to enhance the intrinsic activity of the catalysts: (i) regulating the local coordination structure of center metals, (ii) adjusting their electronic structures by doping of light heteroatoms, (iii) integrating dual-atom or multi-atom metal sites, and (iv) creating more edge hosted active MN_4 sites. Besides, recent successes in improving mass activity via populating the density of single metal active sites focus on precursor design and subsequent thermal activation, which include chemical M-N bonding formation, the coordination effect, the spatial confinement effect, and porosity engineering. Combined with accurate characterization and theoretical simulations, fundamental understandings of synthesis-structure-property correlation are essential to lay a solid foundation for developing high-performance M-N-C catalysts through the rational design of precursors and synthetic methods.[20, 56-59]

For desirable M-N-C catalysts in MEA electrodes, abundant micropores are essential for hosting active sites and thus achieving high catalytic activity.[57, 60] In contrast, sufficient mesopores

and macropores are imperative to ensure effective ionomer distribution for mass transfer of reactants (O_2 and H^+) and product (H_2O).[61, 62] Herein, the importance of rationally controlling catalyst morphologies with optimal porosity and nanostructure is emphasized on the optimization of the interfacial properties between catalysts and ionomers to create efficient three-phase interfaces.[63-65] Insufficient knowledge regarding the assembly of M-N-C catalysts into electrodes primarily limits the performance of MEAs for practical PEMFC applications. Optimization of electrode structures requires not only experiments but also multiple-scale modeling and high-resolution characterization. Relative to traditional PGM catalysts, the active site density in these M-N-C PGM-free catalysts is much lower and turns out much thicker electrode layers (*e.g.*, ~100 μm), in turn limiting high current density operation and causing challenging mass transport and water management.[66-68] Therefore, one of the important topics is to review recent progress in designing, elucidating, and diagnosing electrode structures. The proper understanding can guide the fabrication of high-performance MEAs.[68, 69] Significant progress demonstrated encouraging beginning-of-life (BOL) MEA performance.[17, 60, 70] However, improving long-term stability through understanding possible degradation mechanisms of the M-N-C electrode is still fledgling, especially during operando operation conditions. PGM-free cathodes only demonstrated performance durability for hundreds of hours at relatively low voltages (*i.e.*, 0.4 V),[55] which is not sufficient for transportation applications. Herein, durability studies are crucial for M-N-C catalyst development, which is discussed, including possible degradation mechanisms and strategies. In this work, we provided a comprehensive review for the most promising atomically dispersed single metal site M-N-C catalysts from rational catalyst design and synthesis to electrode optimization for performance and durability in MEAs by levering our more than 15-years of research experience in the field.

2. Strategies to improve catalyst activity

Atomically dispersed single metal site M-N-C catalysts are recently emerging as a new frontier in the electrochemical field due to their unique electronic structures and intrinsic catalytic activity for many reactions.[53] However, compared to traditional PGM catalysts, current M-N-C catalysts have insufficient catalytic activity and stability for viable applications in fuel cells. One of the challenging issues is the generally low density of isolated metal active sites (less than 3 at.%), significantly hindering their practical applications. Increasing the density of the active site faces the challenges that isolated metal atoms migrate and agglomerate to form metal nanoparticles and compounds due to their high surface energy and the lack of stabilizing ligands. Another serious concern is the insufficient stability of M-N-C catalysts for long-term operation durability. Highly active catalysts often suffer from rapid degradation during the ORR, possibly due to the metal dissolution and carbon corrosion under the oxidative electrochemical environments. Moreover, although MN_4 sites are the universal active sites for the ORR, the catalytic mechanisms and reaction pathways are primarily dependent on the metal centers, heteroatom dopants, coordination environments, and reaction conditions (*e.g.*, pH and potential values). The field still lacks relevant knowledge on how to further enhance their intrinsic activity and stability by modulating coordination environment, local structures, and supporting carbon matrix. Here, we summarize recent advances of the atomically dispersed M-N-C catalysts with special emphasis on the understanding of coordination environments engineering and single metal site stabilization during the synthesis.

2.1 Improving the intrinsic activity of MN_4 sites

Generally, adsorption energies between single metal sites and O_2/intermediates are crucial for reaction activity and selectivity.[71-74] Different theoretical research groups have proposed the most

likely ORR pathways on such single metal sites in acidic media.[75-77] Firstly, an O_2 molecule is chemically adsorbed on an MN_4 active site, followed by the first protonation step to form OOH*. Then the O=O bond scission is likely to produce O* and OH* species adsorbing on metal sites and the adjacent carbon or nitrogen sites, respectively. The second protonation step would further convert OH* to the first H_2O. Meanwhile, the O* proceeds protonation steps and eventually form the second H_2O. Depending on whether the breaking of the O=O bond of OOH* species or not, the ORR proceeds the two- and four-electron pathways and generates detrimental H_2O_2 or desirable H_2O, respectively. Among these elemental steps, the OOH* dissociation is the possible rate-determining step (RDS) due to the relatively high activation energies. Also, according to the Sabatier principle, the adsorption of ORR intermediates on active sites should be "just right," neither too strong nor too weak. Similar to Pt sites, such adsorption on the best performing FeN_4 sites is still too strong, while maybe too weak for CoN_4 sites. Therefore, tuning the electron density and geometry of the metal center and their local coordination structure is of great significance to modulate the adsorption energies of O_2 and other intermediates.[76, 78-84]

Although many M-N-C catalysts exhibited promising catalytic activity for the ORR,[24, 83, 85-89] the discovery and further realization of advanced catalysts are often empirical rather than rational design. Fundamental principles to guide compositional control and synthesis optimization seriously lack.[90] Many fundamental questions are still unresolved, which hinders the catalyst advancements. For example, (i) it is not fully understood yet how these MN_4 sites form during the necessary thermal activation process; (ii) how do the MN_4 coordination chemistry, bonding, surrounding local carbon structures, and chemical environment affect their catalytic activity, reaction selectivity, and stability; (iii) how does O_2 adsorb on MN_4 sites for subsequent electron transfer, protonation, and bond-breaking; (iv) how do the reaction intermediates desorb as

functions of applied potentials, pH values, and temperatures; (v) what are the possible degradation mechanisms during the ORR at different potentials and pH environments. Hence, combined approaches, including theoretical computation, judicious materials synthesis, high-resolution structural characterization, and high-fidelity property measurements, are crucial for providing knowledge to modulate the electronic and geometric properties of atomically dispersed M-N-C catalysts for enhanced intrinsic activity.

2.1.1 Coordination and local structure of the metal center

DFT calculations have predicted the most active and stable active sites in the M-N-C catalysts. In principle, the active sites associated with FeN_x moieties have five possible coordination numbers with x = 1 to 5. The coordination number x significantly affects the charge distribution of the active site, thus resulting in the alteration of catalytic properties of M-N-C catalysts.[76, 86, 91-97] The theoretical calculation predicted the optimized adsorption configurations of ORR intermediates O*, OH*, and OOH* on FeN_x (x = 1–5). FeN_4 has the smallest free energy for the ORR limiting step, which stems from appropriate adsorption of OH* on FeN_4 and the easy desorption of H_2O from FeN_4. The order of ORR activity is theoretically determined to be $FeN_4 > FeN_3 > FeN_2 > FeN_1 > FeN_5$. Therefore, desirable Fe-N-C catalysts should contain dominant FeN_4 sites with a four-fold coordination number stabilized in carbon planes.

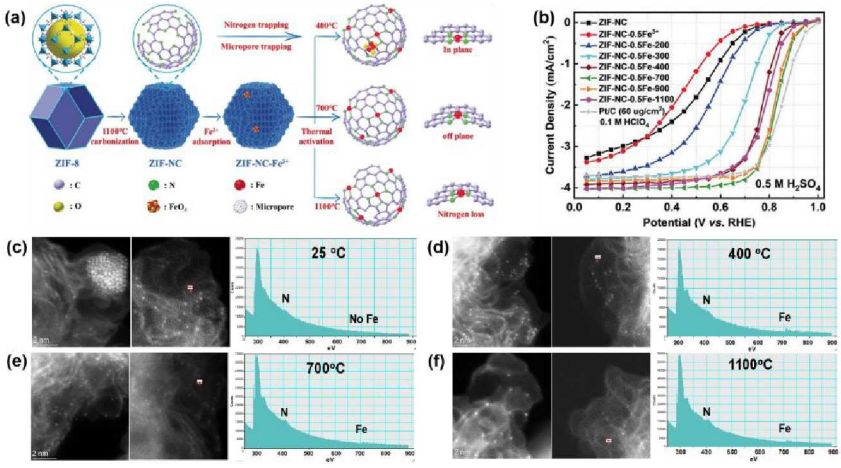

Fig. 1. (a) Schematic illustration of the Fe-N bond formation process by adsorbing Fe into ZIF-8-derived N-doped carbon. (b) the ORR activity of the catalysts obtained in different stages and pyrolysis temperatures. (c-f) Morphology and atomic structure of Fe-N-C catalyst treated at various temperatures. Reproduced with permission.[91] Copyright 2019, Wiley-VCH.

In prior studies, the specific feature of active sites cannot be identified experimentally and characterized. Because, most of the Fe-N-C catalysts developed in the early stage are highly heterogeneous containing multiple Fe species such as metallic Fe, oxides, carbides, or sulfides.[98-100] Due to recent advances of M-N-C catalysts embedded with monodispersed single Fe site without Fe aggregates,[85, 101] advanced characterization techniques verified the dominant existence of FeN_4 sites in highly active Fe-N-C catalysts by using X-ray absorption near-edge structure (XANES), Mößbauer Spectroscopy, and visualized with aberration-corrected scanning transmission electron microscope (STEM) coupled with atomic-level electron energy loss spectroscopy (EELS).[24, 101] However, elucidating the formation mechanisms of FeN_4 active sites remains elusive for a few decades. The reason is due to the complex Fe-N bond formation process during high-temperature pyrolysis, simultaneously, along with the uncontrolled occurrence of

carbonization and nitrogen doping. Well-defined model systems are highly desirable to study the interaction variation between Fe and N atoms during the controlled thermal activation process. Recently, we found that ZIF-8-derived nitrogen-doped carbon with controllable nitrogen doping, carbon structure, and porosity is an ideal carbon matrix for investigating the FeN_4 formation mechanism. The high temperature (1100 ^oC) pyrolysis of ZIF-8 produces stable carbon structures and nitrogen dopants, which can remain identical during the subsequent thermal activation. Therefore, adsorbing Fe^{3+} ions into this carbon host can study the FeN_4 site formation process as a function of heating temperatures (**Fig. 1a**).[91] The evolution of Fe-N bond interactions can link to experimentally measured catalytic activity (**Fig. 1b**) and structural characterization.[91] One of the significant discoveries is that active Fe-N bonds can form at a relatively low temperature of 400 $^\circ C$, as evidenced in XAS analysis along with the STEM/ EELS mapping (**Fig. 1c-f)**. This new understanding updated the previous knowledge of the formation of active Fe-N bond at a higher temperature over 800 $^\circ C$.[2, 85, 102, 103] Ultrafine Fe-oxide nanoparticles with a size typically less than 2 nm formed after the adsorption step at room temperature, but able to gradually disappear over 400 ^oC. Because the FeO_x nanoparticles anchored on the nitrogen-doped carbon can convert into atomically dispersed FeN_4 sites during thermal activation, indicating the feasibility of directly using solid-state FeO*x* precursor for single metal site catalyst synthesis. Even a low temperature of 400 ^oC can generate relatively high activity ($E_{1/2}$ =0.79 V), which can further increase when the temperature rises to 700 ^oC ($E_{1/2}$ =0.83 V). However, the activity is slightly declined at 1100 ^oC due to the loss of nitrogen dopants and reconstruction of carbon structures (**Fig. 1b**). Thus, a temperature at 700 $^\circ C$ leads to optimal FeN_4 sites with a shorter bond length corresponding to enhanced intrinsic activity. Therefore, a concept of strain can uncover the effect of Fe-N bond length on ORR activity based on the XAS analysis. With gradually increasing temperatures, the

carbon layer embedded with FeN_4 sites undergoes off-plane ripples. The subtle change of local carbon structures leads to lower symmetry around Fe atoms, shorter Fe-N bond lengths, and contraction strains of the Fe-N bond in FeN_4 moieties. Theoretical calculation predicted that a small degree of Fe-N bond contraction (-2%) would facilitate O_2 adsorption and the subsequent O=O bond-breaking process during the ORR. However, a significant Fe-N bond contraction (-5%) makes the ORR thermodynamically unfavorable at the FeN_4 site. Hence, the ORR activity increases with temperature up to 700 °C, which is probably due to the optimal Fe-N bond strain (-2%).

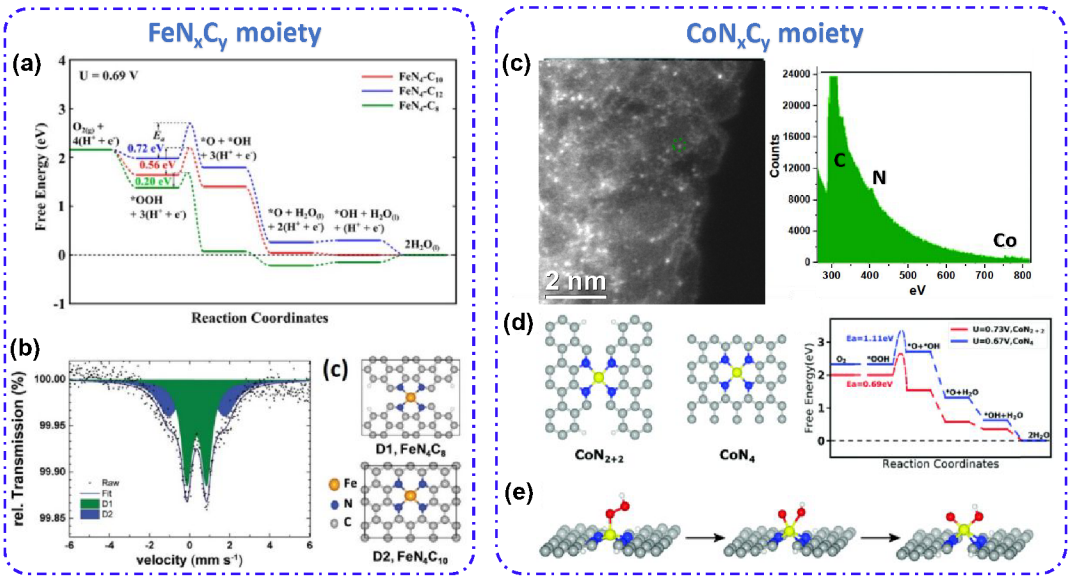

Fig. 2. (a) Free energy diagram of the reduction of O_2 to H_2O through an OOH dissociation pathway on the active sites FeN_4-C_{10}, FeN_4-C_{12}, and FeN_4-C_8 at a temperature of 300 K and under an electrode potential of 0.69 V in acid medium. Reproduced with permission.[76] Copyright 2017, American Chemical Society. (b) Mössbauer spectroscopy of the atomically dispersed Fe catalyst (1.5Fe–ZIF), and the corresponding molecular structure of D1 (FeN_4C_8) and D2 (FeN_4C_{10}).

Reproduced with permission.[101] Copyright 2019, Royal Society of Chemistry. (c) Aberration-corrected MAADF-STEM images and EELS of the best performing Co-N-C catalysts. (d) Atomistic structure and calculated free energy evolution diagram of CoN_{2+2} and CoN_4 active sites in the Co-N-C catalysts. (d) The OOH intermediate adsorption and dissociation on the CoN_{2+2} site. Reproduced with permission.[105] Copyright 2019, Royal Society of Chemistry.

Furthermore, three FeN_4-type active sites with different local carbon structures were theoretically studied **(Fig. 2a)**, including FeN_4-C_8, FeN_4-C_{10}, and FeN_4-C_{12}. The FeN_4 site surrounded by a lower number of local carbon atoms (*i.e.*, the FeN_4-C_8 on the edge of micropores) has the lowest activation energy for the O=O bond breaking and favors a direct four-electron pathway.[48, 76, 106, 107] Consequently, the introduction of micropores in the Fe-N-C catalysts creates optimal local carbon structures. It then generates more FeN_4-C_8 active sites for enhancing intrinsic activity. Experimentally, Mössbauer spectroscopy and XANES can elucidate the local carbon structures of FeN_4 sites, which further link to their intrinsic activity.[86, 89] Especially, ^{57}Fe Mössbauer spectroscopy is the most powerful tool to differentiate FeN_4 species with various local carbon structures in Fe-N-C catalysts. Recently, two types of FeN_4 active sites in an atomically dispersed Fe-N-C catalyst (1.5Fe-ZIF) were identified by using Mössbauer spectroscopy, including FeN_4-C_8 and FeN_4-C_{10}, respectively, as shown in **Fig. 2b**.[101] Concerning their Mössbauer spectrum, D1 is assigned to FeN_{2+2} configuration. Four neighboring nitrogen atoms surround the pseudo-sixfold coordination of Fe in a way that carbon or nitrogen atoms were above and below the graphene planes from the axial direction.[101, 108] D2 is in-plane FeN_4 coordination integrated into graphene layers. D1 may act similarly to FeN_4C_8, where the carbon atoms with dangling bonds adjacent to FeN_4 moieties were the active sites and give rise to the outstanding ORR performance.

It enables the binding of OOH intermediate to facilitate the cleavage of O=O bonds during the ORR, evidencing the FeN_4-C_8 site-rich Fe-N-C catalyst presented exceptional ORR activity (RDE: $E_{1/2}$ = 0.88 V, loading: 0.8 mgcm^{-2}; j = 2.0 mA cm^{-2} at 0.9 V) in acid media. This experimental observation is consistent with the DFT calculations, which verified that the FeN_4-C_8 moiety expected to present higher intrinsic activity than the conventional FeN_4-C_{10} moiety. [76]

In addition to the MN_xC_y geometric configurations, the chemical properties of neighboring nitrogen or carbon atoms around the metal are also crucial in adjusting their intrinsic activities. For instance, the NH_3-pyrolyzed Fe-N-C catalyst exhibited enhanced ORR activity over that of the Ar-pyrolyzed one in spite that they contained identical FeN_4C_{12} moieties.[86] The reason is that the Lewis basicity of NH_3-treated N-doped carbon support promotes the TOF of FeN_4C_{12} moieties. Specifically, the pyrolysis in NH_3 promotes the formation of nitrogen groups with higher basicity in the carbon support. The modification is related to the higher degree of π-electron delocalization and the electron-donating capability of the carbonaceous surfaces.[109] This further optimized the bond strength between the metal center and the ORR intermediates, resulting in higher TOF and intrinsic ORR activity of FeN_4C_{12} moieties. This knowledge inspired researchers to explore new approaches in preparing highly active M-N-C catalysts by further introducing new functional groups around the metal active sites.[51, 80, 110-115]

Although Fe-N-C catalysts exhibited the best performance among studied PGM-free catalysts, a significant concern of Fe-N-C catalysts is the Fenton reactions between Fe^{2+} and H_2O_2. Essentially, H_2O_2 is an inevitable by-product or intermediate during the ORR. Thus, the as-produced radicals, including hydroxyl and hydroperoxyl groups, would cause the degradation of organic ionomer and membranes along with catalysts themselves in fuel cell electrodes.[116] To address this issue, strategies for mitigation of the Fenton reactions of Fe-N-C catalysts or

developing Fe- and PGM-free catalysts are highly desirable. Like FeN_4 sites, CoN_4 and MnN_4 sites are also active sites toward ORR with alleviated Fenton reactions.[13, 116] However, such Co- and Mn-N-C catalysts often exhibited relatively low kinetic activity. Similar to Fe-N-C catalysts, modifying the coordination numbers and local carbon structures of CoN_x or MnN_x moieties are capable of enhancing the catalytic activity of catalysts.[16, 113, 117-120] With a similar chemical doping method, we prepared a Co-N-C catalyst enriched with anatomically dispersed CoN_4 sites. The Co-N coordination was observed for the first time by advanced HAADF-STEM images coupled with EELS (**Fig. 2c**).[104] The conventional CoN_4 site embedded in the intact graphitic layer cannot effectively catalyze the $4e^-$ ORR due to its ultra-high activation energy barrier for O=O bond-breaking.[91] However, the CoN_{2+2} sites with local carbon defects similar to D1 structures bridging over two adjacent armchair graphitic edge are more active for the ORR (**Fig. 2d**).[119] The calculated activation energy for the critical OOH dissociation on the Co-N_{2+2} site was similar to that of FeN_4, suggesting that the Co-N_{2+2} site was thermodynamically favorable for the $4e^-$ ORR pathway (**Fig. 2d** and **e**).[119] In turn, the high selectivity of the four-electron pathway would be beneficial for catalyst stability enhancement, which is discussed later in the next section.

In summary, advanced characterization techniques and the theoretical calculations have identified the MN_x moieties as the active sites toward ORR electrocatalysis. The geometric configurations, including the coordination environment of metal centers and the chemical feature of the nitrogen/carbon atoms, are crucial for adjusting their intrinsic activity. Because they modify the adsorption and desorption energies toward ORR intermediates.[101, 105] The evolution of Fe-N bond formation is dependent on pyrolysis temperatures, which can be unveiled via the delicately designed experiment. The relevant studies have updated our knowledge in Fe-N-C catalysts synthesis and would guide further engineering of highly efficient M-N-C catalysts.[91]

2.1.2 Doping light heteroatoms

As we stated in the previous subsection, FeN_4 moieties hosted in the carbon matrix are the active site for the ORR in acid media. However, the interaction between FeN_4 sites and ORR intermediates are still too strong based on theoretical predictions. Thus, there is still much room for further improving the intrinsic ORR activity by regulating the electronic structure of FeN_4 active sites to weaken the interaction between FeN_4 active sites and ORR intermediate.[83, 121, 122] Recently, incorporation of light heteroatoms such as sulfur (S),[82, 123-126] and phosphorus (P)[127, 128] into M-N-C catalysts is an effective strategy for addressing this issue.[129] Like N atoms, both S and P atoms are classified as the p-block elements. However, S and P atoms have a larger atomic radius and lower electronegativity than that of N.[130] Thus, their dopings into the carbon matrix favor the formation of structural defects on the sp^2 carbon. They can further adjust the electronic property of MN_x sites.

As an example, Fe single sites on S and N co-doped carbon (Fe/SNC) with controllable S, N doping was synthesized through pyrrole-thiophene copolymer pyrolysis strategy.[78] The S/N ratio is tunable by changing the feeding ratio of polymeric monomers. The optimized Fe/SNC catalyst with an S/N ratio of 1:1 exhibited superior ORR activity to that of Fe single sites on N-doped carbon without S doping. Based on XAFS analysis and DFT calculation, the improved ORR activity is originated from the incorporation of low relative electronegativity of S, facilitating the rate-limiting reductive release of ORR intermediates. Also, using $Fe(SCN)_3$ precursors can produce an S-doped Fe-N-C catalyst with nearly a twofold increase of ORR activity in acidic electrolyte than that of a Fe-N-C catalyst without S doping.[82] Several other works also validated that the introduction of S can effectively enhance the ORR activity of Fe-N-C catalysts. The

primary reason is due to the reduced electron localization around FeN_4 active sites, leading to an optimized electronic structure for the ORR.[81, 131-135]

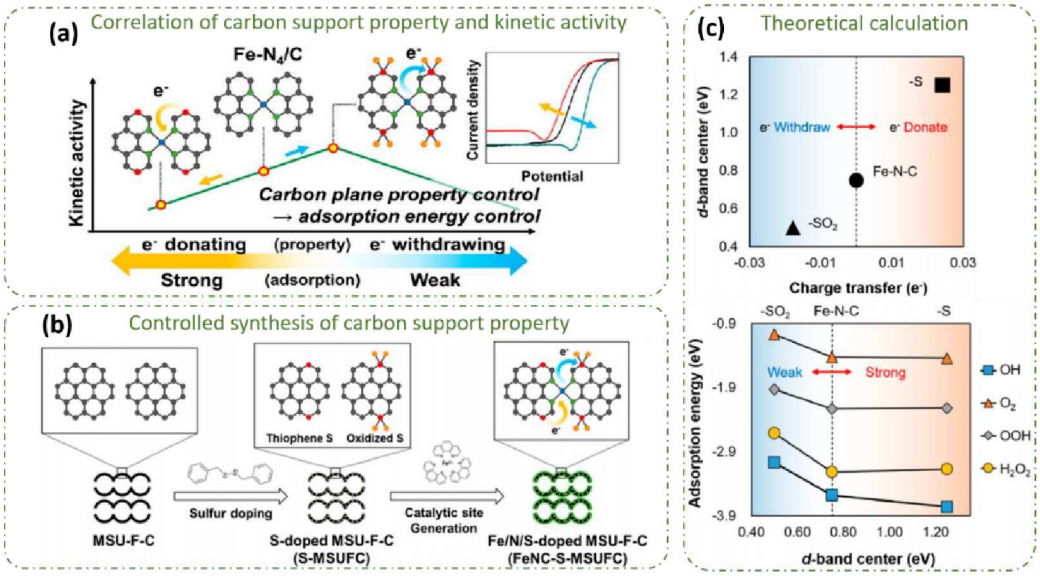

Fig. 3. (a) The design strategy for tuning the kinetic activity of a single Fe-N_4 site by regulating the electron-withdrawing/donating properties of a carbon plane via incorporation of different sulfur functionalities. (b) Schematic presentation of the synthesis process of thiophene S and oxidized S doped Fe-N-C catalysts. (c) Correlation of d-band center and charge transfer amount of different functional groups (upper), and the relationship of the ORR intermediates adsorption energy and the d-band center (lower). Reproduced with permission.[79] Copyright 2019, the American Chemical Society.

Most of the recent studies on heteroatom-doped Fe-N-C catalysts for promoting intrinsic ORR activity are on the manipulation of the configuration of the active site for tailoring the adsorption/ desorption energy of the ORR intermediates. However, tailoring the kinetic activity of each FeN_4 active site (*i.e.,* the electron transfer rate during the reaction) has been rarely reported. A few

studies provided insights into the understanding and regulation of the kinetic activity of a single FeN_4 site.[79, 83] Ramaswamy *et al.*[83] presented the structure-activity relationship between the intrinsic ORR activity and surface property of the Fe-N_4 catalyst. They proposed that it is the electron-withdrawing/donating capability of the carbon support endowed by the delocalized π-electrons that governs ORR activity on FeN_4 active sites. The incorporation of the FeN_4 active site leads to a significant perturbation of the π-electron system in the carbon basal plane. In turn, the graphite ligand environment featured with electron-withdrawing property gives rise to an anodic shift in the redox potential of the metal ion, corresponding to a higher ORR onset potential. Experimentally, FeN_x sites can anchor onto various carbon supports (graphite, acetylene black, super-P, activated carbon, Ketjen EC600JD, and black pearl) with diverse delocalized π- electron system in the carbon basal plane. Highly ordered carbon supports such as acetylene black, graphite, and super-P yield lower TOF due to their electron-donating property and the accumulation of a higher electron density at the metal center. Thus, the resultant strong bond strength between the ORR intermediates and metal center generate a smaller TOF value. On the contrary, highly disordered carbon supports such as Ketjen black (EC600JD), activated carbon, and BlackPearl with electron-withdrawing property decrease the electron density and a downshift of the e_g-orbital, thus remarkably enhancing the ORR. Motivated by this, a new and intuitive strategy for regulating the kinetic activity of a single FeN_4 site was developed by controlling electron-withdrawing/donating properties of a carbon plane with S functionalities incorporated (**Fig. 3a**).[79] In the controlled synthesis, dibenzyl disulfide (DBDS) and $Fe(phen)_3Cl_2$ are S-dopant and FeN_4 site precursors, respectively **(Fig. 3b)**. Fe-N-C catalysts functionalized with S have tunable ratios between oxidized- and thiophene-like S. In particular, thiophene-like S with lone pair of electrons makes it a strong electron donor to the carbon plane, leading to the upshift of the d-band center

and increased adsorption energies toward ORR intermediates on the FeN_4 sites (**Fig. 3c**). In contrast, oxidized S functionalities such as a sulfone or sulfonyl group endow an electron-withdrawing effect on the π- electron band in the carbon plane. The lowered *d*-band center of the Fe ion by withdrawing electrons from the FeN_4 site results in decreased adsorption energies toward ORR intermediates on the FeN_4 sites. Therefore, the oxidized S functionalities with electron-withdrawing property on the carbon plane of Fe-N-C catalysts accelerated the reaction rates and hence enhanced the kinetic activity. The above hypothesis was further validated by the increased ORR catalytic activity of Fe-N-C catalysts with a higher oxidized S/thiophene-like S ratio. These results imply the importance of modulating the electronic properties of the carbon plane *via* heteroatom dopants.

Despite that, the S doping leads to encouraging activity improvement. Still, the major limitation is that the number of doping sites because S atoms usually are doped at the edge sites or defects.[136] Also, the possibility of active sites poison by S species remains misty.[133] Whereas, P atoms could be quickly introduced to the carbon matrix via substituting an arbitrary carbon atom.[137, 138] Introduction of P dopants into M-N-C materials is another way of improving the intrinsic activity of MN_x sites.[136, 139,140] The synergistic coupling effect between CoN_4 active sites and P atoms can promote O_2 chemisorption, and thus facilitating the ORR catalysis in alkaline electrolytes.[139] Boron and chloride doped M-N-C catalysts also showed the potential for improving intrinsic activity.[78, 140, 141] Hence, heteroatom dopings are effective to tune electronic and geometric structures of metal centers and their local carbon structures. Also, such appropriate doping can further modify carbon morphologies, including surface area, pores structure, and hydrophilicity. It should be pointed out that valid evidence for identifying the multiple heteroatom dopings in terms of their position and content, along with the exact roles in altering ORR activity, is still absent.

Aside from the heteroatom doping method, tailoring the carbon plane size is another way for promoting the kinetic activity of the incorporated FeN_4 active sites. The underling promotion mechanism is similar to heteroatom doping for regulating the localized electron density. The small carbon plane (edge sites, defects, heteroatoms) usually affects the high degree of electron-delocalization and -donating capability. Because FeN_4 active sites hosted in these small carbon planes generally induce a speeded ORR process yet a sharp activity degradation. The observation is consistent with recent reports [24, 142,143] that the size of the carbon plane is one of the critical factors for regulating the kinetic activity of the FeN_4 site.[83,144] However, it is still a bottleneck for obtaining the well-defined carbon plane size, though several promising strategies can control the activity of the FeN_4 site.[145-147] Here, introducing heteroatoms into M-N-C catalysts or well-tailored carbon plane size is capable of boosting the ORR kinetic activity of the FeN_4 sites, which originated from the as-induced electronic effect between carbon plane and metal atoms.

2.1.3 Dual/multi-metal sites

The adsorption of O_2 molecule onto a single-atom site is either through a side-on or end-on model, whereas on a dual- or multi-atom site, O_2 tends to adsorb by a bridge-*cis* model and favors the $4e^-$ ORR pathway due to the weakened O=O bonding.[137, 148] This knowledge provides the pivotal impetus for designing dual-metal or multi-metal-site catalysts, which are more active towards ORR.[118, 149-152] Targeted synthesis is a promising way to further circumventing the current limitation in activity improvement. Among the immense carbon materials, MOFs with inherent versatility for composition and structural manipulation are the ideal platform for achieving the dual- or multi-atom chelation with precise control of atom species and active site density.

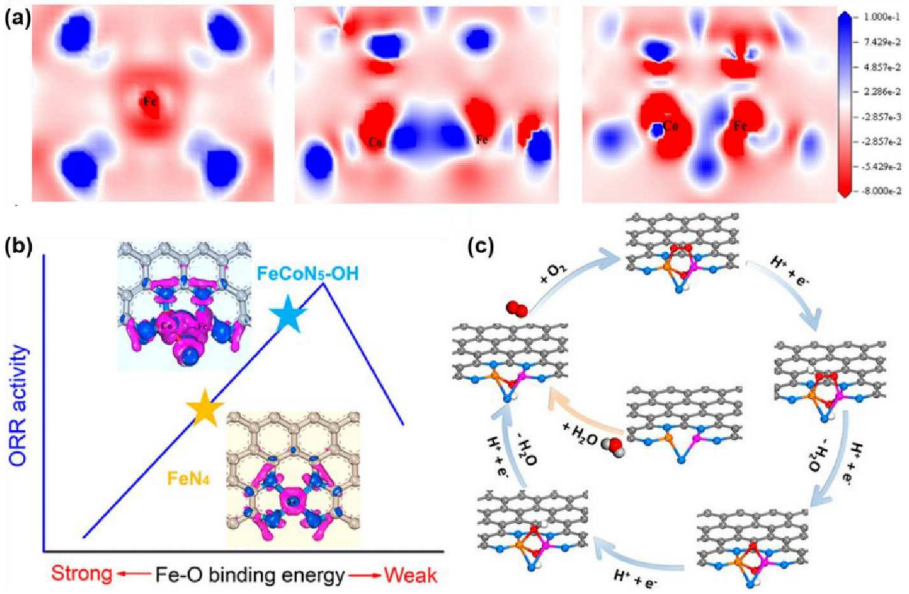

Fig. 4. (a) Calculated charge density differences for FeN_4 (left), $FeCoN_5$ (middle), and $FeCoN_5$-OH (right); (b) ORR activity of FeN_4 and $FeCoN_5$-OH sites as a function of Fe-O bonding energy; (c) The proposed ORR mechanism on the $FeCoN_5$-OH site. Reproduced with permission.[146] Copyright 2019, the American Chemical Society.

A typical synthesis of Fe-Co dual-site was coined by Wang *et al.,* who reported a double-solvent method to create Fe-Co dual sites embedded in N-doped porous carbons for the ORR under acidic conditions.[152] The key in the synthesis relied on the controlled bonding between Co and adsorbed Fe ions within the confined space of ZIF-8 frameworks. According to DFT calculations, the energy barrier of OOH dissociation into O and OH on Fe-Co dual-site was much lower than those on the single Fe or Co sites. Therefore, the Fe, Co-N-C catalyst delivered a superior catalytic activity than those of single-site catalysts with a higher selectivity toward the four-electron ORR pathway in acidic electrolyte. A novel OH-ligand self-binding strategy created Fe-Co binuclear sites to unveil the promotional role further.[146] The as-constructed triangle $FeCoN_5$-OH site catalyst

enabled dramatically improved intrinsic ORR activity (E_{onset} = 1.02 V) in acidic electrolytes. Introducing $FeCoN_5$-OH site configuration decreased the localized electron density around Fe atoms, as shown in **Fig. 4a**, leading to a weakened Fe-O bonding (**Fig. 4b**). Moreover, the preferential bridge-*cis* adsorption model on the binuclear site is advantageous over the conventional end-on model on mononuclear sites. The elongated O=O bond accelerates the bond cleavage rate and results in a promoted reaction path, therefore favoring ORR activity (**Fig. 4c**). This finding not only introduced a novel strategy to regulate the electronic and geometric structures of the active sites but also provided an insightful understanding of dual-metal sites toward the ORR mechanism. Inspired by these successes, targeted synthesis of the dual-atom site catalysts for boosting ORR activity attracted an ever-increasing interest.[150, 152, 153] In addition to Co, the doped Mn site enables the regulation of the electronic structure of FeN_x active sites.[154] For instance, pyrolysis of ZIF-8 encapsulated with Fe and Mn ions produced a bimetallic Fe, Mn-N-C catalyst with atomically dispersed dual-metal sites anchored on N-doped porous carbon. Comparing to monometallic FeN_x catalysts, the possible synergy effect between Fe and Mn atoms in the catalyst is the main reason for more efficient ORR in alkaline.[94] Recent advances in theoretical tools such as DFT calculations and machine learning would provide the origin of ORR activity enhancement on a variety of bimetallic sites and predict the possible new bimetallic systems such as Fe-Cu and Ni-Cu.[151] In short, the ORR activity of bimetallic site catalysts is dependent on multiple factors, including electron affinity, electronegativity, the radius of embedded metal atoms, heteroatom dopants, and local carbon defects. Benefiting from advantages of the dual sites, the development of dual or multiple metal site-embedded M-N-C catalysts may provide alternative opportunities to address current issues of single-site M-N-C catalysts with insufficient activity and stability.

However, innovative synthesis methods should precisely control the distance of two metal sites and their distribution on carbon supports for maximizing their synergy effect.

2.1.4 Edge hosted M-N_x sites

Aside from the unique chemical activity of the metal centers, the FeN_4 active sites in the edge position and basal plane also play different roles in the ORR process, leading to distinct catalytic activities.[155, 156] Previous reports manifested that porphyrin-like FeN_4 sites are mainly embedded in or located at the single graphene planes, while FeN_{2+2} sites are in the micropores defined by two adjacent graphene edges.[2, 108] Several theoretical studies hold similar views that FeN_4 structures follow different reaction pathways towards the ORR catalysis, depending on the location anchored in bulk, or at the edges of graphene. In the previous subsection, the edge-hosted sites are more active by their electron-withdrawing properties that decrease in the electron density of the metal center.[73, 76, 83, 108, 136, 137, 157, 158] The edge-hosted FeN_4 moieties dominated Fe-N-C catalyst achieved by selective C-N bond cleavage adjacent to Fe center is capable of lowering the overall ORR barrier.

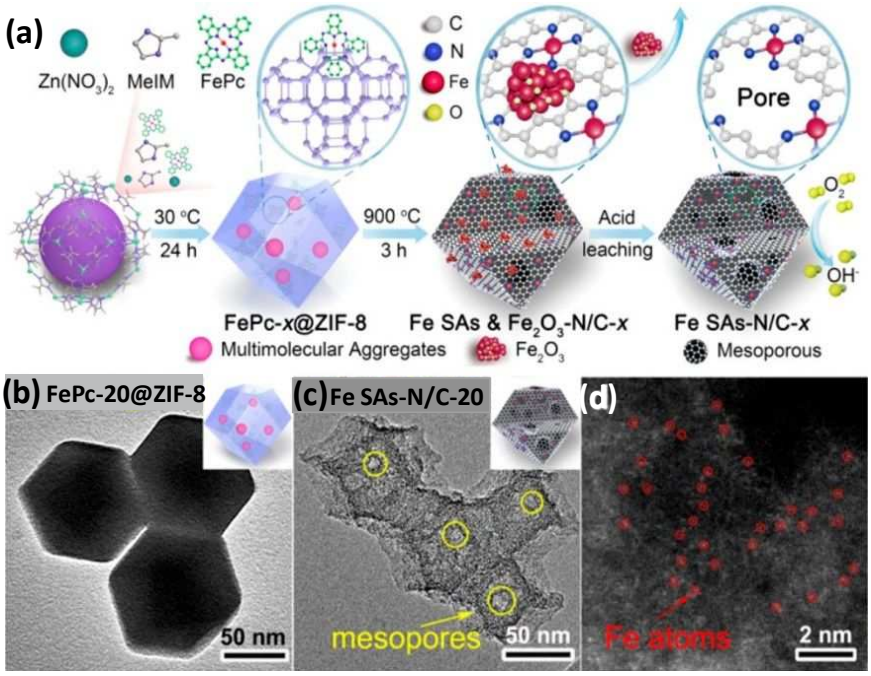

Fig. 5. (a) Design and synthetic process of edge-site hosted Fe-N-C catalysts. TEM images of the as-prepared (b) bulk-FePc-20@ZIF-8 precursors, (c) mesoporous Fe-N-C catalysts, (d) defective zigzag edge-hosted FeN_4 structures. Reproduced with permission.[159] Copyright 2018, the American Chemical Society.

Fig. 5a conferred an intriguing example for the edge site engineering. Trapping iron(II) phthalocyanine (FePc) molecules with a size of 14.6 Å into the ZIF cage (cavity size, 14.6 Å) produced a Fe-N-C catalyst, featured with hierarchical porosity and richness of edge-hosted FeN_4 moieties.[159] As evidenced in the TEM images in **Fig. 5b-d**, the FePc molecular acted as the cage buster for edge-site engineering and subsequent mesopore generator through the acid leaching of Fe_2O_3 nanoclusters. The edge-site riched Fe-N-C catalyst delivered superb ORR catalytic activity ($E_{1/2}$ reached to 0.909 *vs*. RHE in 0.1 M KOH electrolyte), attributing to the well-defined micro-mesoporous architecture and maximized exposure of active sites.[159] These results are consistent

with recent experimental and theoretical trends demonstrated by Zelenay *et al.,*[24] who demonstrated that FeN_4 moieties at the edges of graphitic domains might have higher ORR activity. The utilization of ammonium chloride (NH_4Cl) salt is another edge engineering strategy for creating abundant edge-hosted FeN_4 sites.[156] NH_4Cl not only prevents the aggregation of iron atoms and guarantees the preferential formation of edge-hosted FeN_4 sites, but also generates a large number of pores and N-doped edges in the graphene matrix. DFT calculations confirmed that the introduced in-plane holes would lower the absorption energy of intermediates such as O_2^* and OOH^*, thereby increasing the thermodynamic limiting potential. As expected, edge-hosted FeN_4 sites anchored catalysts demonstrated remarkable ORR activity in acids, representing one of the most active M-N-C catalysts so far. This work inspires the rational design of more advanced M-N-C catalysts for ORR through this pore-edge-engineering strategy.[79, 139, 159-161]

2.2 Populating single metal site density

Substantial studies suggest that aggrandizing the density of atomically dispersed MN_4 active sites in the catalyst is an essential design principle for maximizing catalytic activity.[85, 139, 162] However, the tendency of single metal atoms to form inactive metals, oxides, or carbides species during high-temperature pyrolysis renders a challenging work for attaining single metal sites in catalysts.[131,163-165] The shortage of anchoring sites such as defects or nitrogen/oxygen atoms in the carbon support is the major limitation, making it difficult for increasing the number of active sites. Moreover, the utilization of the single active sites is relatively low due to numerous active sites are buried in the catalysts that cannot contact the reactants. Therefore, extensive studies aim to develop effective strategies for realizing the synthesis of high-density MN_4 sites stabilized in carbon supports via preventing isolated atoms from migration /aggregation, strengthening the stabilizing effect of the support, or creating more anchoring sites.[85,91,119,162,163,166,167] Moreover, strategies such as creating

highly porous structures for exposing increased active sites to reactants is also pivotal in boosting the catalytic performances.

2.2.1 Chemical M-N bonding formation

Conventional synthesis of M-N-C catalysts includes the physical mixture of metal and nitrogen-containing ligand precursors, wet-chemical doping, and adsorption strategies. The physical mixture of metal and nitrogen precursors usually results in relatively weak M-N bonding during pyrolysis, giving rise to metallic aggregates instead of atomically dispersed MN_4 sites. Currently, chemical doping or ion adsorption strategies are effective in strengthening M-N interactions and populating MN_4 sites. These methods involved multi-steps of precipitation, impregnation, or adsorption of metal ions to the precursors or carbon supports with pre-existing nitrogen doping, followed by thermal activation. MOF precursors, in particular ZIF-8, composed of metal nodes and nitrogen-containing ligand, perfectly match the prerequisites for M-N bonding establishment. The subsequent thermal activation directly converts the M-N covalent bonds to MN_4 sites embedded into the partially graphitized carbon supports. However, pushing the limit of creating available MN_x moieties in MOF-derived carbons remains a roadblock, thus evoked tactful strategies for resolving it. There are two types of substantial strategies for establishing M-N bonds, nitrogen-containing ligand/defect trapping, and the chelation reaction between metal ions and molecular.

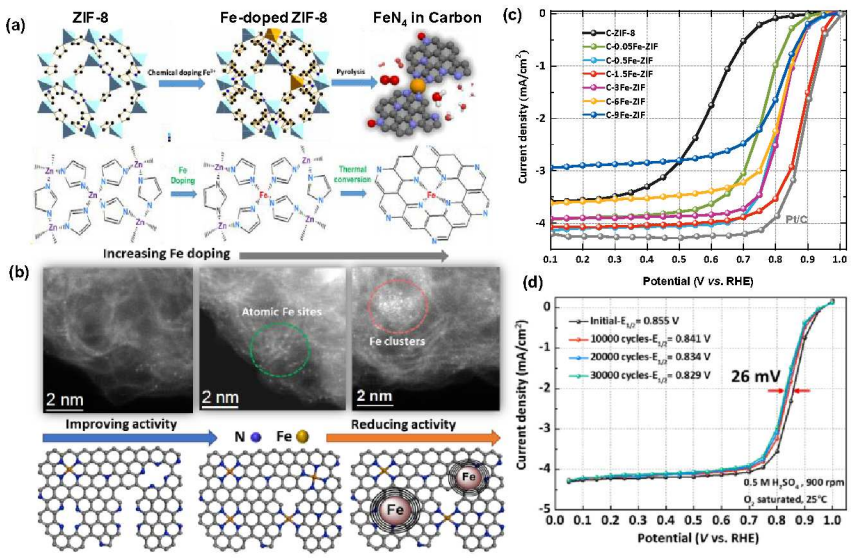

Fig. 6. (a) Synthesis process of chemical-doping of Fe precursors into ZIF-8 nanocrystals (upper) and the evolution of the Fe-doped carbon structures (lower). Reproduced with permission.[85] Copyright 2017, American Chemical Society. (b) HAADF-STEM images of single Fe sites (bright dots) ZIF-8-derived carbon catalysts with different Fe doping content. (c) ORR polarization plots in O_2-saturated 0.5 M H_2SO_4 for different *x*Fe–ZIF-8-1100 catalysts (x ranging from 0 to 15 at%). (d) ORR stability of the best performing 2.5Fe–ZIF-8-1100 catalyst evaluated by using accelerated stress test (AST) potential cycles (0.6-1.0 V). Reproduced from permission.[101] Copyright 2019, The Royal Society of Chemistry.

Many groups have embarked on the nitrogen-containing ligand/defect trapping methods for the synthesis of well-defined M-N-C catalysts with a high concentration of MN_4 active sites.[85, 91, 101, 119, 168] The pioneering works are chemical doping of Fe ions into ZIF-8 nanocrystals, which allows successfully realizing the accurate control of ZIF-8 nanocrystal size, Fe doping content,

and uniform distribution FeN_4 site. The best performing catalyst contains complete dispersion of atomic FeN_4 sites in the absence of any inactive metal species, conveying an excellent ORR activity (RDE, 0.5 M H_2SO_4: $E_{1/2}$ = 0.88 V, loading: 0.8 mg cm^{-2}; j = 2.0 mA cm^{-2} at 0.9 V).[85, 101] In the first step of the chemical doping, Fe ions partially replaced Zn and chemically bonded with imidazolate ligands in the form of FeN_4 complexes during the growth of ZIF-8 crystals in methanol solutions. Subsequent one-step thermal activation directly forms FeN_4 sites dispersed into partially graphitized carbon with particle morphologies (e.g., size, shape, and porosity) retained from ZIF-8 nanocrystals (**Fig. 6a**). The optimal doping content of Fe is crucial for maintaining the structural integrity of ZIF-8 frameworks and suppressing Fe migration due to the limited N-containing imidazolate ligand (**Fig. 6b**). The catalyst with optimal Fe doping content and particle size (e.g., 50 nm) possess maximum FeN_4 active sites, corresponding to the record-breaking ORR activity in an 0.5 M H_2SO_4 electrolyte with an $E_{1/2}$= 0.88 V, loading: 0.8 mg cm^{-2} and j = 2.0 mA cm^{-2} at 0.9 V. The doping content of Fe is crucial for affecting the size of ZIF-8 nanocrystals and their carbonization process during the pyrolysis. **Fig. 6c** shows that a small amount of Fe doping, such as 0.1 at.%, can increase ORR activity dramatically. Gradually increasing Fe content to 2.5 at % pushes the activity shift to the rightmost and then shift back when Fe content passes this threshold. Excess Fe content resulted in the formation of inactive or less active Fe species, which is a significant cause for the activity drop (**Fig. 6b**). The size of ZIF-8 nanocrystals could be adjusted in a wide range from 1 μm to 30 nm by decreasing corresponding metal ion concentrations during the growth of ZIF-8. The optimized carbon nanoparticle size is capable of exposing most of the accessible active sites and favoring the mass transfer. Moreover, the graphitization degree of the carbon matrix is also indispensable with the doped Fe content. Highly graphitized carbon could improve the stability but may at the expense of losing defects for anchoring metal sites. Thus, the

stability of the Fe-N-C catalysts is critical for balancing the density of active sites and the graphitization degree of the carbon support. Besides, due to the inherent strong covalent M-N bonding through this chemical-doping method, the as-prepared best-performing Fe-N-C catalysts demonstrated outstanding stability with only 26 mV $E_{1/2}$ loss after 30,000 AST potential cycle (0.6 to 1.0 V) tests (**Fig. 6d**). Therefore, the chemical-doping synthesis of highly efficient and stable Fe-N-C catalysts necessitates the optimal content of Fe ion precursors and carbon morphologies/structures.

Apart from directly using ZIF-8 precursors with a nitrogen-containing ligand for binding metal ions, defects in nitrogen-doped carbons are useful to trap metal ions for the formation of active MN_4 sites. We recently demonstrated that the ZIF-8 derived carbon (ZIF-NC) has defined nitrogen doping and carbon defects, capable of trapping sufficient Fe^{3+} ions to form the Fe-N complex at the room temperature.[91] Firstly, carbonizing ZIF-8 nanocrystals at 1100 ^{o}C resulted in pyridinic nitrogen-containing porous carbon-dopants. Then, Fe^{3+} ions were adsorbed onto or/and into the carbon host. Subsequent thermal activation at an optimal temperature at 700 ^{o}C can strengthen the bonds of Fe-N and form FeN_4 sites, showing exceptional ORR activity in acids.[91] In this synthesis, increased density of the active site is due to that all of Fe ions could participate in the FeN_4 sites embedding in the surface layers of carbon hosts, exhibiting reasonably high ORR activity with an $E_{1/2}$ of 0.85 V at a loading of 0.6 mg cm^{-2}.

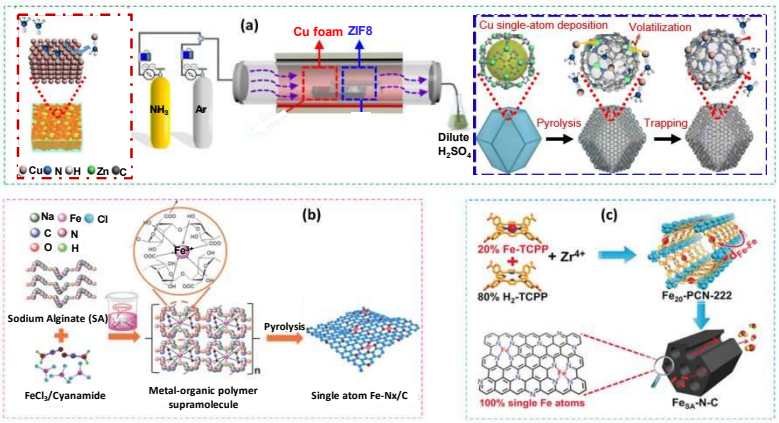

Fig. 7. (a) Schematic illustration of the synthetic procedure of the Cu-N-C catalyst through the chemical vapor deposition method. Reproduced with permission.[168] Copyright 2018, Nature Publishing Group. (b)The chelation reaction between metal-organic polymer supramolecular and Fe ions. Reproduced with permission.[163] Copyright 2018, Wiley-VCH. (c) Schematic demonstration of the synthesis of Fe-N-C using double ligand. Reproduced with permission.[169] Copyright 2018, Nature Publishing Group.

In addition to the effective chemical doping and adsorption methods, a variety of innovative approaches can prepare active single metal sites in M-N-C catalysts. For example, a simpler way was developed based on the defect-trapping strategy to prepare atomically dispersed metal (e.g., Fe, Co, Ni, and Cu) catalysts from corresponding bulk metals. Typically, the defects on the carbon support at the downstream can trap the $M(NH_3)_x$ species originating from ammonia gas complexation of metal atoms out of the upstream bulk metals. The basic principle is the strong Lewis acid-base interaction. Therefore, stabilizing isolated metal sites are generated in nitrogen-doped carbon supports (**Fig. 7a**).[168] The intrinsic activity of such-prepared single metal sites is not optimized yet. However, the chemical vapor deposition (CVD) strategies hold a great promise in

the mass production of high-quality single metal site catalysts. In addition to ZIF-8 derived carbon, defective graphene can provide sufficient defects (*e.g.*, vacancy and coordinating atoms) as trapping sites. A simple dangling bond trapping strategy is feasible to construct atomically dispersed Fe catalyst under ambient conditions through these defects.[167] Typically, defected graphene oxide (GO) slurry was uniformly injected into metal foam and drying in ambient conditions. The close contact between the metal bulk and GO would transfer electrons from M^0 to the dangling oxygen groups on GO and form $M^{\delta+}$ ($0 < \delta < 3$) species. Subsequently, M-O bonds formed through the coordination of $M^{\delta+}$ with the surface oxygen dangling bonds. Then the M-O bonds pull out the metal atoms from foam under the assistance of sonication. Thus, a high density of FeN_x active sites was generated in a Fe-N-C catalyst derived from polydopamine. The resultant catalyst endowed good ORR activity. Besides trapping Fe by nitrogen in carbon support to form FeN_4 active sites, Qiao's group[160] prepared a Co-C_3N_4 complex with a single coordinated Co atom through capturing Co ions by using pyridine-like nitrogen in graphitic carbon nitride (g-C_3N_4).

Another strategy for establishing an abundance of M-N bonding is through the chelation reaction between metal-organic polymer supramolecular and Fe ions.[163] As illuminated in **Fig. 7b**, the supramolecular structure of 3D metal-organic polymer can effectively disperse and stabilize Fe ions through the chelation reaction with its hydrophilic groups. Zhao *et al*. produced a series of M-N-C catalysts with high-loading MN_x moieties up to 12.1 wt.% by combining this chemical chelation approach with a coordination effect.[170] Studied metal ions included Fe, Co, and Mn, which were firstly sequestered by excess glucose and then anchored on the oxygen species-enriched porous carbon supports. This chemical chelation strategy is effective in the production of a wide range of atomically dispersed M-N-C catalysts. Utilizing Fe_x-PCN-222, a porphyrinic MOF constructed by Fe-TCPP (TCPP= tetrakis (4-carboxyphenyl) porphyrin) and H_2-TCPP dual ligands

(**Fig. 7c**) is another practical method for fabricating single-atom Fe-implanted N-doped porous carbon catalyst.[169] The intriguing point is that the spatial distance between Fe atoms in the MOF skeleton could be modulated by changing the ratio of the two ligands, efficiently hindered the aggregation of the Fe atoms during pyrolysis. The porous carbon can contain a high density of FeN_x sites due to the periodic and tailorable structures in the Fe_x-PCN-222. All results mentioned above ascertained the critical role of metal-ligand/chelating agent interaction in stabilizing the single metal atoms, thus giving birth to a series of Fe-N-C,[35, 133] Co-N-C,[104, 161, 171] Mn-N-C,[172, 173] and the newly emerging Cu-N-C catalysts.[174]

In summary, the existence of defects and heteroatom dopant (*e.g.*, N) can produce vacancies and unsaturated coordination sites in the carbon support.[137, 161, 175, 176] They are crucial and act as "traps" to catch and anchor transition metal atoms through an enhanced charge-transfer mechanism during the critical heating treatment processes.[168, 171] In principle, the density of unsaturated nitrogen in carbon support is the key to maximizing the density of MN_x sites in catalysts.[177] The chelation reaction of nitrogen-containing molecular with metal ions offers another effective way of establishing strong M-N bonding and attaining a high density of active sites. Therefore, the deliberate selection of suitable nitrogen contained precursor and innovative concepts to generate a high density of unsaturated nitrogen in carbon supports can significantly populate MN_x sites in M-N-C catalysts for improved mass activity.

2.2.2 Spatial confinement effect

The space confinement is effective to prepare atomically dispersed MN_x active sites in M-N-C catalysts. The basic principle of the spatial confinement effect lies in the employment of the built-in pores/cavities (*i.e.,* the cages in MOF materials) or foreign items (*i.e.,* the secondary atom, hard or soft template) for restricting the movement of the metal atoms, thus creating a high density of

isolated MN_x moieties. The existence of the abundant molecular cages in MOF materials endowed the ideal choice for encapsulating metal precursors. In a typical example, $Fe(acac)_3$ molecules were trapped in the cage of ZIF-8 nanocrystals during the assembly of Zn^{2+} and 2-methylimidazole.[160] After pyrolysis, $Fe(acac)_3$ within the cage was reduced by carbonization of the organic ligand, leading to the formation of isolated single Fe sites anchored on nitrogen-doped carbon. Cao *et al.,* [178] attained a high Fe loading up to 3.8 wt.% in a catalyst through encapsulating massive tetraphenyl porphyrin iron (Fe-TPP) molecules into the vast interior cages of rho-ZIF (a kind of ZIF with the rho topology) *via* a mechanochemical method. Such a high loading of active sites affirmed that the host-guest confinement strategy could effectively segregate single Fe centers and increase the density. In addition to the cages, the secondary atoms like Zn, Na, K, or Mg act as the fences for avoiding the target metal atoms from intimate contacts.[179, 180] A distinct instance is the Zn atoms in ZIF materials, acting as the inartificial isolation agent for the creating ZIF-8 derived single metal site M-N-C catalysts.[85, 101, 119, 168] Another benefit of using these kinds of secondary atoms is that they induce dominant micropores after removing them either by washing or the high-temperature pyrolysis (Zn evaporate over 900 ℃).[112] Taking the Co-doped ZIF-8-derived Co-N-C catalyst as an example, the key lies in the ratio adjustment of Co and Zn atoms to reach a limit of obtaining a high density of uniformly dispersed single Co sites. The appropriate feeding dose of Zn precursors prevents single Co sites from the aggregation.[104, 179]

Usually, compared to other metals, Mn atoms tend to form ORR-inactive oxide species more easily during high-temperature pyrolysis, representing a grand challenge to prepare single Mn site catalysts. An effective two-step doping and adsorption approach by combining the chemical doping and spatial confinement strategies can generate a high density of MnN_4 sites.[168] With that, we successfully developed an Mn-N-C catalyst with dominant atomically dispersed MnN_4 sites on

a carbon support. First, the carbonization of Mn-doped ZIF-8 precursors followed by subsequent acid leaching yields a partially graphitized microporous carbon with optimal nitrogen doping and a small fraction of MnN_4 sites. Second, microporous carbon can host additional Mn and N sources and generate incremental density of MnN_4 active sites, followed by additional heat treatment. The XAS analysis and aberration-corrected STEM imaging coupled with atomic-level EELS demonstrated the atomically dispersed MnN_4 sites are in the partially graphitic carbon matrix. With the optimizations of chemical doping of Mn content and subsequent adsorption procedures, the best performing atomically dispersed Mn-N-C catalyst generated encouraging activity with an $E_{1/2}$ of ~ 0.80 V *vs*. RHE along with enhanced stability in 0.5 M H_2SO_4 relative to a Fe-N-C catalyst prepared by identical procedures.

High-temperature treatment steps are inevitable for the synthesis of M-N-C catalysts. Still, they produce inactive metallic aggregates, thereby inhibiting the formation of high-density MN_x active sites.[89, 94, 181] To address this issue, an innovative "silica-protective-layer-assisted" approach can maximize the number of FeN_4 sites in a Fe-N-C catalyst.[158] Typically, a silica coating induced effective confinement for limiting the free migration of iron species during high-temperature pyrolysis, generating a higher density of FeN_4 sites than that of a catalyst prepared without the silica coating. Following this mechanism, the silica-confined strategy has been used frequently by other groups.[163, 175, 182] Similarly, mSiO_2-protected pyrolysis strategy proven to be useful for inhibiting the aggregation of Co species and generated a hierarchically porous Co, N co-doped carbon nano framework (Co, N-CNF).[183] Apart from the hard-template coating strategy, soft-template surfactants can also confine and protect the MN_x active sites from aggregation during the pyrolysis.[47, 91, 175, 184] Inspired by the effective interactions between surfactants and ZIF-8 nanocrystals,[185] our group synthesized atomically dispersed Co-N-C catalysts with immensely

increased CoN_4 sites from surfactant (*i.e.*, F127)-assisted ZIF-8 (**Fig. 8a**).[105] This unique confinement effect suppressed the migration of atomic Co and mitigated the collapse of micropores within ZIF-8 during the pyrolysis. Consequently, the atomically dispersed Co-N-C@F127 catalyst with a core-shell structure possessed considerably increased active site density, showing three-time higher single Co site content relative to surfactant-free Co-N-C catalysts (**Fig. 8b**). The catalyst delivered exceptionally enhanced ORR activity ($E_{1/2}$= 0.85 V), four-electron selectivity (H_2O_2 yields < 2%), and improved stability in acidic electrolytes, representing the best Co-N-C catalyst (**Fig. 8c**).

In summary, introducing secondary spacing atoms, hard-, or soft-templating coatings revealed the merits of spatial confining or the isolation effect for preventing the metal atoms from wandering around to form inactive metal species. This strategy effectively populates the number of active sites in M-N-C catalysts, thus favors a more promising ORR activity. However, merely increasing the density of active sites does not ensure a higher catalytic performance. The intrinsic activity (discussed in section 2.1) and the accessibility of each active site undertake the same paramount role in optimizing the mass activity and catalyst utilization of M-N-C catalysts.

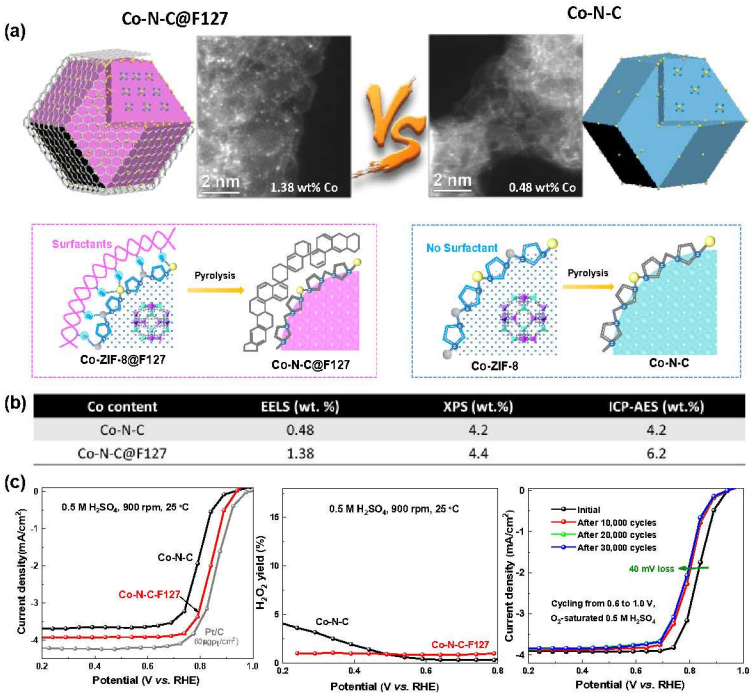

(b)

Co content	EELS (wt. %)	XPS (wt.%)	ICP-AES (wt.%)
Co-N-C	0.48	4.2	4.2
Co-N-C@F127	1.38	4.4	6.2

Fig. 8. (a) Proposed *in situ* confinement pyrolysis strategy to synthesize core–shell-structured Co-N-C@surfactants catalysts. (b) Elemental analysis of Co single sites to demonstrate the significantly increased Co single sites by using the F127 surfactant. (c) ORR activity and stability of the Co-N-C catalysts through a surfactant confining approach. Reproduced with permission.[105] Copyright 2018, the Royal Society of Chemistry.

2.2.3 Porous structure design

In-plane Fe atoms coordinated with pyridinic nitrogen at the edge of a graphene-type matrix are the likely active site in Fe-N-C catalysts.[86, 158] However, the micropores, where the edges and steps of the carbon layer, host numerous FeN_4 active sites.[24, 70, 85] Unfortunately, protons and O_2 gas molecules are restricted mainly from accessing active sites in micropores with small pore sizes (less than 2 nm), resulting in the insufficient formation of three-phase boundaries.[186] Therefore, it

is critical to rationally design optimal porous structures for promoting the mass transfer and exposing more accessible active sites.[187] Feng and coworkers employed three different templates, including silica nanoparticles and montmorillonite to create mesopores in catalysts.[63] A mesoporous Co-N-C catalyst derived from a VB12 precursor and silica nanoparticles template exhibited prime ORR activity in acidic medium relative to others. The superior activity is due to their optimized porous structures with a narrow mesopore size distribution, high BET surface areas, and homogeneous distribution of abundant CoN_4 active sites.

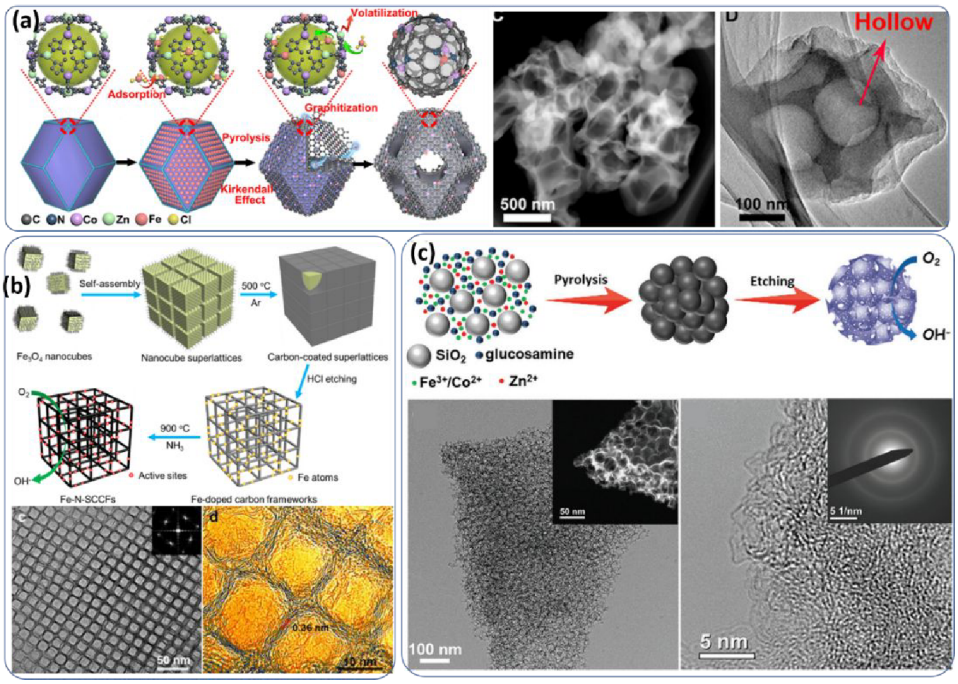

Fig. 9. (a)Hollow structured ZIF-8 derived FeCo-N-C. Reproduced from permission.[152] Copyright 2017, American Chemical Society. (b) Fe-doped carbon frameworks. Reproduced from permission.[188] Copyright 2017, American Chemical Society. (c) Hierarchically porous Fe-N-C and Co-N-C. Reproduced from permission.[112] Copyright 2018, Wiley-VCH.

Also, porous M-N-C catalysts with various morphologies have demonstrated a great promise to maximize the utilization of active sites.[62, 112, 188-191] Despite the structural diversity of the synthesized catalyst, most of them share the same idea of "hierarchical porous structures" (**Fig. 9**), which possess multimodal pore size distribution with interconnected micro-, meso-, and macropores, simultaneously increasing active site density and facilitating the access of the O_2 and electrolytes to these active sites. Because of the lack of fundamental understanding, it is intuitive to explain the effect of multimodal pore size distribution on ORR activity. Designing and realizing the cooperative roles of well-designed hierarchical pores to improve mass transports are still challenging. The relationship between porous structures and MEA performance is crucial for gaining relevant understands and generating criterion to assess the effectiveness of the porous structure. Recently, Hyeon *et al.* studied three N-doped carbon model catalysts with different pore size distributions but similar BET surface areas and active site concentration.[187] Macropores and mesopores contributed to different stages of the reaction kinetics. Specifically, macropores promoted kinetics of available active sites in the time scale of the ORR. Mesoporous structure facilitated electrolyte wetting of the solid surface area, thus leading to augment of the portion of electrochemically available active sites. Motivated by this criterion, the authors further synthesized Fe-N-C catalysts by loading FeN_x active sites to these model carbon supports. The Fe-N-C catalyst with the trimodal pore size distribution of optimal macro-, meso-, and micropores exhibited the best ORR activity. Other similar works also reported the synthesis of atomically dispersed metal catalysts with optimized porous structures and exhibited improved ORR activities.[62, 175, 192]

Overall, optimal hierarchically porous structures can maximize the catalytic performances of the M-N-C catalysts by facilitating the mass transfer, amplifying the density of active sites, exposing each active site accessible to the reactants, and regulating the water management.

Relative to ORR activity measured by using RDE tests, the specific roles of micro-, meso-, and macro-pores of M-N-C catalysts in MEAs are imperative because of the more complicated electrode configurations.

3. Strategies to improve PGM-free cathode performance in MEAs

Similar to PGM catalysts, it is challenging to transfer the activity and stability of M-N-C catalysts to the high-performance electrode in MEAs. Because there is no sufficient understanding and knowledge to guide electrode design to achieve optimal three-phase interfaces for mass and charge transports during the ORR. Increasing experimental efforts indicated that the trends of ORR activity in aqueous electrolytes and MEA performance of electrodes are often not in a good agreement, as inferred from **Table 1**. The complicated porous and thick 3D electrodes containing solid-state ionomers limit the transports of O_2 and protons. Limited accessibility of active sites in micropores within electrodes significantly compromises the catalyst utilization. Therefore, electrode structures play essential roles in generating sufficient current densities in both kinetics and mass transport voltages. Depending on specific surface areas and porosity of specified catalysts, electrode fabrication procedures, and the optimal ionomer content and solvents may be different, requiring several optimizations. Degradation mechanisms of M-N-C catalysts in MEAs might not be identical to those in acidic solutions due to the more complicated conditions in MEAs. Apart from the loss of intrinsic activity, the collapse of interfaces due to the morphology changes of ionomers and carbon corrosion also cause significant performance loss in MEAs. Water flooding is severe in thick M-N-C electrodes, which is responsible for partial performance loss in MEAs. Hydrophobicity of electrodes is related to multiple catalyst properties, including surface functionalities, degree of graphitization, and porosity. Ionomer content and additives such as

polytetrafluoroethylene (PTFE) affect the hydrophobicity in electrodes as well. Therefore, generating knowledge from extensive MEA studies along with characterization and modeling simulations at multiple scales is crucial for high-performance MEAs. U.S. DOE proposed a set of performance metrics at the MEA level (**Fig. 10),** including activity and durability.[14, 168] In 2007, DOE initially selected a volumetric current density of 300 A cm^{-3} at 0.8 $V_{iR\text{-}free}$ as the catalytic activity target. In 2016, DOE changed the goal to more challenging targets in MEAs, *i.e.*, 0.044 A cm^{-2} at 0.9 $V_{iR\text{-}free}$ under 1.0 bar O_2 at 80°C. Also, under more practical air, the current densities directly measured at 0.8 V should achieve 150 and 300 $mAcm^{-2}$ under 1.0 bar by 2020 and 2025, respectively. The MEA performance in terms of power density at rated voltage (*i.e.*, 0.67 V) has a tentative goal > 450 $mWcm^{-2}$ and a long term goal to match PGM catalysts (>1.0 Wcm^{-2}). Compared to PGM electrodes, studies on PGM-free electrodes are much less intense and still lack a comprehensive summary. In this section, we, therefore, focus on the understanding of how MEA performance links to a variety of critical factors from primary catalyst morphologies to electrode structures. Measuring power density under H_2-O_2 conditions is not meaningful. Instead, MEA performance under practical H_2-air at 1.0 bar is more relevant to transportation applications. Most of MEA tests for M-N-C catalysts in the early stage did not follow the U.S. DOE protocols. We still discuss those results to highlight the innovative concepts and approaches to constructing electrodes for MEA performance improvement.

Table 1. Representative M-N-C catalysts and their catalyst activity and MEA performance.

Name	Onset potential	Half-wave potential	Electrolyte	Fuel cell performance	Ref.
Py-B_{12}-M/C	/	0.8 V	0.1 M $HClO_4$	H_2-O_2: 0.26 W cm^{-2};	193
Co-PPy-C	/	0.65 V	0.5 M H_2SO_4	H_2/2.0 bar O_2: 0.28 W cm^{-2}	194
Co-CNM	/	0.75 V	0.5 M H_2SO_4	0.023 W cm^{-2}	195
Co−N/CNFs	0.82 V	0.7 V	0.1 M $HClO_4$	0.016 W cm^{-2}	39
Co/Zn$(mIm)_2$-P	0.93 V	0.76 V	0.1 M $HClO_4$	0.374 W cm^{-2}	196

20Co-NC-1100	0.93 V	0.8 V	0.5 M H_2SO_4	H_2/O_2: 0.56 W cm^{-2}; H_2/air: 0.28 W cm^{-2}	197
Co-N-C@F127	0.93 V	0.84 V	0.5 M H_2SO_4	H_2/O_2: 0.87 W cm^{-2}; H_2/air: 0.28 W cm^{-2}	105
FeNC-1000	0.894 V	0.804 V	0.5 M H_2SO_4	H_2/O_2: 1.01 W cm^{-2}	198
(Fe,Co)/N-C	1.06 V	0.863 V	0.1 M $HClO_4$	H_2/O_2 (0.2 MPa): 0.98 W cm^{-2}; H_2/air: 0.505 W cm^{-2}	152
(CM+PANI)-Fe-C	/	0.80 V	0.5 M H_2SO_4	H_2/O_2: 0.87 W cm^{-2}; H_2/air: 0.42 W cm^{-2}	24
PANI-Fe-MCS	/	0.80 V	0.5 M H_2SO_4	H_2/O_2: 0.83 W cm^{-2};	199
Fe-NC-Phen-PANI	/	0.80 V	0.5 M H_2SO_4	H_2/O_2: 0.86 W cm^{-2}; H_2/air: 0.38 W cm^{-2}	60
TPI@Z8(SiO_2)-650-C	/	/	/	H_2/2.5 bar O_2: 1.18 W cm^{-2}; H_2/air: 0.42 W cm^{-2}	200

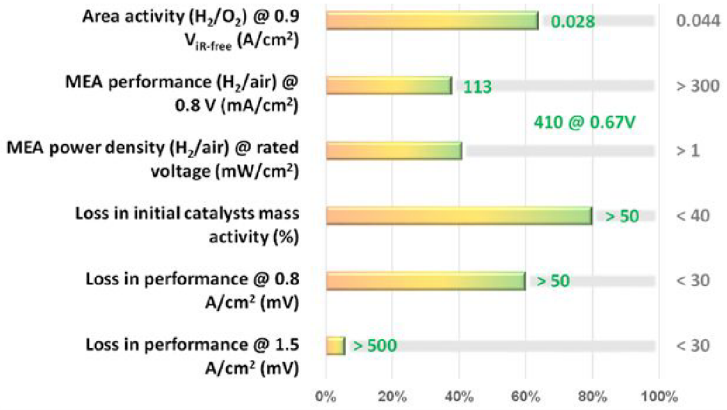

Fig. 10. DOE 2025 technical targets and current status of PGM-free cathode catalysts for transportation applications.

3.1. Effects of primary catalyst morphologies on MEA performance

As for desirable morphologies of M-N-C catalysts, micropores are critical for populating and hosting high-density MN_4 sites. The O_2 and H_2O should transport to and from these active sites through meso- and macropores with minimal resistance. Micropores should connect through continuous mesopores accessible to ionomers for proton conduction. The carbon supports connecting these pores at multiple scales should provide facile electron conductivity and sufficient

resistance to corrosion under practical MEA operation conditions. In this section, we summarize effective synthesis methods to engineer micro-, meso-, and macropores in M-N-C catalysts for boosting MEA performance.

3.1.1 The importance of micro-, meso-, and macro-pores from catalysts to electrodes

Populating micropores to increase site density in electrodes

Populating micropores could be sufficient to accommodate single metal active sites within limited volume and mass of electrodes in MEAs.[201] Substantial efforts have led to significantly increased micropore in M-N-C catalysts by using high-surface-area carbon black supports[2,24,102] or exploring appropriate nitrogen precursors to engineer carbon porosity.[21,50] Dodelet and his coworkers achieved one of the crucial milestones in the early studies of Fe-N-C catalysts.[2] They prepared a Fe-N-C catalyst with high-density active sites through introducing a pore filler phenanthroline and iron precursors (*i.e.*, FeAc) into the micropores of commercial carbon black (*i.e.*, Black Pearl 2000, BET surface areas >1500 m^2g^{-1}) (**Fig. 11a** and **11b**). The innovative synthesis method included the use of ball-milling precursors and subsequent two-step heating treatments (Ar at 1050 ^oC and then NH_3 at 950^oC). During pyrolysis at temperatures of ≥800°C, NH_3 partly gasifies the carbon support and create substantial micropore in carbon-black particles. The resulting catalyst delivered a record MEA performance by 2009, in which the extrapolated volumetric current density reached 99 A cm^{-3} at 0.8 $V_{iR\text{-}free}$.[2] Although the MEA durability of the catalyst is still a serious issue, this success verified the unprecedented role of micropores in boosting MEA performance.

Motivated by these encouraging performance improvements, MOF materials, which often contain dominant micropore and large surface areas, have been selected as a host for Fe and N precursors for designing M-N-C catalysts.[22, 40, 202] The first MOF was chosen is the commercial Zn(II)-based ZIF-8 ($ZnN_4C_8H_{12}$, Basolite Z1200 from BASF). It has an extremely high surface

area up to 1,800 m^2 g^{-1} and an overwhelming microporous structure (**Fig. 11c** and **d**).[102] In 2011, replacing the commercial carbon black support with a ZIF-8 yield a new Fe-N-C catalyst, which exhibited an unusual volumetric activity of 230 A cm^{-3} at 0.8 $V_{iR\text{-}free}$ cell voltage determined from the intersection of the extrapolated Tafel slope (**Fig. 11e-g**). This value is much higher than 99 A cm^{-3} of the commercial carbon black (*i.e.*, BlackPearl 2000) -derived one (red plot in **Fig. 11g**). The dramatic improvement is due to the unique micropore morphology of ZIF-8 precursors. Also, the richness of nitrogen in ZIF-8 potentially facilitates the formation of FeN_4 active sites hosted by the partially graphitized carbon directly converted from the hydrocarbon network within ZIF-8s. Therefore, catalysts and carbon supports are the same, significantly increasing the density of active sites. Besides substantial micropores, the use of ZIF-8 also yields significant mesopores around 50 nm in diameter (**Fig. 11c-d**). The improved porous structure was attributed to zinc evaporation from ZIF-8 precursors during the high-temperature pyrolysis due to the relatively low boiling point of zinc at 907 ^oC, thus generating an interconnected hollow structure. Therefore, the dense FeN_4 moieties plus the highly porous structure endowed the Fe-N-C catalyst with a notable improvement in H_2-O_2 MEA performance with a maximum power density of 0.75 W cm^{-2} at 0.6 V, a practical operating voltage of PEMFCs (**Fig. 11e-g**).

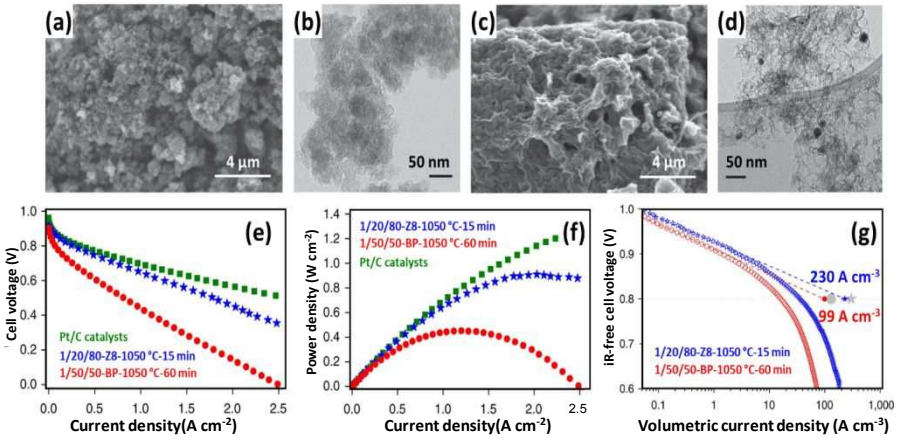

Fig. 11. Morphology and structure comparison of (a-b) previous Fe-based catalyst using commercial carbon black support, 1/50/50-BP-1050 °C-60 min. (c-d) The current most active Fe-based catalyst using heat-treated ZIF-8support, 1/20/80-Z8-1050 °C-15 min. (e) Polarization plots, (f) power density curves, and (g) Tafel plots for determination of the volumetric activity of cathode. Reproduced with permission.[102] Copyright 2011, National Academy of Sciences.

Inspired by the pioneering work, similar Fe-N-C catalysts derived from ZIF-8 precursors exhibited enhanced ORR activity and MEA performance by using a variety of many innovative synthesis methods.[4, 104, 175, 203] Compared to previous work by using ZIF-8 as supports for additional Fe and N precursors, the new method using the active metal-doped ZIF-8 consisting of M, N, and C precursors has many advantages. First, the uniform ZIF-8 crystals can yield homogenous catalyst morphology to control the density of active sites **(Fig. 12a)**. Second, the approach eliminates the tedious post-treatments, including acidic leaching and the second heating treatment, which improve the feasibility of large-scale and low-cost manufacturing. Third, the hydrocarbon networks in ZIF-8s directly convert into the necessary carbon phases. Thus, no additional carbon black supports are required, improving the volumetric activity of catalysts and reducing the cost. Therefore, the doped ZIF-8-derived Fe-N-C catalyst exclusively contains

atomically dispersed FeN_4 sites (**Fig. 12b**) and shows very encouraging activity and stability in aqueous acidic media. Fuel cell tests carried out at Los Alamos National Laboratory (LANL) further verified the high performance of the new Fe-N-C catalysts, generating 0.044 A cm^{-2} at 0.87 $V_{iR\text{-}free}$, approaching DOE's target of 0.044 A cm^{-2} at 0.90 V (**Fig. 12c**). Under H_2-air at 1.0 bar conditions, the current density of 75 mA cm^{-2} is very encouraging at 0.8 V (**Fig. 12d**). More importantly, the catalyst stability determined by both RDE's potential cycling and fuel cell testing at a practical voltage of 0.7 V holds great promise to overcome the stability challenge of PGM-free cathodes. Therefore, due to the dramatically increased active site density hosted in micropores of ZIF-8-derived carbon, the ZIF-8 has represented the most effective precursor to prepare high-performance Fe-N-C catalysts.

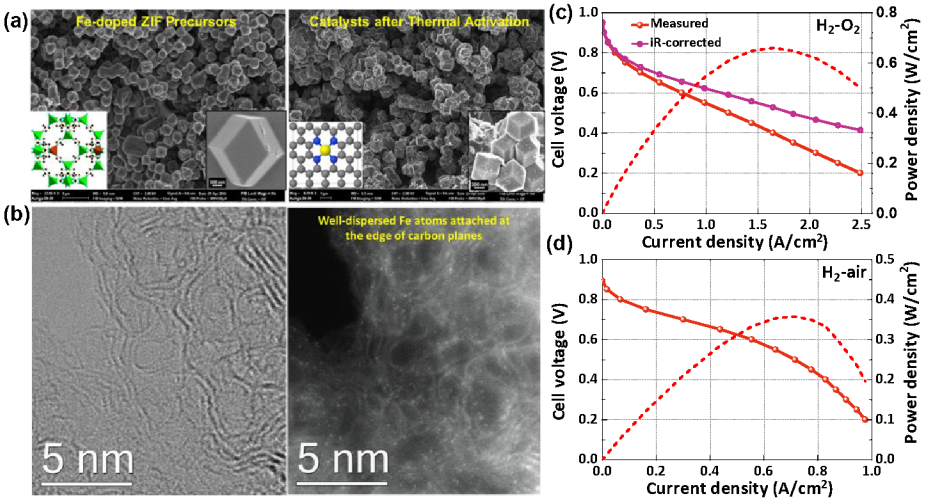

Fig. 12. Morphology and fuel cell performance of a Fe-N-C catalyst developed from chemical doping of Fe ions into ZIF-8 precursors. SEM images and HAADF-STEM images of the as-prepared chemical doped ZIF-8 derived Fe-N-C catalyst with (a) homogeneous morphology and (b) the formation of FeN_x species embedded into carbon matrix. Reproduced with permission.[85] Copyright 2017, American Chemical Society. Fuel cell performance in (c) H_2-O_2 and (d) H_2-air at 1.0 bar. Reproduced with permission.[101] Copyright 2019, The Royal Society of Chemistry.

Enriching meso/macropore structure to facilitate mass transports

Despite the encouraging performance improvement, the M-N-C catalysts-based PGM-free MEAs still suffer from insufficient performance and mass-transport issues, and therefore not yet attaining comparable performance to PGM-based catalysts. The current low performance of PGM-free cathodes in MEAs is due to low catalyst utilization (low mass activity), poor H^+ or O_2 transports, and severe water flooding. Therefore, establishing efficient ionomer/catalyst interfaces is crucial for robust triple-phase boundaries (TPB, the interface where the gas reactant O_2 meets electrons from the solid phase and protons from the electrolyte phase) for the ORR within the cathode.[93, 186] The poor dispersion of the ionomer into the catalyst particles often leads to less effective TPB, which is likely due to the dominant micropores and unfavorable pore structures of the catalyst. Therefore, improving catalyst utilization is critical for performance enhancement by creating sufficient mesoporous (2-50 nm) morphologies and controlling the ionomer/catalyst interface within the cathode layer. Large-sized macropores (pore size >50 nm) are also of vital importance to favor the mass transfer of reactant (protons and O_2) and product (H_2O) throughout the thick cathode electrode layer.[204] The introduction of macropore can reduce tortuosity and subsequently increase the volume current density of cathodes. However, macropores are very limited in traditional M-N-C catalysts, usually dominant with amorphous carbon. They are only the voids among the agglomeration of carbon particles due to the stacking of carbon particles around 50-100 nm.

3.1.2 Strategies for the porosity engineering

Template and coating strategy for surface porosity controls

Significant advancements in MEA performance of M-N-C cathodes indicated that, in addition to intrinsic activity, an optimal distribution between micro-, meso-, and macropores in a favorable carbon morphology is crucial for achieving efficient mass and charge transports.[46, 205-207] Surface porosity engineering of M-N-C catalysts is the fundamental step for catalyst structure optimization applied in MEA electrodes. Templated-directed strategies are the most popular and facile methods for creating pores with well-controlled size and architecture. The templates could either be hard ones such as metal oxides/sulfides and metal salts or soft ones such as polymers and surfactants.

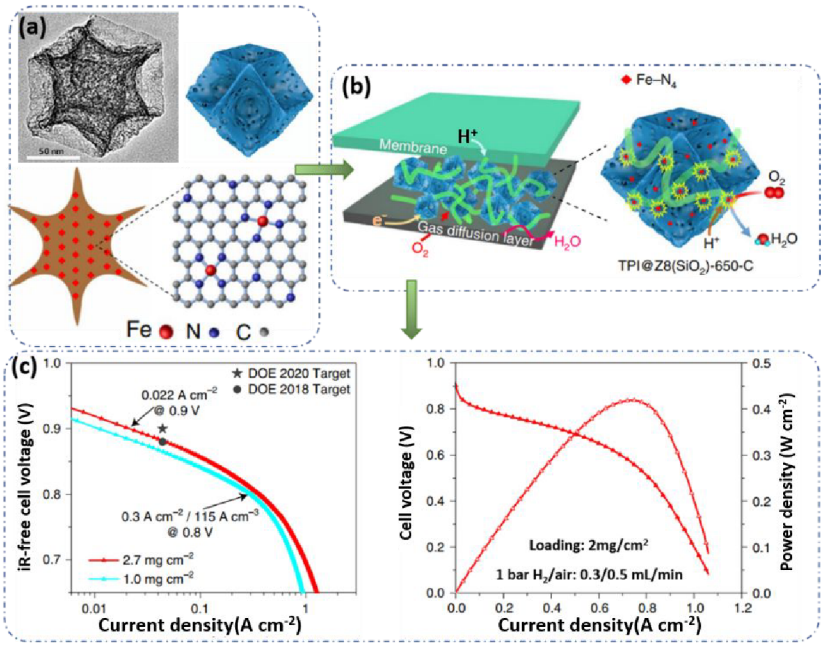

Fig. 13. (a) The morphology and surface structure of the concave-like Fe-N-C catalyst with dominant mesopores. (b) Schematic illustration of the TPB in a concave-like Fe-N-C catalyst-based cathode electrode. (c) (left) Tafel plot for determination of the current density at $0.9V_{iR\text{-}free}$ in 1 bar H_2-O_2 cell; (right) Polarization and power density plot of the catalysts in H_2-air cell. Reproduced from permission.[139] Copyright 2019, Nature Publication Group.

Atanassov's group has widely developed a well-known sacrificed silica-template method (SSM) at the University of New Mexico.[208-211] The SSM can yield an open-frame carbon structure by incorporating fumed silica precursors, in which the complete removal of the silica phase after pyrolysis is crucial for creating an internal pore network. The nature of the internal porosity generally depends on the size of the silica precursor used. Silica templates also modify the morphology of the catalysts for enlarging the exposed active site density. Recently, ZIF-8-derived carbon particles coated with a layer of silica lead to a Fe-N-C catalyst with a concave structure containing dense Fe-N_4 moieties. After leaching out the SiO_2 by using NaOH, the ZIF-8 derived carbon can adsorb additional Fe and N precursors followed by a multiple-step high-temperature treatment at 1000 and 800 ^oC using Ar and NH_3, respectively. As a result, the concave-like Fe-N-C catalyst increases external surface areas and mesoporosity and benefits for ionomer dispersion, therefore significantly improving FeN_4 site utilization in catalyst layers (**Fig. 13a** and **13b**).[139] The corresponding MEA showed a high current density of 0.022 A cm^{-2} at 0.9 $V_{iR\text{-}free}$ or 0.047 A cm^{-2} at 0.88 $V_{iR\text{-}free}$ under 1.0 bar H_2-O_2 conditions (upper plot in **Fig. 13c**).[139] Additionally, the MEA generated a high power density of 1.18 W cm^{-2} under 2.5 bar H_2-O_2 and an unusual activity of 129 mA cm^{-2} at 0.8 $V_{iR\text{-}free}$ under 1.0 bar H_2-air (lower plot in **Fig. 13c**). The quantitative analysis in this work further elucidated that catalyst mesoporous/external surface areas play an essential role in maximizing accessible FeN_4 sites and enhancing mass transfer, which dominates the current delivery efficiency in MEAs. This work indicated that the concave structure is effective in increasing mesopores to boost accessible active sites for overall MEA performance.

However, the complexity of template formation and removal limit the scale-up of catalyst synthesis. The complete removal silica requires hazardous HF and particular attention and expertise to handle it. Therefore, a template with simple, green manufacturing, and easy removal

process is of considerable significance and, as such, is highly desired. Recently, a MgO-templating strategy can benefit the formation of dense atomically dispersed FeN_4 moieties by separating adjacent Fe ions and avoiding the creation of inactive aggregates during pyrolysis.[212] The nano-MgO template can be removed by a mild acid solution at room temperature, leaving well-defined hierarchical porous structures. As expected, the catalyst achieved a high current density and encouraged durability in H_2-O_2 MEA tests.[199] Also, NaCl crystallizes can act as a water-removable template to synthesize 3D graphene-like macroporous Fe-N-C catalysts. NaCl crystallites introducing in precursors can serve as a blocking agent to prevent both significant weight loss and nitrogen evaporation during the pyrolysis. As a result, a Fe-N-C catalyst contains a macroporous carbon and a high Fe/N doping content synthesized by using N-rich polyvinylpyrrolidone (PVP) with an optimal addition of NaCl. The as-obtained Fe/N-doped 3D MPC failed to show exceptional high MEA performance (450 mW cm^{-2} under H_2-O_2 at 1.0 bar), likely due to the insufficient active site. However, the creation of macropores by using water-removable NaCl is a new strategy that deserved in-depth explorations.

Self-template strategies for hierarchical porosity engineering

As has been highlighted in section *3.1.1*, a hierarchical porosity of M-N-C catalysts with an optimal balance between micro, meso, and macropores is more desirable in MEA electrodes for achieving high performance by taking full advantage of each type of pore structures. The template-directed strategy is powerful in integrating different sized pores into the catalysts by employing multiple types of templates. The self-templates range from the pore-forming nitrogen-containing precursors to the *in situ* formed metal species or the carbon precursors.

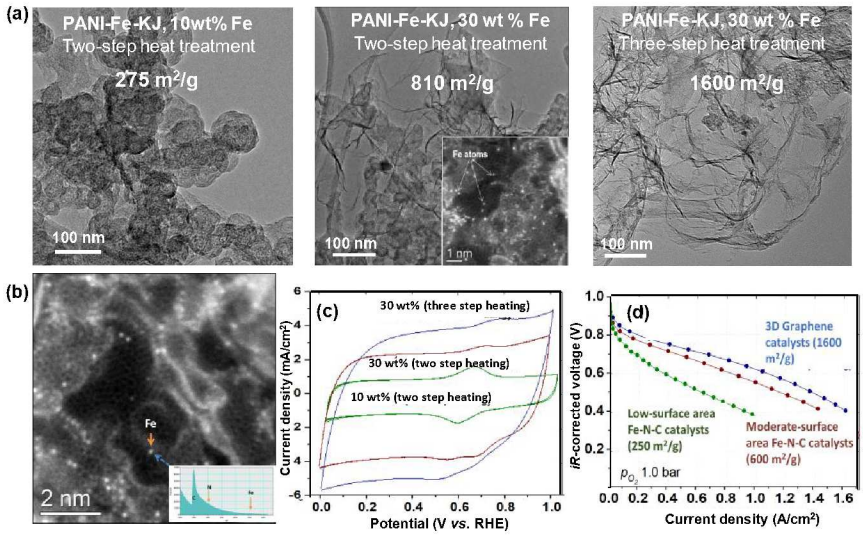

Fig. 14. (a) Overall morphologies of PANI-derived Fe-N-C catalysts synthesized from different methods showing different porosity and carbon nanostructures. (b) STEM/EELS analysis to determine the atomically dispersed and nitrogen coordinated Fe sites. (c) Cyclic voltammetry at 20 mVs^{-1} in 0.5 M H_2SO_4 solution to determine electrochemically accessible surface areas. (d) MEA performance with Fe-N-C cathodes: ~4.0 mg cm^{-2} 1.0 bar O_2, 200 sccm; membrane: Nafion® 211; cell: 80°C; 100% RH. Reproduced with permission.[213] Copyright 2014, American Chemical Society.

Following on our early work to develop PANI-based Fe-N-C catalysts,[50, 100, 181] we further discovered that the carbon morphologies and nanostructures are primarily dependent on the Fe content used during the synthesis. The higher Fe content, the more porous morphologies generated **(Fig. 14a)**.[213] The *in-situ* formation of FeS (sulfur from ammonium persulfate used as the oxidant to polymerize aniline) during the pyrolysis is a pore-forming agent, capable of generating highly porous and graphene-sheet like morphologies dominant with meso and macropores. Therefore, in a comparison of varying the Fe content and heating treatment step, three Fe-N-C catalysts were prepared to show significantly different surface areas and morphologies. Using 30 wt.% Fe content, a Fe-N-C catalyst with high-surface-area (>1600 m^2 g^{-1}) comprises nitrogen-doped 3D graphene-

like carbon. The catalyst contains a large quantity of atomically dispersed and nitrogen coordinated single Fe sites attached at the edge of graphene sheets (**Fig. 14b**). The higher Fe content during the synthesis generated larger electrochemically accessible surface areas (EASA) determined by using cyclic voltammetry (CV) in 0.5 M H_2SO_4 (**Fig. 14c**). In particular, when use extra-high Fe content of 30 wt.% along with additional heating treatments at 300 ^oC followed by traditional 900^oC enable to increase surface areas from 810 to 1600 $m^2 g^{-1}$ corresponding to much increased EASA. The corresponding MEAs studies also verified the importance of high surface areas and mesoporous graphene-like morphologies, generating the most top performance with a current density of 190 mA cm^{-2} at 0.8 V under H_2-O_2 at 1.0 bar conditions (**Fig. 14d**), which represented the best in the class of PANI-derived Fe catalysts by 2014.[214]

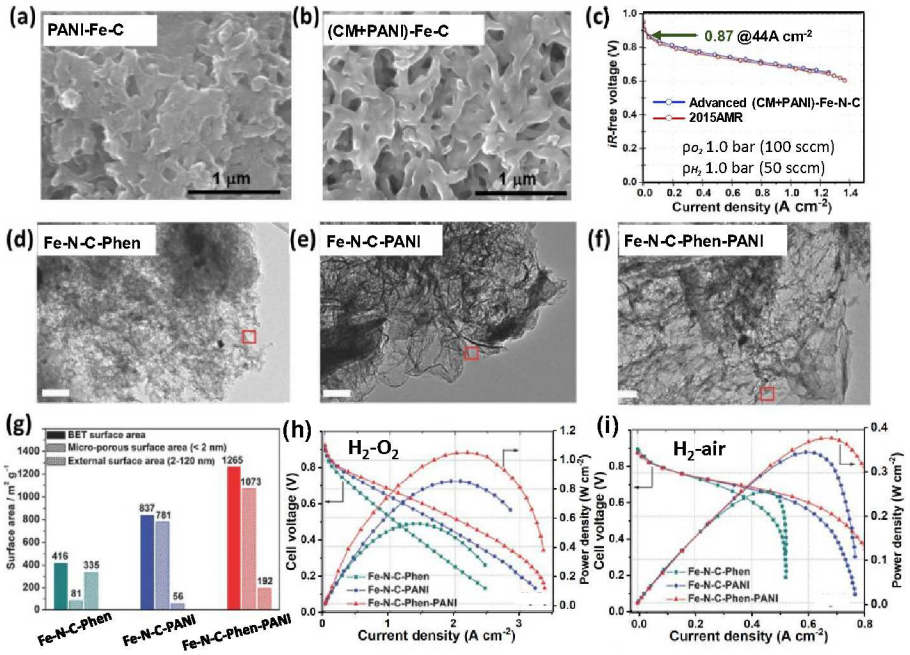

Fig. 15. (a-b) The hierarchical pore structure of the PANI-Fe-C catalyst and (CM+PANI)-Fe-C catalyst. Reproduced with permission.[24] Copyright 2017, American Association for the Advancement of Science. (c) H_2-O_2 fuel cell$_{iR\text{-}free}$ polarization plots of (CM+PANI)-Fe-C cathode catalyst. Reproduced with permission.[215] Copyright 2016, U.S. Department of Energy. (d-f) TEM images and (e) surface areas of the prepared Fe-N-C-Phen, Fe-N-C- PANI, and Fe-N-C-Phen-PANI catalysts. (f) H_2-O_2 and (g) H_2-air PEMFC. Reproduced with permission.[60] Copyright 2017, Wiley.

Designing multiple nitrogen/carbon precursors provides a new opportunity further to optimize the porosities and morphologies of Fe-N-C catalysts.[24,35,50] In addition to PANI, another effective precursor cyanamide (CM) was discovered and combined with PANI to prepare multiple nitrogen precursors-derived Fe-N-C catalysts.[24,216,217] Compared to the PANI (**Fig. 15a**), the decomposition temperature of CM is relatively lower. The gas generated during the decomposition of CM forms

various pores (**Fig. 15b**). Therefore, the PANI-CM-derived Fe-N-C catalyst is composed of fibrous carbon and several layers of graphene sheets, thus improving the distribution of ionomers in the catalyst layer and enhancing the accessibility of the reactants to FeN_4 active sites. The MEA with the Fe-N-C cathode generated a current density of 0.016 A cm^{-2} at 0.9 $V_{iR\text{-}free}$ or 0.044 A cm^{-2} at 0.87 $V_{iR\text{-}free}$ under H_2-O_2 at 1.0 bar (**Fig. 15c**).[24] This work further emphasizes the vital role of hierarchical pore structures in improving MEA performance. Following a similar double-nitrogen precursors approach, Chen's group discovered that the decomposition of phenanthroline (Phen) during the pyrolysis step expanded the covering PANI shells, producing a porous graphene-like skeleton (**Fig. 15d-f**).[60] Compared with the catalyst prepared by using only one nitrogen precursor, the Phen-PANI-derived Fe-N-C catalyst possessed both a high microporous surface area (1073 m^2 g^{-1}) and a larger external surface area (192 m^2 g^{-1}) (**Fig. 15g**). The MEA produced a current density of 0.39 A cm^{-2} at 0.8 $V_{iR\text{-}free}$ and a peak power density of 1.06 W cm^{-2} at 0.46 V under H_2-O_2 conditions (**Fig. 15h-i**). Ingenious combinations of dual nitrogen sources have resulted in unique graphene-like electrocatalysts with hierarchical nanoporosity, which significantly boosts MEA performance.

Electrospinning technology for hierarchical porosity engineering

Electrospinning catalysts with fiber-like morphologies can construct macroporous carbon structures, which still contain sufficient micropores in each nanofiber for hosting MN_4 active sites. The carbonized fibers are highly graphitized, reducing charge transfer resistance within the thick PGM-free electrode. Liu et al., at Argonne National Laboratory (ANL), reported a pioneer work to design PGM-free electrodes by using the electrospinning method in 2015.[204] Electrospinning a polymer solution containing ferrous organometallics and ZIF-8 followed by thermal activation is useful to produce an active and stable Fe-N-C catalyst. The ZIF-8 content in polymers is crucial

for generating optimal porosity with a balance among micro, meso, and macropores for maximum site density and the most favorable mass transport. Compared to traditional Fe-N-C catalysts with particle morphologies, the continuous network structure in the electrospun catalyst promotes the transport of electrons along the fibers, and the large pores between the fibers facilitate the mass transport of O_2 and H_2O (**Fig. 16a** and **b**). MEA tests indicated that the electrospun and fiber-like Fe-N-C catalysts generated volumetric activities of 3.3 $A \cdot cm^{-3}$ at 0.9 V or 450 $A \cdot cm^{-3}$ extrapolated at 0.8 V under H_2-O_2 at 2.0 bars (**Fig. 16c**). Compared to traditional Ketjenblack (KB) support Fe-N-KB catalyst (~0.3 $W \cdot cm^{-2}$), the peak power density of the electrospun and fiber-like Fe-N-C catalyst reached 0.9 $W \cdot cm^{-2}$ in an H_2-O_2 cell (**Fig. 16d**).[204] The MEA also demonstrated excellent water management behavior and maintained a smooth polarization curve even at the highest current density without any sign related to severe water flooding.

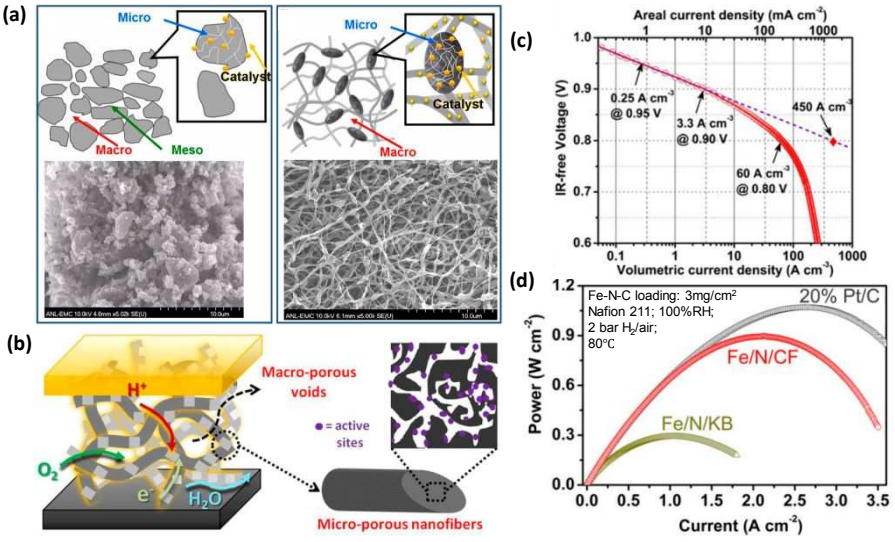

Fig. 16. (a) Comparison of the pore/active sites distribution of conventional carbon support Fe/N/KB (left) and nanonetwork catalyst Fe/N/CF (right). (b) The schematic demonstration of micropore-macropore architecture and charge/mass transfer model in the nanofibrous network Fe/C/CF catalysts. (c) Tafel plot of the kinetic activity and (d) power density curves of the representative catalysts in the H_2-O_2 cell. Reproduced with permission.[204] Copyright 2015, National Academy of Sciences.

Assembly methods for hierarchical porosity engineering

Apart from the nanofiber network morphology, nanosheet morphologies also allowed for enhanced accessibility to reactants by dispersing active sites at the surface of ultra-thin carbon nanosheets, therefore lowering the O_2 diffusion barrier and shortening diffusion path. Generally, assembling building blocks with different pore sizes generates a hierarchical porous morphology. One example demonstrated a rationale that is to design an architecture of in-situ polymerization of PANI on graphite mesoporous carbon spheres (MCSs).[60] A post thermal treatment produced a nitrogen-doped mixture of 2D graphene-like pieces and 3D porous carbon spheres in a Fe-N-C catalyst. The 2D/3D hybrid architectures in the catalysts facilitate mass transport due to the sufficient meso- and macropores. The predominant microporous structures host densely dispersed FeN_4 sites crossing the 2D graphene carbon and 3D MCSs. The high degree of graphitization of the carbon matrix derived from the PANI facilitated electron transport and enhanced corrosion resistance. MEA tests further confirmed the enhanced mass transfer and giving a high power density of 0.83 W cm^{-2} under H_2-O_2 at around 2.4 bar. Therefore, the catalyst with hybrid 2D and 3D carbon structures are considered as nanochannel reactors, which can catalyze the ORR with easily accessible active sites, effective mass transfer, and smooth charge transfer.

3.1.3 Catalysts particle size optimization

Well-designed ZIF-8-derived M-N-C catalysts usually feature with a homogeneous particle size distribution, which provides a great opportunity to engineer particle size with maximum active site exposure, optimal ionomer distribution, and porosity for boosting MEA performance. We have developed a facile synthesis method through varying the metal concentrations in methanol solution during the synthesis of ZIF-8, which can accurately control precursor crystal sizes in a large range from 30 to 1000 nm, and then transfer into catalyst particle sizes through a thermal activation at 1100^{o}C (**Fig. 17a**). The correlation between catalyst particle size and ORR activity was established, showing the smaller particle size, the higher ORR activity until down to 50 nm. As expected, the improvement is mostly due to the increased active sites exposed in the surface layers of catalysts. However, further reducing particle size to 30 nm leads to a fusion morphology showing declined activity (**Fig. 17b**). Importantly, Litster's group at Carnegie Mellon University (CMU) elucidated the correlation between the primary particle size of the catalyst and the integration with Nafion ionomers, which aims to optimize the performance of cathode in terms of proton conduction and O_2 transport.[218] In the study, a series of Fe-N-C catalysts with primary particle sizes varying from 40 to 600 nm was employed to prepare cathodes by casting catalyst ink onto the gas diffusion layer (GDL). Ideally, the ionomer forms a continuous film on the surface of the primary particle without excessive thickness to inhibit O_2 diffusion. **Fig. 17c** provides a schematic illustration for the ionomer distribution in small primary particle-modified GDE. X-ray computed tomography imaging at nanoscale resolution (Nano-CT) is powerful to evaluate the ionomer distribution in the cathode, which can display the ionomer distribution in these Fe-N-C cathodes. As shown in **Fig. 17d**, brighter regions in the images indicate a high concentration of the acidic groups in the ionomer, and thus the brightest regions reflect the concentration of the bulk polymer electrolyte.

In the 40 nm size catalyst, the majority of the ionomer is in thick films around the aggregates, and the interior of the large catalyst aggregates (>5 μm) is mostly free of ionomer despite using high ionomer content (I/C=1). Instead, the 600 nm size catalysts feature good ionomer infiltration and uniform primary particle coverage. The 60 and 100 nm catalysts present an intermediate case, where a greater fraction of ionomer infiltrates the aggregates, but there are still dense layers of ionomer around the large aggregates. Their MEA performance by using fully-humidified air and pure O_2 gases can elucidate the gas and proton transport properties through the cathode thickness. The 60-100 nm catalyst yielded the highest currents in both the high voltage activity and low voltage mass transport-limited regions of the polarization curve. Despite performing well in RDE testing (**Fig. 17b**), the smaller particle size (i.e., ~40 nm) catalyst showed low performance in MEA testing, where its apparent activity was below that of the 60-100 nm catalysts and was highly transport limited at lower voltages (**Fig. 17e**). The results indicate that the primary particles must be large enough to form a uniform film of ionomer throughout the surrounding pores, but small enough not to affect the intra-particle transport to the active sites. The electrochemical impedance spectroscopy (EIS) of the cells with various particle size cathode catalysts was measured (**Fig. 17f)**. The larger particles (150 and 600 nm) presented notably higher resistances, whereas the spectra for 40 nm and 100 nm size catalysts almost perfectly overlapped with the lowest resistance. The conductivity is dependent on a combination of factors, including the microporous carbon with higher intrinsic proton conductivity to provide a path between branches of ionomer, and larger particles with longer distances between ionomer to increase the inner particle water domain resistance. Therefore, the ionomer content should reach a balance between providing sufficient proton conductivity and minimum negative impact on O_2 diffusion and electrical conductivity.

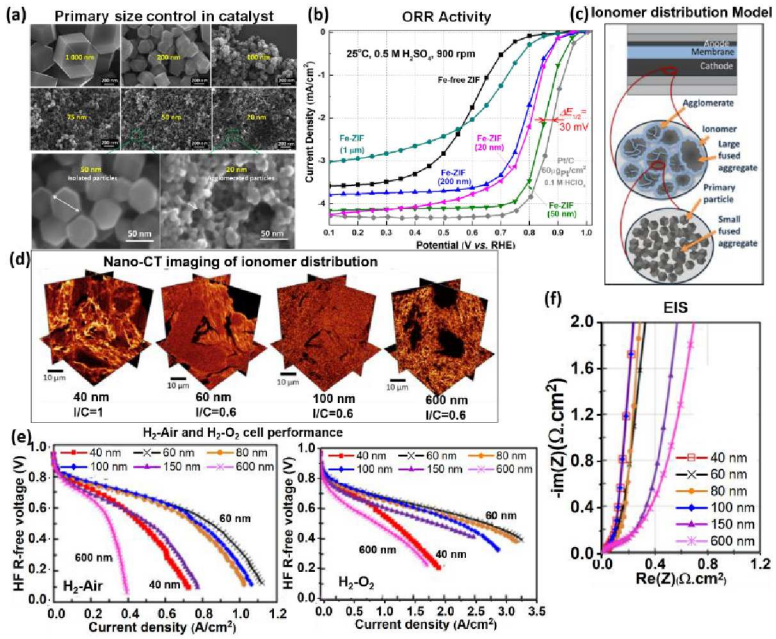

Fig. 17. (a) Primary particle size controls in ZIF-8-derived Fe-N-C catalysts. (b) ORR activity as a function of catalyst size from 1000 to 20 nm. Reproduced from permission.[85] Copyright 2018, American Chemical Society. (c) Schematic representation of the cathode catalyst layer structure. Ionomer distribution in the cathode catalyst layer. (d) Nano-CT imaging of the ionomer distribution in cathodes of Fe-MOF catalysts with different primary particle sizes and I/C: 40 nm-1, 60 nm-0.6, 100 nm-0.6, and 600 nm-0.6. (e) Fuel cell performance of Fe-MOF catalysts with different primary particles. Polarization curves obtained under air and O_2 for MEAs with cathodes prepared from Fe-MOF catalysts with different primary particles at 100% RH with I/C of 0.6. (f) EIS of the response of the cells with various particle sizes. Reproduced with permission.[218] Copyright 2019, American Chemical Society.

3.2. Optimizing cathodes through fabrication, modeling, and characterization

Due to low volumetric activity (A m^{-3}), M-N-C cathode catalyst layers (CCLs) (~100 μm) are usually an order of magnitude thicker than PGM CCLs (~10 μm). Fabricating PGM-free cathodes in MEAs with minimum mass and ionic transport resistance is more challenging.[219] Cathode-level transport losses can impose a tremendous penalty on PGM-free catalyst performance in MEAs. The extreme thickness, along with the hydrophilic carbon surface, yields a cathode that is highly sensitive to water flooding and massive proton ohmic/mass transport losses as protons/oxygen must be transferring across flooded and thick cathodes. The leading factors limiting M-N-C cathodes performance are electrode wettability, bulk proton conductivity, and ionomer tortuosity.[220] Furthermore, simultaneously increasing electrode hydrophobicity and ionomer conductivity could significantly improve cathode performance in MEAs. Mass transport within a very thick cathode presents a significant limitation. However, recent works demonstrated the effectiveness of optimizing CCL structures for MEA performance improvements.[221, 222] Therefore, a cathode with a well-dispersed ionomer and efficient water management is the key to achieving performance targets for PGM-free cathodes in MEAs.

3.2.1 Ionomer content influence

Besides the catalyst activity, MEA performance is sensitive to ionomer within the thick catalyst layer. In principle, first, the electrode ionomer (e.*g*., Nafion®) should introduce a high proton concentration and mobility at the catalyst sites. Second, the electrode ionomer should exhibit high conductivity to reduce ohmic losses across the cathode. Presently there is little understanding of how ionomers interact with M-N-C catalysts because the single metal active sites (e.g., FeN_4) are likely embedded within water-filled micropores. Thus, increased proton (acid) concentration of the low equivalent weight (EW) ionomers can kinetically enhance ORR reaction rates. Also, given the vast conduction distances in thick PGM-free cathodes, improved proton conductivity of

ionomers can significantly improve the uniformity of current density across the thickness of the electrode, increasing performance and extending lifetime.[223]

The ionomer distribution in cathodes depends on the dispersion of ionomer in "ink," the surface chemistry, and catalyst morphology. Therefore, adjusting the ionomer content has a profound effect on MEA performance and is easy to achieve experimentally.[224] In principle, high Nafion content benefits for performance improvement in the kinetic region. However, it blocks gas channels. Thus, oxygen and water transports would be limited in mass- transfer controlled voltage range. On the contrary, low Nafion content leads to a reduced proton conductivity corresponding to poor MEA performance throughout the voltage range.

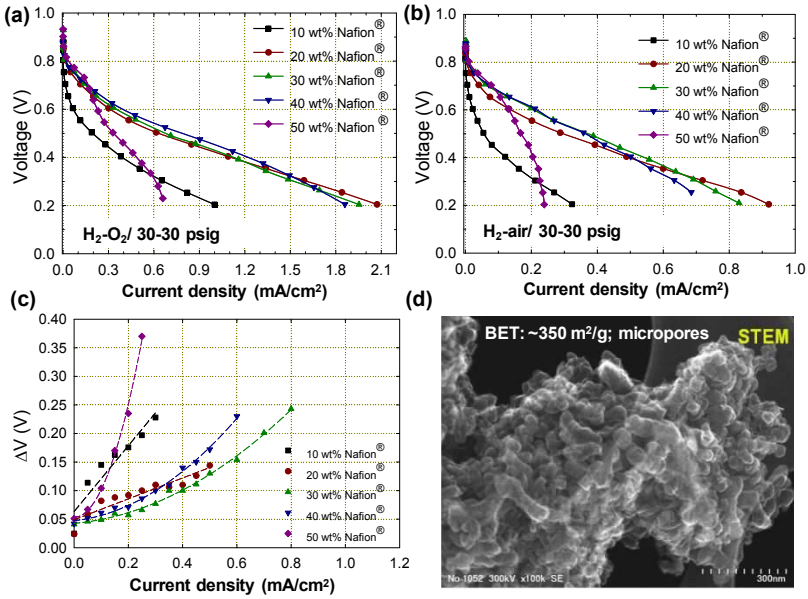

Fig. 18. (a and b) The effect of Nation content in PGM-free cathodes made from PANI-derived Fe-N-C catalysts on MEA performance measured under O_2 (a) and air (b) conditions. (c) The differences in voltages between O_2 and air indicates the mass transport resistance as a function of Nafion content. (d) Typical morphology of PANI-derived Fe-N-C catalysts.

We studied the effect of Nafion content from 10 to 50 wt.% on MEA performance by using PANI-derived Fe-N-C catalysts under both O_2 and air conditions (**Fig. 18a** and **b**).[225] With the extra-low Nafion content (10 wt.%), performance at both kinetic and mass transferred control ranges is lower due to the insufficient proton conductivity. Oppositely, with a high Nafion content such as 50 wt.%, performance at the kinetic range is enhanced. However, the MEA suffered from significant performance loss in the mass transport range. As for the specified PANI-derived Fe-N-C catalyst, the optimal Nafion content is around 30-40 wt.% generating the maximum performance in a wide voltage range. To theoretically study the effect of Nafion content on O_2 transport in the catalyst layer, the correlation between current density and ΔV is used as an indicator to determine the limitation of O_2 transport based on the Nester equation (**Fig. 18c**).[225] The ΔV means the difference of the voltages when using O_2 and air to generate the same current density. Hence, the smaller ΔV means easier O_2 transport in the cathode. According to this theoretical model, 30 wt.% Nafion content yield the most favorable electrode structures for the specified Fe-N-C catalyst that has relatively low BET surface area (~350 $m^2 g^{-1}$) dominant with micropores (**Fig. 18d**). This optimal value is similar to that often used for Pt/C cathode (*i.e.*, 35 wt.% Nafion).[226]

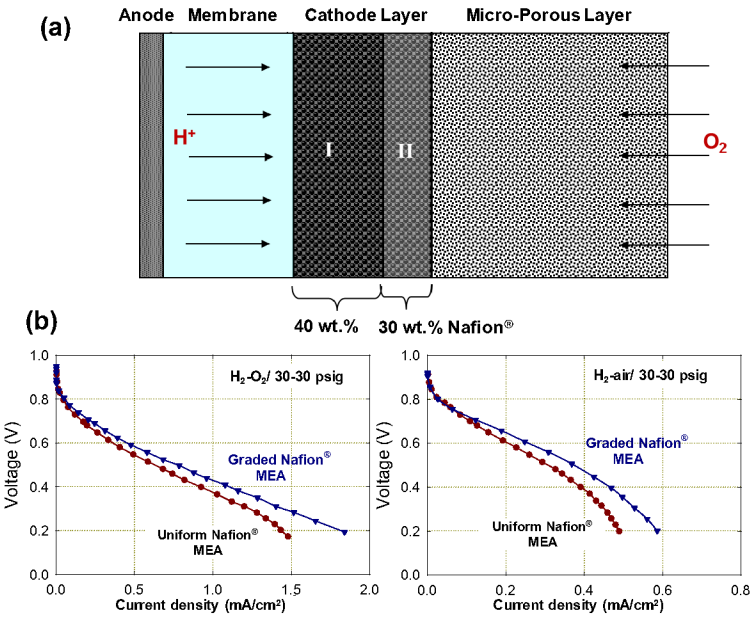

Fig. 19. (a) The scheme to demonstrate an innovative concept of designing a PGM-free cathode with gradient Nafion content: high Nafion content close to the membrane and the low Nafion content close to GDL aiming to improve proton and oxygen transfer from the opposite direction simultaneously. (b) Experimental results verified the gradient Nafion content in the cathode yield improved current density.

Others have demonstrated that a "graded-ionomer" concept is beneficial for MEA performance improvements.[225,227-229] The gradient Nafion content through M-N-C cathodes is to design higher Nafion content close to the membrane to facilitate proton transfer and lower Nafion content close to the GDL to improve O_2 transport. To simplify the model, here, for example, we just divided the cathode into two layers (**Fig. 19a**).[225] The cathode contains gradient Nafion content: 30 wt.% in half cathode close to GDL and 40 wt.% in the half cathode close to the membrane. Hence, protons and O_2 can diffuse into the cathode more easily from opposite directions. As a result, the extended overlapped area, where proton and O_2 can meet and react, increased the utilization of active sites

in the cathode to generate higher current density. As a comparison, a cathode contained a uniform Nafion content of 35 wt.%. The corresponding MEA performance of two cathodes is compared in both O_2 and air conditions (**Fig. 19b**).[225] The MEA with the cathode containing gradient Nafion content achieved improved current densities, especially in the low voltage range, without compromising the current density in the kinetic area. Therefore, using gradient distribution of Nafion content holds excellent promise to design cathodes with the optimal combination of proton conductivity and O_2 transport.

Banham and co-workers[222], and Yin *et al.*[230] found that optimal ionomer content for Fe-N-C catalysts is typically higher than 40 wt.%, especially for the latest catalysts with dominant micropore. EIS methods are useful in determining optimal ionomer content.[222, 231] When an optimal ionomer coverage is at the catalyst surface, the EIS spectra obtained in H_2/N_2 (anode/cathode) shows a 45º line in the high-frequency region, indicative of the ionic resistance in the CCLs.[232] Using an optimal Nafion content, Banham *et al.* demonstrated exceptionally high performance for a large (50 cm^2) MEA by using a Fe-N-C catalyst, reaching a peak power of 570 mW cm^{-2} with a current density up to 1.5 A cm^{-2} in mass transport regions under H_2-air conditions, highlighting the importance of rational catalyst layer design to overcome the transport issues in thick PGM-free electrodes.

3.2.2 Catalyst ink preparation and catalyst layer modification

Currently, main barriers of fabricating high-performance M-N-C cathode MEAs are (1) incomplete/non-uniform ionomer coverage, (2) thick layer of ionomer over catalyst surface, (3) inability to effectively repel water, and (4) poor ionomer/catalyst interfaces due to the hydrophobic surface of the highly graphitic catalysts. In general, the surface of M-N-C catalysts is highly hydrophobic after the pyrolysis, making the dispersion of them in water-based solvent extremely

difficult and often leading to poor MEA performance. Therefore, ink preparation is crucial for designing the active cathode layer with an appropriate pore structure and hydrophobicity. The goal is to disperse catalyst powder in optimal solvents to achieve the smallest particle size distribution. The proper match of the solvent and functionalized catalyst can lead to well-dispersed catalyst particles in the catalyst ink and rational utilization of catalyst pore structures. The relevant study, especially on M-N-C electrodes, is barely reported. Selection of different solvents/mixtures based on their dielectric constants (*e.g.*, a mixture: H_2O: IPA, ϵ_{H2O}=80.4, and ϵ_{IPA}=18.23) to match the M-N-C catalysts is the effective way to realize the optimal hydrophobicity. Using the *Zeta* potential of the mixture of a solvent and a solid particle can quantitatively guide the selection of optimal solvents for specified catalysts. The resulting morphologies of catalyst particles, ionomer particles, and the formation of the ionomer/catalyst interface in a catalyst ink can link to the ink preparation procedures. Appropriate functionalization of catalysts can effectively tune the surface hydrophobicity and break the catalyst agglomerates into primary particles. Therefore, it can achieve maximum ionomer/catalyst interfaces to control the pore volume, average pore size, and porosity, facilitating mass transport with improved MEA performance.

In addition to the selection of solvent for ink preparation, the use of additive is the key to controlling the hydrophobic domain across the thickness of the electrode for efficient gas transport. CMU's researches on comprehensive characterization[233, 234] and modeling[235, 236] indicated that, by using the CM-PANI-Fe catalyst developed by LANL, electrode wettability, the bulk proton conductivity, and tortuosity of the ionomer (only increasing ionomer loading is not beneficial due to increased mass transport losses) primarily limit the current density and power density at 0.7 V. The model developed by CMU also predicted that simultaneously increasing the hydrophobicity of the electrode and doubling the ionomer conductivity (without increasing ionomer volume

fraction) could yield a 50% increase in power density at 0.7 V.[235, 236] Early efforts included the addition of a small amount of polytetrafluoroethylene (PEFT) particles to improve the hydrophobicity of electrodes. However, uniformly and continuously dispersing PTFE particles in catalyst inks remains challenging. Further colloidal engineering in this area may yield a more effective method to evenly distributing PTFE particles or other relevant additives within the electrode to improve mass transport and water management. Hydrophobic dimethyl silicone oil (DMS) as an additive can introduce active three-phase interfaces in micropores of the Fe-N-C catalyst and provide sufficient hydrophobicity and mass transfer.[237] The key is to control the distribution of DMS on the Fe-N-C catalyst by screening the molecular weights, size, and viscosity of DMS. As the molecular weight of DMS increases, the permeability of DMS into micropores decreases. **Fig. 20a** illuminates that the well-controlled partial occupation of DMS with optimal molecular weight inside micropores alleviated the water flooding and can provide a robust O_2 transmission channel to the active sites. Therefore, the direct methanol fuel cells with the modified hydrophobic microstructure of the Fe-N-C cathode can deliver high power density and durability (**Fig. 20b**).

Recently, an effective method can covalently graft hydrophobic and electron-withdrawing trifluoromethylphenyl (Ar-CF_3) groups on the Fe-N-C catalyst (denoted as Fe-N-C-F) to achieve better water management in the CCL, as shown in **Fig. 20c**.[238] Surface fluorination can modify the hydrophobicity of a porous carbon matrix, because functionalization with fluorinated groups decreases surface energy, thus increasing the hydro-repellence.[239] It is common sense that increased contact angels of water droplets (ca. 165^o) on Fe-N-C-F materials surface means an improved hydrophobic property. However, this hydrophobic property only represents the overall external surface of the carbon matrix. Measuring the hydrophobicity of the microporous surface,

where hosts the active sites, is much more essential for evaluating the water management ability of catalysts. Proposed by Do *et al.*,[240] the following equation helps the understanding of the water adsorption inside the pores of porous materials:

$$C_{\mu} = C_{\mu s}\frac{K_{\mu}\sum_{n=6} X^{n}}{K_{\mu}\sum_{n=6} X^{n} + \sum_{n=6} X^{n-5}} + S_{0}\frac{K_{f}\sum_{n=1} nX^{n}}{1 + K_{f}\sum_{n=1} X^{n}}$$

Whereas S_0 is the density of hydrophilic functional group, K_f and $K\mu$ represent the chemisorption and the micropores equilibrium constant, respectively, $C_{\mu s}$ is the saturation concentration of water vapor in micropores. At the pressure region (P/P_o) below 0.20, water adsorption occurs around the hydrophilic functional groups induced by hydrogen bonding and the chemisorption, reflected by the parameter of S_0 *and* K_f. In the pressure region between 0.3 and 0.8, accumulated water vapor resulted in water clusters into micropores, indicated by the metric of K_{μ} and $C_{\mu s}$. Moreover, in a higher pressure region over 0.8, the growth of water clusters quickly diffused into the meso- and macro-pores. **Fig. 20d** provides a comparison of the accumulated water content in micropores for the Fe-N-C catalyst with or without fluorination. The smaller $K\mu$ value of Fe-N-C-F indicated the surface fluorination effectively impedes water condensation in micropores and thus benefits for mass transport in electrodes.

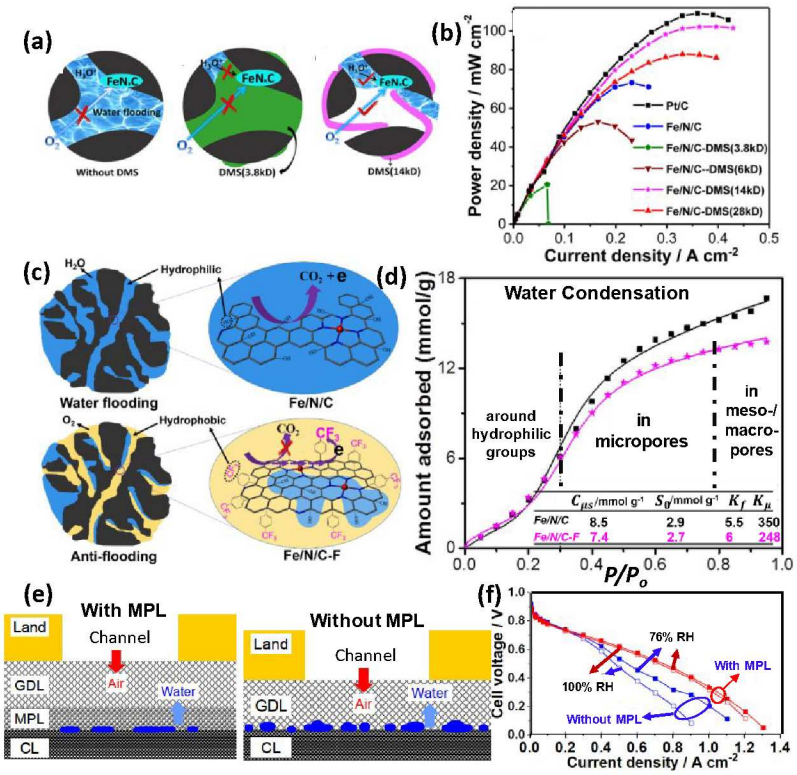

Fig. 20. (a) Scheme for the microstructure of Fe/N/C cathodes without hydrophobic DMS, (left) with DMS of small size (middle, *e.g.*, 3.8 kDa) and suitable molecular weight (right, 14 kDa). (b) Power density curves of direct methanol fuel cells with Fe/N/C-DMS cathodes. Reproduced with permission.[237] Copyright 2017, the American Chemical Society. (c) Trifluoromethylphenyl (Ar-CF_3) group functionalized Fe/N/C catalyst for preventing micro-pore water flooding and carbon corrosion. (d) Dynamic water vapor sorption isotherms (symbols) and fitting curves of Do-Do mode (line) of the two catalysts at room temperature. Reproduced with permission.[238] Copyright 2017, Wiley-VCH. (e) Schematic demonstration of water distribution on a cathode CL with and without the MPL and (f) Polarization curves of the H_2-O_2 cell at 35 °C. Reproduced with permission.[241] Copyright 2015, Elsevier.

The other strategy for mitigating water flooding and improving mass transport property is to modify the pore structure in CCL. Micropores of M-N-C catalysts are easily blocked by water due to their chemisorption ability. Thus, the possible water flooding in micropores hinders O_2 diffusion to active sites and destroys the effective three-phase interface.[242,243] As has discussed above, introducing mesopores and macropores to M-N-C catalysts-based CCL can alleviate the micropore flooding by offering more efficient water-draining out channels and freeways for reactants diffusion. Section *3.1* also provides several mesopore and macropore engineering strategies for addressing this issue.

Beyond catalyst-level, optimal designs of cathodes and GDL are critical to addressing mass transport issues to improve power density significantly. An electrospun Fe-N-C cathode, made from a mix binder of Nafion and polyvinylidene fluoride (PVDF), produced stable power output for 300 hours. On the contrary, the traditional sprayed electrode MEA with pure Nafion binder exhibited a power loss of 63 %. The comparison implies that the addition of hydrophobic PVDF to the nanofiber electrode binder helps improve the performance and durability of MEAs in the mass transport region.[244] Besides, it has recently been considered that a GDL designed with a microporous layer (MPL) has better anti-flooding performance than a GDL without MPL. Here, a wise water freezing method was applied to monitor the liquid water distribution in the cathode for investigating the effect and mechanism of MPL on inhibiting water flooding.[241] In this method, liquid water was trapped in the ice form by rapid freezing, and then the cell was disassembled for observations. The comparison of the areas covered by ice between the cells with and without an MPL suggested that MPL can suppress water accumulation at the CL/GDL interface due to its smaller pore size and close contact with CCL. This experiment supports the hypothesis that the interfacial gap between CCLs and MPL provided a buffer space for liquid water accumulation and

opened more free paths for gas transfer, as demonstrated in **Fig. 20e.** The enhanced MEA performance in **Fig. 20f** further verified the practical method of MPL utilization for water management, which provided another impetus for the cathode structure design to mitigate water flooding issues.

3.2.3. Characterization and models of CCL

High-resolution characterization of the structure and morphology of the CCL and the CCL/Nafion membrane interface is crucial for understanding the correlation of electrode fabrication, structures, and MEA performance. X-ray computed tomography (CT) is useful for characterizing 3D MEA to observe the anode, cathode, membrane, and interfaces virtually, as depicted in **Fig. 21a**. Especially the high-resolution Nano-CT can focus on electrode pore structures (pore size and distribution and catalyst geometry) and ionomer distribution.[218] Electrode structures also can be studied by using BET, Hg porosimetry, SEM, and TEM/3D TEM for ionomer/catalyst interfaces, Nafion ionomer network, and pore geometry in cathodes. These results are useful for both experimental MEA and modeling development.

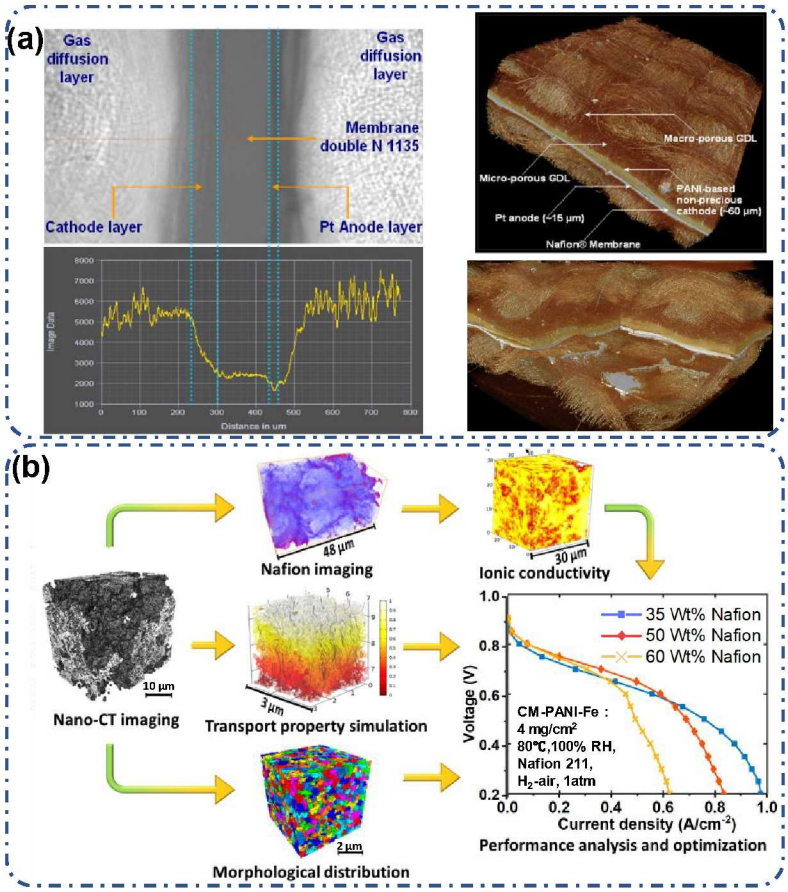

Fig. 21. (a) X-ray tomography can generate 3D images of the MEA structure. The various component in the MEA can be identified, such as GDL, anode, membrane, and PGM-free cathode. The thickness of PGM-free cathodes can be determined. (b) Resolving electrode morphology's impact on PGM-free cathode performance using Nano-CT of 3D hierarchical pore and ionomer distribution analysis. Reproduced with permission.[227] Copyright 2016, the American Chemical Society.

In addition to the time-consuming MEA fabrication and tests, the development of CCL models can guide to design optimal electrode structures for maximum reaction activity, efficient charger transfer, and mass transport. It can help experimental works to understand better and further mitigate the activity loss of M-N-C cathodes.[245] This method allows the generation of atomic-scale

structure-function relationships for catalysts, which are extremely difficult to be realized by experimental work.[17, 246] Only a few groups are dedicating to such modeling studies. In 2012, in collaboration with Zelenay, Kang et al., at LANL, developed a pore-scale simulation method based on the lattice Boltzmann method to predict the macroscopic transport properties in CCLs.[247] The quartet structure generation set can reconstruct high-resolution porous CCLs to show pore size distribution, specific area, and phase connectivity. The non-uniform distribution of ionomer in CCL generates more tortuous pathways for reactant transport. The tortuosity of CCLs is much higher than that adopted by the Bruggeman equation. Knudsen diffusion plays a significant role in O_2 transport and significantly reduces the effective diffusivity. Reactive transport inside the CCLs is also essential. Although the reactive surface area of the Fe-N-C CCL is much larger than that of the Pt/C CCL, the reaction rate is lower in the Fe-N-C CCL due to the much lower reaction rate coefficient (*i.e.,* lower TOF of the active sites). To further improve the performance of the Fe-N-C MEA, the enlarged reaction surface area would overcome the slow reaction rate coefficient. To enhance the microstructure of optimal reaction surface area is a topic of future studies. Theoretical studies indicated that the contribution of micropores in catalysts is little to mass transport. In contrast, mesopores or macropores are indispensable for accelerating mass transport rates.

In a series of related studies,[215, 224, 227, 228, 230, 235, 248, 249] Litster's group at CMU used nano-CT (with a resolution of about 50 nm) to provide an insightful understanding of the efficacy of Fe-N-C catalysts within the electrode as well as their correlation with electrode fabrication, morphology, and performance. For example, the pore/solid structure and ionomer distribution could be resolved into a 3D re-constructed structure from nano-CT imaging and transport simulation in three electrodes with the same Fe-N-C catalyst but varying Nafion contents. **Fig. 21b** displayed the hierarchical morphology reconstruction with differentiated solid, pore, and the pore-scale finite

element simulations studied ionomer domains and the mass (electronic, gas, and ionic) transport. Therefore, the MEA performance linked with electrode structures with verifying Nafion loadings. The optimal ionomer content around 35 wt.% shows the best mass transport compared with 50 and 60 wt.% cases, whereas exhibited relatively lower current in the kinetic region (inset in **Fig. 21b**).[227] The reason could be attributed to the insufficient infiltration of the ionomers into the micropores in the case of 35 wt.%. For the 50 and 60 wt.% contents, they delivered a similar performance in the kinetic region. However, 60 wt.% case presented a notable second Ohmic slope, indicating an excessive water flooding in the electrode. To be specified, the thick Nafion films of a higher ionomer content of 60 wt.% induces more hydrophilic pores, which would be easily flooded by water, as observed by the reduction of their associated pore volume. As a result, the O_2 diffusion path became significantly shortened, and an inactive region appeared near the membrane, therefore reducing the proton conductivity, evidenced by the second Ohmic slope in the polarization curve. Therefore, the combined experimental results with these modeling and simulation techniques are crucial in advancing both the catalyst pore size distribution/active site density modification and the electrode optimization for further boosting the MEA performance.

4 Strategies to mitigate catalyst and MEA performance degradation

In the past decade, scientists have made significant progress in improving the BOL ORR activity and MEA performance, through the rational design of atomically dispersed M-N-C catalysts with dense active sites and optimal porous structure. As their activity gradually approaches the actual requirement for PEMFC application, bridging the gap between the initially high activity and long-term durability has become an important topic for PGM-free catalysts. The goal for PEMFCs is an 8000-hour start-up/shut-down drive cycle or equivalent accelerated stress test (AST) with minimal performance loss (< 10 %) according to the U.S. DOE.[13, 250] A target of >25,000 hours further

stressed the challenge of durability for medium and heavy-duty transportation applications.[13, 251] Until now, long-term stability tests are rare for PGM-free cathode MEAs. In 2011, Wu and Zelenay reported that an MEA made from the PANI-derived FeCo-N-C catalyst run fairly stable for more than 700 h at 0.4 V in an H_2-air fuel cell.[181] However, the current density is around 0.3-0.4 $Acm^{-2,}$ and the energy efficiency at 0.4 V is only 32 %. Fuel cells should be operated at voltages above 0.6 V to provide more than 50 % energy efficiency. Unfortunately, a similar PANI-derived Fe-N-C cathode lost about 50 % performance at 0.6 V during the first 50 hours in an H_2-air MEA.[252, 253] Currently, the performance of MEAs with atomically dispersed highly active M-N-C cathodes often decreased 40-80 % during the first 100 hours of durability tests under practical operation conditions (> 0.6 V). M-N-C catalysts with a higher initial activity usually degrade faster at the initial stage. Although PGM-free and PGM cathodes could share a similarity of performance loss in MEAs, there are fundamental differences of degradation mechanisms between the atomically dispersed MN_4 sites embedded into carbon and the Pt nanoparticles. Generally, under oxidative and acidic ORR environments, transition metals and carbon are not thermodynamically stable. In addition to the likely metal dissolution, carbon oxidation occurs at 0.207 V in the presence of water. Fortunately, the transition metal sites (*e.g.*, Fe, Co, or Mn) are coordinated by four N ligands and further stabilized in carbon planes. Also, carbon corrosion is kinetically slow until the potential is beyond 1.0 V. Therefore, strengthening M-C bonds and modifying carbon local structures with improved corrosion resistance can enhance the intrinsic stability of the metal centers. However, the detailed degradation mechanisms of the M-N-C remain unknown yet. The degradation mechanism of the MEAs is even more complicate than the catalysts tested using RDE in aqueous electrolytes. Besides active site degradation, the collapse of the three-phase interface and water flooding in the cathode also cause severe proton and O_2 transport resistance. Unlike aqueous

electrolytes, the confined H_2O_2 formed in the cathode of an MEA is even more hazardous, causing free radicals to attack active sites and carbon support. However, most of the stability studies focused on the activity loss through AST by using RDE in aqueous electrolytes. Long-term durability studies of MEAs are rare due to the facility limitation and time-consuming reasons. Therefore, the primary work is to excavate the degradation mechanisms of M-N-C in both catalysts and cathodes during long-term fuel cell operation, thereby guiding for addressing the grand stability and durability challenges. Currently, four primary degradation mechanisms have been examined for M-N-C cathodes: (i) H_2O_2 or hydroperoxyl radical oxidative species attack, (ii) active site degradation caused by demetallation or C/N corrosion, (iii) protonation of active sites, and (iv) possible micropore flooding in catalysts.[254] In this section, we focus on the following two main categories to elucidate the possible degradation mechanism of M-N-C catalysts and cathodes. One is the activity loss due to the decomposition of MN_4 sites at the atomic level. The other is the performance loss of cathodes at the mesoscale or macroscale. Then, based on current understandings, we propose possible strategies to mitigating the inevitable stability/durability degradation of the most promising M-N-C catalysts in MEAs.

4.1 Mitigating hydrogen peroxide-induced degradation

Hydrogen peroxide, which is a by-product of the ORR through the indirect four-electron path or undesired two-electron path, promptly generates radical oxygen species (ROS) once meet with Fe ions through the Fenton-type reaction. Either H_2O_2,[251, 255] or the as-generated ROS[256, 257] could damage the integrity of the active sites or the carbon support, as well as membranes and ionomers, thereby causing a severe decay of MEA performance. For H_2O_2 induced performance degradation, the primary task is to reveal the way how the active sites or carbon support was damaged by H_2O_2

and the reason for activity decay either caused by the loss of active sites or the decreased intrinsic activity of active sites.

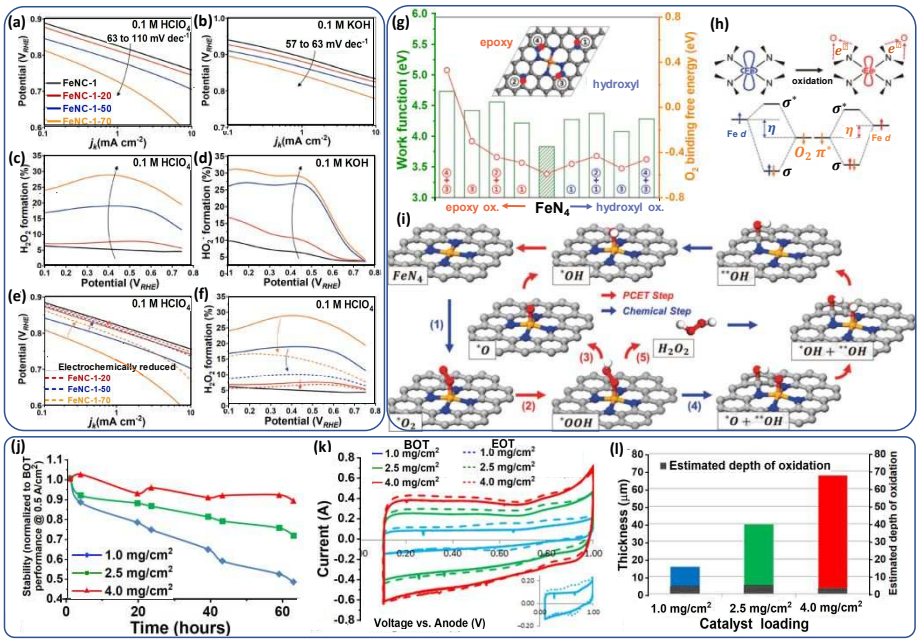

Fig. 22. (a-d) ORR activity and selectivity of the Fe-N-C catalysts before and after acidic H_2O_2 treatment at different temperature in acidic and alkaline electrolyte. (e-f) ORR activity and selectivity recovery after electrochemical reduction in 0.5 M NaCl. (g) Electron work function and O_2-binding energy of the active sites with two oxidation types on different carbon sites. (h) Schematic illustration of the electron-donating property at FeN_4 center after oxidation. (i) Different ORR pathways at FeN_4 active sites and the neighboring oxidized carbon atoms, respectively. Reproduced from permission.[257] Copyright 2018, The Royal Society of Chemistry. (j) Galvanostatic stability test of Fe-N-C catalysts-based MEA under air/H_2 with CCL design of different catalysts loading. (k) Double layer charge variation of the CV curves for each MEA before (BOT) and after (EOT) stability test. (l) CCL thickness and estimated depth of surface carbon oxidation of each MEA. Reproduced with permission.[5] Copyright 2018, American Association for the Advancement of Science.

Early in 2003, H_2O_2 treatments were developed to investigate the degradation of Fe-based ORR catalysts.[251] The results indicated that the activity decay is due to the nitrogen atom oxidation rather than the iron loss via observing the isomer shifts and half-width increase in Mőssbauer spectra after H_2O_2 treatment. However, this hypothesis is not convincing for the N 1s binding energies that are not changed if they are oxidized. Recently, a similar H_2O_2 treatment strategy in a combination of advanced characterization techniques and DFT calculations provided an understanding of the specific H_2O_2-induced ORR activity and selectivity degradation mechanism.[257] The ORR activity and selectivity of pristine (denote as Fe-N-C-1) and H_2O_2-treated (Fe-N-C-1-T, T represents the temperature) Fe-N-C catalysts were compared in acidic and alkaline media. The primary Fe-N-C-1 catalysts (comprised of 20% Fe content on the surface within FeN_xC_y moieties) did not leach out during the ORR procedure in an acidic electrolyte based on their previous report, excluding the possible activity degradation caused by the loss of Fe ions.[59] As displayed in **Fig. 22a** and **c**, the Tafel slopes were similar except the case of treatment at 70 ℃ in the acidic electrolyte, implying that the ORR RDS changed at 70 ℃ in acidic electrolyte. On the contrary, the activity and selectivity of H_2O_2-treated catalysts were identical to the pristine one in the alkaline medium (**Fig. 22b** and **d)**. However, the selectivity was much higher than those in the acidic electrolyte, assigning to the more durable binding of HO_2^- than H_2O_2 onto the active sites in alkaline medium. The nitrone spin trap and electron paramagnetic resonance spectra identified the ROS generation from Fe^{3+} ions, and H_2O_2 was pH-dependent, only occurs in acidic solution. Furthermore, it is interesting to found that the physical structure (i.e., pore size distribution, specific surface area, and bulk carbon structure) of the H_2O_2-treated Fe-N-C kept unchanged. At the same time, some minor changes in chemical properties occurred, including the

coordination environment modification of the FeN_xC_y moieties and the 2-fold oxygen content increase. These results suggested selective oxidation of the top-surface carbon atoms around FeN_x moieties by ROS, which was supposed to account for the decrease of the ORR activity with a lower TOF of FeN_xC_y active sites. The recovery experiment further verified this hypothesis by removing the oxygen functional groups through electrochemical reduction, a method similar to the graphene oxide electrochemical reduction.[258] **Fig. 22e** and **22f** show that the recovery of activity and selectivity is high but not complete, especially for Fe-N-C-70, because of the difficulty of the removal of epoxy groups. In addition to experimental observations, theoretical DFT calculations predicted the relationship between performance degradation (i.e., TOF and selectivity) and the surface carbon oxidation. The O_2-binding energy dramatically decreased, and the electron work function elevated as a result of modifying the carbon support with electron-withdrawing groups (hydroxyl and epoxy groups), thus downshifting the Fe-d band center and reduced their oxophilicity (**Fig. 22g** and **22h)**. DFT calculation also explained the change of selectivity regarding the change of RDS steps (**Fig. 22i**), implying that the indirect 2e +2e transfer path for the formation of H_2O_2 is more favorable as a result of surface carbon oxidation adjacent to the FeN_4 moieties.

This H_2O_2 or ROS-induced surface carbon oxidation is one of the significant degradation mechanisms for the M-N-C catalysts in MEAs. The hypothesis was examined by studying the stability of three different Fe-N-C catalyst loadings (1, 2.5 and 4.0 mg cm^{-2}) at a galvanostatic mode test at 0.5 A cm^{-2}.[5] Because the majority of the current for the PGM[259, 260] or PGM-free-based CCL[261] is generated at the CCL/membrane interface. The thinner CCLs might suffer from more severe current loss due to the H_2O_2 attack, especially for the indirect 2e+2e ORR process, than the thicker ones, which have their larger "buffer zone" with less H_2O_2 generation. As expected, the 4.0 mg cm^{-2} loading design exhibited the best stability, with only 10 % initial performance loss

after 60 hrs (**Fig. 22j**). Therefore, this loading-dependent stability analysis further verified the primary degradation mechanism through H_2O_2-induced surface carbon oxidation versus micropore flooding by comparing the variation of the double-layer charge (DLC) in the CV. As for a lower loading CCL design (1.0 mg cm^{-2}), H_2O_2-induced surface carbon oxidation may result in the appearance of pseudo-capacitive peaks with increased DLC, while micropore flooding may lead to a uniform increase in DLC due to a higher production of volumetric water. The variation of the DLC is consistent with the prediction from H_2O_2-induced surface carbon oxidation (**Fig. 22k)**, where the pseudo-capacitive peaks occurred at 0.6 V and 0.8 V. This suggested that the primary degradation mechanism might be the H_2O_2 or ROS induced surface carbon oxidation. Moreover, as the loading increase, the percentage of the surface oxidation decreases due to the severe degradation rate in the membrane/CCL interface (**Fig. 22l**). These results do suggest that CCL thickness optimization is an effective strategy to improve the stability/lifetime of PGM-free-based MEAs. However, the formation of a thicker catalyst layer leads to limited diffusion and may cause the catalyst to undergo an oxidative attack by H_2O_2 trapped in the catalyst layer. Therefore, a joint strategy that combined with both catalyst and CCL modification is more reasonable and applicable for the MEA performance improvement.

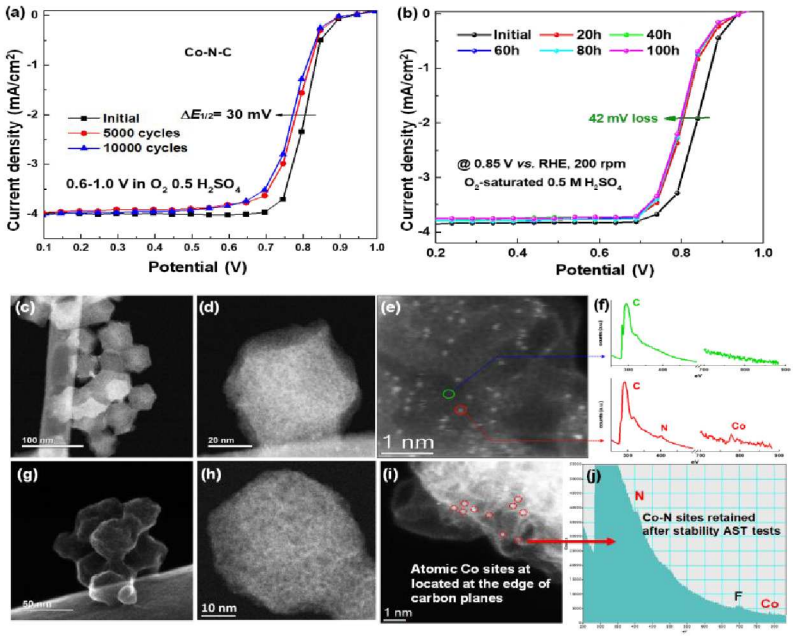

Fig. 23. Stability tests of a ZIF-derived atomically dispersed Co-N-C catalysts in O_2 saturated 0.5 M H_2SO_4 solution: (a) potential cycling from 0.6 to 1.0 V and (b) holding at the constant potential at 0.85 V for 100 hours. (c-f) STEM and EELS analysis for the Co-N-C catalyst before (c-f) and after (g-i) potential cycling stability tests. The carbon corrosion is significantly likely responsible for the initial activity loss. Co-N bonds remain stable during the ORR in a wide potential window. Reproduced after permission.[104] Copyright 2018, Wiley-VCH.

Three strategies have been explored toward catalyst modification for alleviating H_2O_2 or ROS attack during the ORR catalysis. First, engineering FeN_x active sites enhances the four-electron selectivity with minimal H_2O_2 generation during ORR catalysis. [159, 160] Second, the development of Fe-free M-N-C catalysts mitigates the Fenton reactions to minimize ROS generation (such as Co and Mn).[18, 91, 104, 105, 116, 262, 263] Third, addition ROS scavengers, such as CeO_2, is feasible.[264] Unlike the continuous activity loss observed in the Fe-N-C catalyst, the Co-

N-C catalyst conveys excellent stability after the initial degradation in both potential cycling from 0.6 to 1.0 V (**Fig. 23a**) and constant potential holding at 0.85 V (**Fig. 23b**) in O_2-saturated 0.5 M H_2SO_4 **(Fig. 23b)**.[104] Based on the STEM imaging and EELS analysis of Co-N-C samples before (**Fig. 23 c-f**) and after (**Fig. 23 g-j**) the stability test, the apparent carbon oxidation associated with unstable active sites is the main reason for the rapid initial decay. However, the remaining CoN_x active sites (**Fig. 23j**) are more stable against the H_2O_2 attack, although Co-N-C catalysts may generate more H_2O_2 during ORR catalysis than Fe-N-C catalysts. The reason lies in the difference in the metal cations and H_2O_2/ROS redox potential, given the following equations:

$$H_2O_2 + H^+ + e^- \leftrightarrow \cdot OH + H_2O \quad E^o = 0.88\ V$$

$$Co^{3+} + e^- \leftrightarrow Co^{2+} \quad E^o = 1.92\ V$$

$$Fe^{3+} + e^- \leftrightarrow Fe^{2+} \quad E^o = 0.77\ V$$

The Fenton reaction is thermodynamically favorable for Fe ions over Co ions.[265, 266] Under the attacks of H_2O_2 and the derived ROS, the atomically dispersed Co sites coordinated with N atoms at the edge of the carbon plane are stable during the ORR in acidic media, while serious carbon corrosion happens. Increasing graphitization degree of carbon to enhance stability while maintaining enough dopants for activity improvements is a challenging task in the future for advancing Co-N-C catalysts

Another alternative strategy for eliminating ROS generation is by adding ROS scavengers. The ROS removal mechanism via adding CeO_2 is due to the Ce^{3+}/Ce^{4+} conversion through the following reaction equations:

$O_2 + 2H^+ + 2e \rightarrow H_2O_2$, (1)

$$2CeO_2 + 2H^+ + 2e \rightarrow Ce_2O_3 + H_2O, (2)$$

$$Ce_2O_3 + H_2O_2 \rightarrow 2CeO_2 + H_2O. (3)$$

CeO_2 can eliminate the generation of H_2O_2 in the ORR cathode.[264] In a phenylenediamine-based Fe-N-C catalyst, as expected, the yield of H_2O_2 evaluated by RRDE measurement is significantly lower with the optimal addition of CeO_2 in the catalyst. *In situ* removal of oxygen functional groups from the oxidized carbon for recovering ORR activity/selectivity also provide another hint for improving the stability of M-N-C catalysts.[257, 258]

4.2 Alleviating metal leaching and demetallation

Early studies have reported the occurrence of transitional metal leaching in M-N-C catalysts-based MEA (especially Fe-N-C catalysts) under controlled potential range operation. These results stated that the demetallation rate and extent were dependent on potentials.[252] Most of the Fe demetallation during the fuel cell operation originates from the inactive and acid-soluble iron species (e.g., Fe nanoparticles/oxides/sulfides/carbides).[217, 252] As for FeN_4 sites, redox of Fe^{3+}/Fe^{2+} during the ORR might lead to the demetallation under high potential, because of the smaller ionic radius of Fe^{III} than Fe^{II}.[267] However, metal leaching is likely a minimum for the atomically dispersed M-N-C catalysts with very low metal content (<2.0 wt%). It seems not to be responsible for the rapid initial performance loss within the first several hours.[59, 252, 268] Choi *et al.*[268] designed an operando scanning flow cell (SFC) connected to an inductively coupled plasma mass spectrometer (SFC/ICP-MS). Then they determined the hypothesis of the possible Fe demetallation for three Fe-N-C catalysts under steady-state fuel cell operation (**Fig. 24a**). The first catalyst contains FeN_xC_y active sites, free Fe, and encapsulated Fe nanoparticles by graphite carbon (denoted as

FeNC-wet-1 based on the wet-impregnation step and 1wt% Fe content in the precursor). The second one only comprises FeN_xC_y active sites without undetectable Fe particles (denoted as FeNC-dry-0.5). The third one consists of FeN_xC_y active sites and a low amount of Fe nanoparticles (FeNC-dry-1). Because the conversion of the insoluble Fe^{III} hydroxide to soluble Fe^{II} cations is thermodynamically favorable at low pH according to their redox potential of E^o=0.77 V.[59] For FeNC-wet-1 catalysts, significant leaching occurred (ca. 705 $\mu g_{Fe}\ g_{catal}^{-1}$ for initial 20 CV cycles) as expected at a potential below 0.7 V_{RHE}. Oppositely, the *ex-situ* electrochemical CV cycle and the $SnCl_2$/HCl solution treatment ($SnCl_2$ acting as the reducing agent for assisting the Fe species removal) result in less Fe leaching of ca. 79 $\mu g_{Fe}\ g_{catal}^{-1}$ and 150 $\mu g_{Fe}\ g_{catal}^{-1}$ for the FeNC-dry-1 catalyst, respectively. As for the FeNC-dry-0.5 catalyst, the detected Fe is the smallest <10 $\mu g_{Fe}\ g_{catal}^{-1}$, suggesting the superior stability of FeN_x moieties in the harsh acid environment with a potential range of 0-1.0 V_{RHE}. Regarding the Fe leaching amount in three catalysts, their decay during the 50-hours fuel cell test is similar in both the kinetic and mass transport regions (**Fig. 24b**). Their Tafel slopes (**Fig. 24c**) and current densities (**Fig. 24d**) were in parallel, with no correlation with their Fe demetallation rates. Therefore, the primary degradation mechanism for these Fe-N-C catalysts-based MEA is not likely due to the leaching of free Fe particles. Alternatively, the hypothesis of the H_2O_2/ROS-induced degradation mechanism was then proposed by correlating current densities with cumulative Faradic charge (nearly identical slopes in **Fig. 24e**). Because the cumulative Faradic charge should proportional to the electro-reduced O_2 molecules and thus H_2O_2 by-products/ROS amount. These leached Fe ions in cathodes do not cause a severe issue of membrane and ionomer due to cation contamination in a short time. However, in practical catalyst synthesis, acid leaching step often employed as a post-treatment can minimize the demetallation issues by removing all the instable metal species.

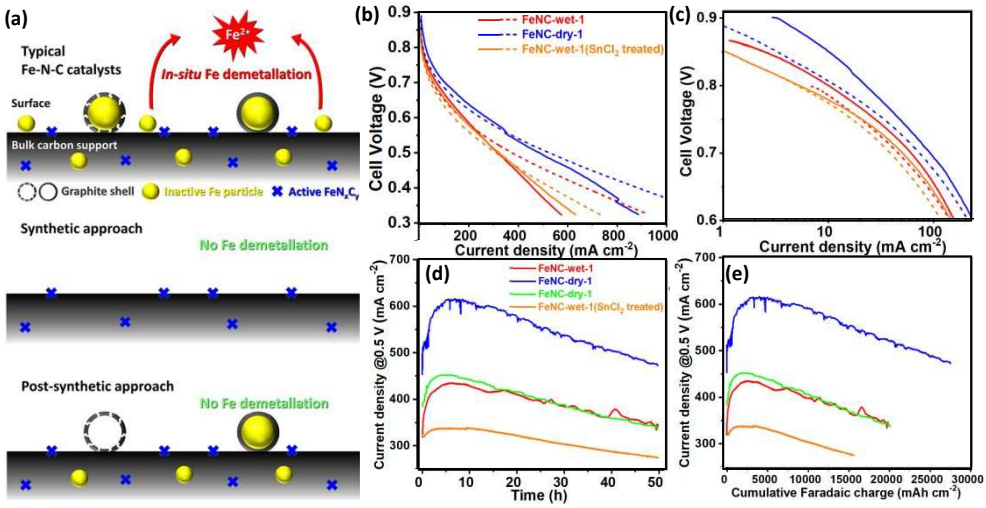

Fig. 24 (a) Schematic demonstration of the morphology of three types of Fe-N-C catalysts comprised of inactive free Fe particles, partially and fully encapsulated Fe particles by graphite layers and active FeN_x moieties, respectively. (b) Polarization curves and (c) Tafel plots of the catalysts before and after 50 h fuel cell operation at 0.5 V. (d) Current density degradation. (e) Corresponding current density @ 0.5 V vs. cumulative faradic charge. Reproduced from permission.[268] Copyright 2016, American Chemical Society.

In addition to the leaching of unstable metal species from catalysts, the demetallation of MN_4 sites directly degrades the catalyst by losing the intrinsic activity. The demetallation of MN4 sites is associated with the H_2O_2/ROS-induced attack. The carbon oxidation might accelerate the decomposition of MN_4 active sites. When FeN_4 sites adsorb hydroxyl free radicals, they are entirely "pulled" out of the carbon plane due to the elongated Fe-N bond. The likely Fe-N bond-breaking generates free Fe ions and form clusters.[269] Also, the leached Fe ions acting as the Fenton reaction catalysts, in turn, exacerbate the carbon oxidation/corrosion. Like a chain reaction, the resulting carbon corrosion further leads to the continuous decomposition of the MN_4 moieties,

hence continuously causing active site loss and leaching of metal ions. These free released cations may contaminate the ionomers and the Nafion membrane. The contamination also hinders proton conduction[59,269] and reduces O_2 permeability,[270,271] which eventually results in the performance decay. However, the understanding of the effect of ionomer and membrane contamination by these free metal ions are remained unresolved. Mitigating demetallation is likely to be realized by synthesizing homogenous M-N-C catalysts with exclusive MN_4 active sites in the absence of inactive and soluble metal aggregates. For example, the Fe-doped ZIF-8-derived methods have been proved useful for synthesizing Fe-N-C catalysts with stronger Fe-N bonding and high density of FeN_4 moieties,[85, 101], therefore, exhibiting enhanced stability relative to others.

4.3 Minimizing carbon corrosion

Unlike Pt/C catalysts in which carbon acts as the conductive support, the carbon matrix in M-N-C materials not only serves as an electronic conductor but also as the host for active site stabilization. With carbon being the main component in M-N-C catalysts (> 90 at. %), the corrosion of the carbon is fatal to the catalyst stability due to the separation of MN_4 active sites from carbon planes and the loss of electrical contact.[272, 273] In fuel cell cathodes, the occurrence of carbon corrosion is inevitable due to the high operating potential (up to 0.9 V) is often above the thermodynamic equilibrium potential of CO_2 evolution (0.207 V *vs*. SHE). Still, the kinetics of carbon oxidation is often slow below 0.9 V. Also, the harsh conditions, including 100 %RH, elevated temperature (80 ^oC), and acidic conditions, further accelerate the oxidation process. Other factors, like demetallation or H_2O_2/ROS attacks, might aggravate this issue. In addition to the reduced electrode conductivity, carbon corrosion may also weaken the M-N and N-C bonds, ultimately resulting in the deactivation and decomposition of MN_4 active sites.

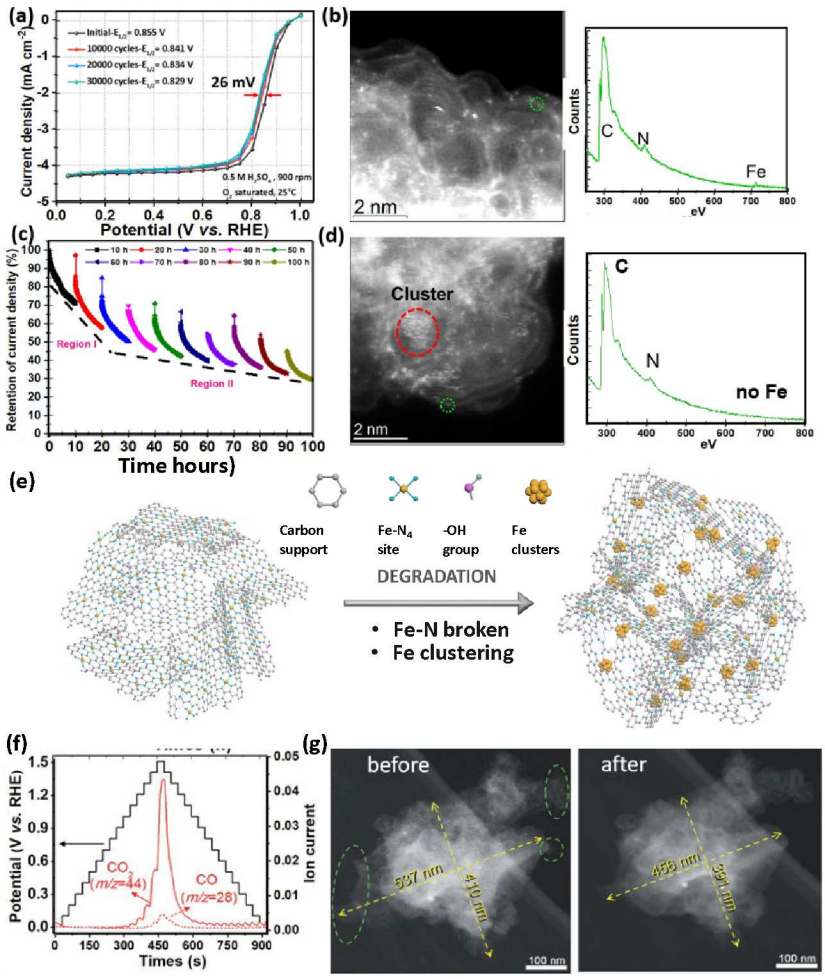

Fig. 25. (a) ORR performance after AST potential cycling between 0.60 and 1.0 V. (b) STEM and EELS analysis of Fe-N-C catalyst after potential cycling test. (c) Durability potentiostatic test by holding at a constant potential of 0.85 V for 100 hours. (d) STEM and EELS analysis of Fe-N-C catalyst after the potentiostatic test. Reproduced with permission.[101] Copyright 2019, Royal Society of Chemistry. (e) A scheme to show the degradation mechanisms of FeN_4 sites associated with Fe-N broken and Fe clustering. (f) Online SFC/DEMS signals as responding to a stepwise chronoamperometry test between 0 and 1.5 V at 50 °C. (g) Operando studies of carbon oxidation of a Fe-N-C catalyst by using dark-field IL-STEM micrographs before and after 5000 cycles

performed between 1.2 and 1.5 V at 50°C in 0.1 M $HClO_4$ electrolyte. Reproduced with permission.[59] Copyright 2015, Wiley-VCH.

We used the post-mortem electron microscopy analysis to gain insight into possible catalyst degradation mechanisms related to carbon corrosion and Fe-N coordination cracking.[101] In an O_2 saturated 0.5 M H_2SO_4 electrolyte, the initial $E_{1/2}$ value loss of the Fe-N-C catalyst is about 30 mV under the 40,000 AST potential period (0.6-1.0 V) (**Fig. 25a**), suggesting reasonably good retention of FeN_4 sites in the Fe-N-C catalyst. STEM-EDS images coupled with and EELS analysis (**Fig. 25b)** further confirmed the insignificant carbon corrosion, because the polyhedral particles are nearly intact with similar particle size and shape when compared to the catalysts before the AST. Meanwhile, Fe-N bonds remain stable even under the electron beam during the EELS analysis, showing the co-existence of Fe and N at the atomic level. However, a more stringent potentiostatic test at a potential of 0.85 V for 100 hours causes significant activity loss. During the stability test, a partially recovered ORR activity recorded every 10 hours may be due to the electroreduction of the surface functional groups adjacent to the FeN_4 position (**Fig. 25c**). However, the catalyst suffered from significant irreversible degradation, especially in the first 20 hours, losing about half of the original ORR activity. The round and agglomerated catalyst particles observed in the HAADF-STEM image indicate severe carbon corrosion after the potentiostatic stability test at 0.85 V. The appearance of Fe nanoclusters and the disappearance of Fe and N signals in STEM-EELS (**Fig. 25d**) indicated the breaking of Fe-N bonds and the loss of FeN_x active sites. Therefore, carbon corrosion and Fe-N breaking in Fe-N-C catalysts probably account for the performance degradation. As the demetallation is not likely to occur at 0.85V, the loss of the active sites was perhaps originated from the carbon corrosion and gradually detached from their host.

Based on these insightful understanding, we present a scheme to elucidate the possible degradation of Fe-N-C catalysts associated with the Fe-N bond breaking and Fe clustering caused by the carbon corrosion under harsh conditions during the ORR (**Fig. 25e**).

Another work further verified this hypothesis that carbon corrosion has a detrimental impact on catalyst stability. Operando techniques, including ICP-MS and differential electrochemical mass spectroscopy (DEMS) combined with identical location-scanning transmission electron spectroscopy (IL-STEM), were developed to study the carbon oxidation of a Fe-N-C catalyst in high potential range cycling range (*i.e.,* 1.2-1.5 V) with the loss of FeN_x active sites.[59] As mentioned before, by comparing the CV curves before and after the stability test, an uneven increase in the DLC and the appearance of new pseudocapacitive peaks at 0.6 V and 0.8 V suggested the formation of oxygen-containing groups at the carbon surface. The as-collected online SFC/DEMS data under chronoamperometric test conditions (**Fig. 25f**) signified the occurrence of CO_2 evolution at potentials over 0.9 V. According to the line profiles in EDX active sites loss as the consequence of the carbon corrosion, a noticeable reduction in Fe and N content after cycling directly validated active sites loss as the consequence of the carbon corrosion. The intensity of the Fe dissolution signal obtained from the SFC/ICP-MS data is proportional to the rate of carbon oxidation derived from the SFC/DEMS data. The Fe dissolution in the high-potential range can link to carbon oxidation. More interesting is that high potential cycling not only caused the oxygen-containing group functionalization at the carbon surface but also resulted in the shrinkage of the carbon particle shape and decrement of layer or carbon wall thickness. **Fig. 25g** shows dark-field micrographs of an isolated Fe-N-C particle before and after 5000 potential cycles performed between 1.2 and 1.5 V at 50 °C in a 0.1 M $HClO_4$ electrolyte. The disappearance carbon protrusions (marked in-dash circles), 5-15 % 2D size shrinkage, and the weakened image contrast

(meaning the thinner carbon layer) are apparent by comparing the carbon particle before potential cycling. Also, the relevant morphological changes caused by carbon corrosion, such as active surface area and the pore size distribution, result in the additional hindrance of O_2 diffusion and charge transfer.

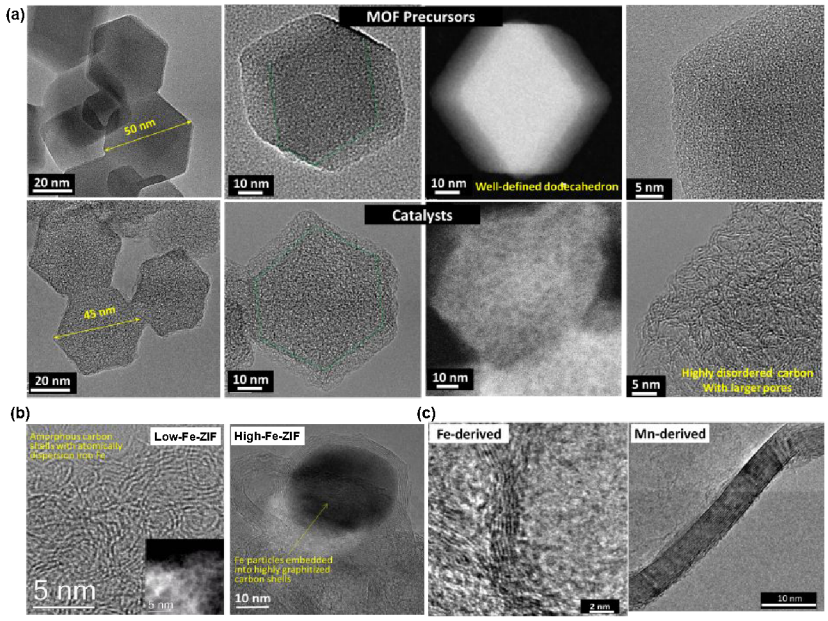

Fig. 26. Carbon nanostructures and morphologies in atomically dispersed Fe-N-C catalysts derived from ZIF-8 precursors. (a) The carbonization of Fe-doped ZIF-8 nanocrystals to generate highly amorphous and defect-rich carbon particles in catalysts. Reproduced with permission.[85] Copyright 2017, American Chemical Society. (b) The effect of Fe doping content on carbon structures of the Fe-doped ZIF-derived catalysts. (c) The effect of metals (Fe *vs*. Mn) on the carbon structures derived from carbon/nitrogen precursors (i.e., dicyandiamide) through carbonization. Reproduced with permission.[277] Copyright 2019, Royal Society of Chemistry.

To enhance carbon corrosion resistance and extend the lifetime of M-N-C catalysts-based MEAs, early works focused on using carbon supports with a higher degree of graphitization than conventional carbon black. For instance, the multi-walled carbon nanotube (MWCNTs)-supported Fe-N-C catalyst, featured with a much higher degree of carbon graphitization, showed negligible performance degradation for more than 500 h at a cell voltage of 0.4 V. Inspired by this, many studies have embarked on achieving enhanced stability by increasing the degree of graphitization and optimizing the local carbon bond structure.[274-278] Early M-N-C catalysts contain highly graphitized carbon due to a large number of metals (*e.g.*, Fe or/and Co) used for catalyzing the graphitization of nitrogen/carbon precursors during the synthesis. However, the latest atomically dispersed M-N-C catalysts are often dominant with ZIF-8-derived amorphous carbon due to the use of limited metal doping (**Fig. 26a**). Increasing Fe doping content leads to the graphitized carbon and the formation of metallic aggregates enclosed into carbon shells often observed in previous M-N-C catalysts (**Fig. 26b**). The amorphous carbon essentially helps provide defects and heteroatom dopants to accommodate high-density single metal sites, but with less corrosion resistance. Thus, the carbon corrosion-related stability issue becomes more severe for those atomically dispersed metal site catalysts with exceptionally high ORR activity. The research goals are to address the trade-off between initial activity and stability, achieving considerably enhanced durability, but with an insignificant compromise of the activity.

Recently, we found that, compared to traditional Fe, Mn atoms can catalyze the carbon with a higher degree of graphitization (**Fig. 26c**). This result may also provide an opportunity to tune carbon structures with enhanced corrosion resistance by using alternative but still active metals. Preliminary DFT calculations predict the MnN_4 moiety embedded in the carbon has comparable activity to the FeN_4 sites. Thus, the development of Mn-based catalysts may promote the

graphitization degree of the local carbon structures adjacent to MN_4 active sites, which would be favorable for stability enhancement. A recent study of atomically dispersed Mn-N-C catalysts has attracted much attention because of its superior stability than Fe-N-C catalysts.[18] When compared to traditional Fe-N-C catalysts derived from PANI (loss 80 mV after 5,000 cycles) and ZIF-derived Fe-N-C catalyst (29 mV loss), the stability of Mn-N-C catalyst (17 mV) is much improved. The double-layer capacitance of the Mn-N-C catalyst increased by around 30 %, which was less than that of the Fe-N-C catalyst (60%). It suggested that the enhanced stability of the Mn-N-C catalyst may be due to the improved corrosion resistance of the highly graphitized carbon structure in the catalysts.

Another effective strategy is to in-situ generate highly graphitized carbon into M-N-C catalysts. A Fe-N/CNT catalyst, which consists of directly grown CNTs doped with high-density of FeN_x sites, demonstrated a significant enhancement of stability.[276] Compared to the loss of the Fe-N-C catalyst (38 mV after 500 cycles 0.9-1.4 V), the Fe-N/CNT catalyst exhibited only 20 mV loss in $E_{1/2}$, thus proving the significant role of highly graphitized carbon structures in improving M-N-C stability. The high stability of the Fe-N/CNT catalyst is due to its higher graphitization degree and higher corrosion resistance. However, highly graphitized carbons tend to be less prone to hosting $M\text{-}N_4$ sites, which has stimulated the rational design of M-N-C catalysts with a unique activity and stability trade-off.[279]

4.4 Mitigating water flooding

Because micropores host most of the MN_x active sites in catalysts, the adverse effect of micropore flooding likely cause MEA performance loss. Dodelet et al., firstly, proposed micropore flooding is the primary degradation mechanism for the first rapid decay of the original performance for ZIF-8 supported Fe-N-C catalysts.[69] Because the original hydrophobic catalyst layer would gradually

transform into a hydrophilic catalyst layer due to the electrochemical oxidation of carbon support enriched with oxygen-containing functional groups. The hydrophilic catalyst layers are subject to micropore flooding, causing a rapid performance decay of Fe-N-C catalysts.[46, 203] This rapid micropore flooding may be due to the treatment with NH_3. The process proved useful for creating micropores and introducing hydrophilicity at the surfaces of catalysts. Therefore, there is a high possibility that micropore flooding induced significant initial performance degradation, rather than the gradual surface oxidation.

Oppositely, Banham et al., at Ballard, reported two Fe-N-C catalysts and ruled out the micropore flooding degradation mechanism.[222] In the first one, they devised a systematic experiment for investigating the contribution of micropore flooding degree to the instability of Fe-N-C-PANI-Phen catalysts-based MEA.[222] They outlined a series of MEA tests for monitoring the changes of double-layer capacitance in CV curves and O_2/air polarization curves at various conditions. Moreover, finally, they concluded that most of the micropores are wetted quickly at BOL, and additional occurrence of catalyst layer slightly wetting during the stability test does not make significant performance loss. The performance decay is manifested in the kinetic region, but micropore flooding-induced the mass transport loss is negligible. Thus, they suggested that micropore flooding may not be the main factor causing performance degradation. The second case is even more informative in the design of the catalysts and catalyst layers.[5] A Fe-doped ZIF-8 derived Fe-N-C catalysts possessed nearly 100 % of micropores with size below 3 nm, which blocked the ionomers outside of these micropores. Surprisingly, contrary to our common sense that a hierarchical porosity favors a superior mass transport, this microporous catalyst achieved a record-breaking power density of 570 mW cm^{-2} with the H_2/air cell with the 4.0 mg cm^{-2} catalysts loading (50 cm^2 MEA tested at 75^{o}C,100 %RH, I/C:0.67, Nafion 211, air pressure:173 Kpa).

Moreover, this MEA only suffered from a 10% initial performance decay after 60 hours galvanostatic stability test at 0.5 A cm^{-2} (shown in **Fig. 22j**). If the micropore flooding is the primary mechanism, the degradation may polarize with the thickness of the catalyst layer because the volume of the micropore increases with an increase in catalyst loadings. However, the results of the three catalyst layers with different loadings are contradictory to the hypothesis, which directly exclude the micropore flooding degradation mechanism. Therefore, the micropore flooding mechanism is still under debate. Micropore flooding indeed exists, and the degree of the flooding may highly dependent on the physicochemical properties of M-N-C catalysts. Recently, the original micropore flooding was further revised.[70] The initial loss of activity is due to the specific demetallation of the Fe-N_4 site in the micropores caused by the water flux (H^+ and O_2) through the open micropores. Despite the insignificant effect on the initial performance decay, water flooding in micropores or catalysts layers leads to additional resistance of mass and charge transports within the thick cathode during the long-term operation of the fuel cells.[175, 280]

In summary, despite significant progress in terms of activity, their insufficient stability and durability of M-N-C catalysts in MEAs prohibit their practical applications. Performance degradation may be due to multiple reasons, including the destruction of MN_4 sites *via* the Fenton reaction/H_2O_2, demetallation, carbon oxidation, and water flooding. It is worth noting that these different degradation mechanisms are not independent. Deionized metal ions (especially Fe^{2+}/Fe^{3+}) can catalyze the formation of free radicals from H_2O_2 through the Fenton reaction, which in turn act as potential carbon oxidants. On the other hand, chemical and/or electrochemical oxidation of carbon can accelerate demetallation by destroying the local carbon structure or by directly affecting the MN_4 sites within the triple-phase boundary. Carbon corrosion also accelerates the

micropore flooding because the oxidation at carbon surfaces can generate oxygen functional groups, further increasing catalyst hydrophilicity.

Accordingly, minimizing the production of H_2O_2 intermediate and the oxidation of carbon can improve the durability. More efforts are to (1) increase the mass activity by increasing the TOF of the active sites or increasing the density of active sites; (2) adjust the d-electron density and the geometry of the metal center to suppress the generation of H_2O_2; (3) alleviate the mass transfer issues of the PGM-free MEAs due to the thick catalyst layer, *e.g.*, establishing an active three-phase boundary; and (4) improve durability from the perspective of catalyst and cathode engineering, *e.g.*, catalyst loading and I/C ratio in addition to the catalyst itself. Morphology characterization is useful for elucidating the primary macroscale degradation mechanisms by comparing the catalyst layer at the BOL and end-of-life (EOL) studies. The studied ex-situ techniques include electron microscopy/tomography, X-ray computed tomography, F-mapping, and stained ionomer using nano-CT. Using *in-situ* water imaging in the catalyst layer via neutron radiography can elucidate the changes in carbon wettability during aging. Additionally, modeling possible degradation mechanisms can provide reasonable guidance toward experimental works, further generating a comprehensive understanding of the correlation between catalyst intrinsic property with activity and durability.

5. Perspectives and outlook

The development of high-performance PGM-free catalysts is scientifically and technologically essential to accelerate the large-scale applications of sustainable renewable energy via electrochemical reactions. As discussed in this review, the atomically dispersed M-N-C catalyst provides an excellent opportunity to substitute the use of PGMs at the cathode for PEMFCs. Innovative and effective synthesis strategies are essential to improve the catalytic activity of M-

N-C catalysts with regards to improving intrinsic activity, increasing site density, and stabilizing the M-N bonds, and their interactions with carbon supports. Generally, two common strategies improve the performance of M-N-C catalysts: (i) enhancement of the intrinsic activity of atomic metal active sites through regulating the local coordination structure of the center metal, introducing light heteroatoms, dual-atom or multi-atom metals, and creating more edge hosted M-N_x sites; (ii) the increase of atomic metal sites density by enhancing the metal-support interactions, introducing more defects or dopants to stabilize single metal sites, using spatial confinement strategies. Furthermore, with the assistance of theoretical calculation and *in-situ* characterization technologies, elucidating the structure-performance correlation at the atomic scale is the key to shedding light on the rational design of M-N-C catalysts with optimal activity, selectivity, and stability. For the more demanding PEMFC applications, insightful understanding and new approaches for implementing the most promising catalysts into MEA cathodes are crucial for achieving adequate MEA performance. Therefore, the hierarchical pore structure of catalysts is essential. Micropores can host a high density of single metal active sites. Mesopores and macropores can facilitate ionomer distribution and promote the transport of reactants and products. The thick M-N-C cathode often suffers from severe transport losses at higher current densities and therefore limits its power density. Optimization of the catalyst layer structure's properties (*i.e.*, particle and agglomerate size, pore size distribution, hydrophobicity, ionomer-to-carbon ratio, and ionomer distribution) can significantly mitigate the mass transfer limitation, which is essential for translating ORR activity in the MEA performance.

In addition to insufficient activity, stability and durability are more severe limitations for current M-N-C catalysts under realistic operation conditions. It remains elusive that highly active catalysts often deactivate rapidly. There must be multiple types of MN_x catalysts in catalysts,

which contain different coordination numbers and local structures. The rapid activity loss at the initial stage is not evident yet. It is likely due to the oxidation of the carbon matrix and the destruction of the MN_4 active sites, but maybe not related to H_2O_2 and ROS attacking. Poisoning and weak adsorption of functional groups on active sites are probably responsible for the partially reversible activity (RDE) and MEA performance. We also speculate that FeN_4 and CoN_4 site catalysts behave differently during degradation. Because continuous activity loss often was observed with Fe-N-C catalysts, while Co-N-C catalysts tend to steady after the initial loss. Our preliminary DFT calculations predicted that Co-N bonds might be stronger than Fe-N. The Fe^{3+}/Fe^{2+} redox (0.77 V) during the ORR would weaken the Fe-N bond. However, the relevant Co^{3+}/Co^{2+} redox (1.81 V) is beyond ORR potentials and does not happen for Co-N-C catalysts. Mn-N-C catalysts are complicated due to the multiple valances, including Mn^{3+}/Mn^{2+} (1.51 V) and MnO_2/Mn^{2+} (1.23 V). enhanced corrosion tolerance of carbon is beneficial for stability improvements but yields fewer defects and dopants that are crucial for hosting single metal active sites. Innovative concepts are highly desirable for addressing the trade-off issue.

Possible ionomer phase changes and water flooding in cathodes also cause additional resistances of mass transport and proton/electron transfer. Thus, to improve intrinsic stability of M-N-C catalysts and performance durability of electrodes effectively, significant efforts should focus on (i) exploring the possible synergy between Fe, Co, or/and Mn sites to modify electronic and geometric structures of active sites; (ii) increasing the volumetric site density to reduce the thickness of catalyst layers in MEAs; (iii) engineering local coordination structures to strengthen M-N bond; (iv) tuning the electronic structure of Fe centers or seeking alternative metals with mitigated Fenton reactions such as Co and Mn to reduce or eliminate the generation of the H_2O_2 intermediates; (v) exploiting more robust carbon supports with increased graphitization degree to

alleviate the carbon oxidation issue; (vi) constructing an active three-phase boundary in MEAs to mitigate the mass transfer and water flooding issues caused by the thick catalyst layer; (vii) optimizing the cathode structure via innovative electrode design and fabrication, such as a thinner catalyst layer with structural and hydrophobic modification to facilitate water removal; (viii) developing high-throughput combinatorial methods and models for studying catalyst stability by using operando MEA characterization and diagnosis.

Overall, the development of atomically dispersed M-N-C catalysts to replace PGM catalysts is high reward research for fuel cell technologies. In the past ten years, significantly improved catalytic activity in liquid acids based on RDE measurements is comparable to the state-of-the-art Pt/C catalysts.[8] We hold optimistic opinions and expect to address the severe stability issues and dramatically enhance MEA performance in the next ten years. In addition to hydrogen fuel cells, M-N-C cathode catalysts have apparent advantages in direct methanol or ammonia fuel cells due to their excellent tolerances compared to PGM counterparts.[25,237,282,283] Beside the ORR, they have exhibited promising activity for CO_2 reduction reactions (CO_2RR),[10,125,281,284] and nitrogen reduction reactions (NRR) for ammonia electrosynthesis.[119,180,285,286] Generally, the atomically dispersed PGM-free M-N-C catalyst universally represents a new class of catalysts for electrochemical energy conversion and storage.

Acknowledgments

The authors acknowledge the financial support from the U.S. Department of Energy, Office of Energy Efficiency and Renewable Energy (EERE), Fuel Cell Technology Office (DE-EE0008075, DE-EE0008076, and DE-EE0008417) along with National Science Foundation (CBET-1604392, 1804326).

References

1. I. Staffell, D. Scamman, A. V. Abad, P. Balcombe, P. E. Dodds, P. Ekins, N. Shah and K. R. Ward, *Energy Environ. Sci.*, 2019, **12**, 463-491.

2. M. Lefevre, E. Proietti, F. Jaouen and J. P. Dodelet, *Science*, 2009, **324**, 71-74.

3. M. K. Debe, *Nature*, 2012, **486**, 43-51.

4. Y. Deng, B. Chi, J. Li, G. Wang, L. Zheng, X. Shi, Z. Cui, L. Du, S. Liao and K. Zang, *Adv. Energy Mater.*, 2019, **9**, 1802856.

5. D. Banham, T. Kishimoto, Y. Zhou, T. Sato, K. Bai, J.-i. Ozaki, Y. Imashiro and S. Ye, *Sci. Adv.*, 2018, **4**, eaar7180.

6. J. Hou, M. Yang, C. Ke, G. Wei, C. Priest, Z. Qiao, G. Wu and J. Zhang, *EnergyChem*, 2020, **2**, 100023.

7. X. Ren, Q. Lv, L. Liu, B. Liu, Y. Wang, A. Liu and G. Wu, *Sustainable Energy Fuels*, 2020, DOI: 10.1039/C9SE00460B, 10.1039/C1039SE00460B.

8. X. X. Wang, M. T. Swihart and G. Wu, *Nat. Catal.*, 2019, **2**, 578-589.

9. Z. Qiao, S. Hwang, X. Li, C. Wang, W. Samarakoon, S. Karakalos, D. Li, M. Chen, Y. He, M. Wang, Z. Liu, G. Wang, H. Zhou, Z. Feng, D. Su, J. S. Spendelow and G. Wu, *Energy Environ. Sci.*, 2019, **12**, 2830-2841.

10. X. X. Wang, S. Hwang, Y.-T. Pan, K. Chen, Y. He, S. Karakalos, H. Zhang, J. S. Spendelow, D. Su and G. Wu, *Nano Lett.*, 2018, **18**, 4163-4171.

11. Q. R. Shi, C. Z. Zhu, S. F. Fu, D. Du, Y. H. Lin, *ACS Appl. Mater. Interfaces*, 2016, **8**, 4739-4744.

12. C. Z. Zhu, Q. R. Shi, S. F. Fu, J. H. Song, H. B. Xia, D. Du Y. H. Lin, *Adv. Mater.*, 2016, **28**, 8779-8783.

13. S. T. Thompson, A. R. Wilson, P. Zelenay, D. J. Myers, K. L. More, K. C. Neyerlin and D. Papageorgopoulos, *Solid State Ion.*, 2018, **319**, 68-76.

14. S. T. Thompson and D. Papageorgopoulos, *Nat. Catal.*, 2019, **2**, 558-561.

15. Y. Shao, J. P. Dodelet, G. Wu and P. Zelenay, *Adv. Mater.*, 2019, **31**, e1807615.

16. Y. He, Q. Tan, L. Lu, J. Sokolowski and G. Wu, *Electrochem. Energy Rev.*, 2019, **2**, 231-251.

17. U. Martinez, S. K. Babu, E. F. Holby and P. Zelenay, *Curr. Opin. Electrochem.,* 2018, **9**, 224-232.

18. J. Z. Li, M. J. Chen, D. A. Cullen, S. Hwang, M. Y. Wang, B. Y. Li, K. X. Liu, S. Karakalos, M. Lucero, H. G. Zhang, C. Lei, H. Xu, G. E. Sterbinsky, Z. X. Feng, D. Su, K. L. More, G. F. Wang, Z. B. Wang and G. Wu, *Nat. Catal.*, 2018, **1**, 935-945.

19. U. Martinez, S. Komini Babu, E. F. Holby, H. T. Chung, X. Yin and P. Zelenay, *Adv. Mater.*, 2019, **31**, e1806545.

20. U. I. Kramm, M. Lefevre, N. Larouche, D. Schmeisser and J. P. Dodelet, *J. Am. Chem. Soc.*, 2014, **136**, 978-985.

21. G. Wu, *Front. Energy*, 2017, **11**, 286-298.

22. H. Zhang, H. Osgood, X. Xie, Y. Shao and G. Wu, *Nano Energy*, 2017, **31**, 331-350.

23. D. Banham and S. Y. Ye, *ACS Energy Lett.*, 2017, **2**, 629-638.

24. H. T. Chung, D. A. Cullen, D. Higgins, B. T. Sneed, E. F. Holby, K. L. More and P. Zelenay, *Science*, 2017, **357**, 479-484.

25. Q. Li, T. Wang, D. Havas, H. Zhang, P. Xu, J. Han, J. Cho and G. Wu, *Adv. Sci.*, 2016, **3**, 1600140.

26. X. Xu, Z. Xia, X. Zhang, R. Sun, X. Sun, H. Li, C. Wu, J. Wang, S. Wang and G. Sun, *Appl. Catal. B: Environ*, 2019, **259**, 118042.

27. R. Jasinski, *Nature*, 1964, **201**, 1212-1213.

28. H. Jahnke, M. Schönborn and G. Zimmermann, *Top. Curr. Chem.*, 1976, **61**, 133-181.

29. C. W. B. Bezerra, L. Zhang, H. S. Liu, K. C. Lee, A. L. B. Marques, E. P. Marques, H. J. Wang and J. J. Zhang, *J. Power Sources*, 2007, **173**, 891-908.

30. Z. H. Zhai, Y. Lv, C. X. Qiu, R. N. Zheng, J. Li, A. J. Wang and Y. J. Song, *J. Electrochem. Soc.*, 2019, **166**, F441-F447.

31. K. Kadish, K. M. Smith and R. Guilard, *The porphyrin handbook*, Elsevier, 2000.

32. J. A. R. Van Veen, J. F. van Baar and K. J. Kroese, *J. Chem. Soc., Faraday Trans. 1*, 1981, **77**, 2827-2843.

33. E. Yeager, *J. Mol. Catal.*, 1986, **38**, 5-25.

34. T. Sun, B. Tian, J. Lu and C. Su, *J. Mater. Chem. A*, 2017, **5**, 18933-18950.

35. Z. Qiao, H. G. Zhang, S. Karakalos, S. Hwang, J. Xue, M. J. Chen, D. Su and G. Wu, *Appl. Catal. B: Environ.*, 2017, **219**, 629-639.

36. C. W. Bezerra, L. Zhang, K. Lee, H. Liu, A. L. Marques, E. P. Marques, H. Wang and J. Zhang, *Electrochim. Acta*, 2008, **53**, 4937-4951.

37. J. Liu, X. Sun, P. Song, Y. Zhang, W. Xing and W. Xu, *Adv. Mater.*, 2013, **25**, 6879-6883.

38. A. Friedman, L. Landau, S. Gonen, Z. Gross and L. Elbaz, *ACS Catal.*, 2018, **8**, 5024-5031.

39. Q. Cheng, L. Yang, L. Zou, Z. Zou, C. Chen, Z. Hu and H. Yang, *ACS Catal.*, 2017, **7**, 6864-6871.

40. H. M. Barkholtz and D.-J. Liu, *Mater. Horiz.*, 2017, **4**, 20-37.

41. H. Zhang, J. Li, Q. Tan, L. Lu, Z. Wang and G. Wu, *Chem-Eur. J.*, 2018, **24**, 18137-18157.

42. X. Wang, H. Zhang, H. Lin, S. Gupta, C. Wang, Z. Tao, H. Fu, T. Wang, J. Zheng, G. Wu and X. Li, *Nano Energy*, 2016, **25**, 110-119.

43. F. T. Wagner, H. A. Gasteiger and S. S. Yan, *GM Fuel Cell Actvities*, *DOE Workshop*, 2003.

44. H. A. Gasteiger and N. M. Marković, *Science*, 2009, **324**, 48-49.

45. A. Kongkanand and M. F. Mathias, *J. Phys. Chem. Lett.*, 2016, **7**, 1127-1137.

46. Y.-C. Hao, Y. Guo, L.-W. Chen, M. Shu, X.-Y. Wang, T.-A. Bu, W.-Y. Gao, N. Zhang, X. Su, X. Feng, J.-W. Zhou, B. Wang, C.-W. Hu, A.-X. Yin, R. Si, Y.-W. Zhang and C.-H. Yan, *Nat. Catal.*, 2019, **2**, 448-456.

47. H. Chen, S. J. You, Y. Y. Ma, C. Y. Zhang, B. J. Jing, Z. Cai, B. Tang, N. Q. Ren and J. L. Zou, *Chem. Mater.*, 2018, **30**, 6014-6025.

48. C. Zhu, S. Fu, Q. Shi, D. Du and Y. Lin, *Angew. Chem. Int. Ed.*, 2017, **56**, 13944-13960.

49. N. Zion, D. A. Cullen, P. Zelenay and L. Elbaz, *Angew. Chem. Int. Ed.*, 2019, **59**, 2483-2489.

50. S. Gupta, S. Zhao, O. Ogoke, Y. Lin, H. Xu and G. Wu, *ChemSusChem*, 2017, **10**, 774-785.

51. L. Tong, Y.-C. Wang, M.-X. Chen, Z.-Q. Chen, Q.-Q. Yan, C.-L. Yang, Z.-Y. Zhou, S.-Q. Chu, X. Feng and H.-W. Liang, *Chem. Sci.*, 2019, **10**, 8236-8240.

52. H. Zhang, S. Ding, S. Hwang, X. Zhao, D. Su, H. Xu, H. Yang and G. Wu, *J. Electrochem. Soc.*, 2019, **166**, F3116-F3122.

53. Q. Shi, S. Hwang, H. Yang, F. Ismail, D. Su, D. Higgins and G. Wu, *Mater. Today*, 2020, DOI: 10.1016/j.mattod.2020.02.019.

54. M. E. Scofield, H. Q. Liu and S. S. Wong, *Chem. Soc. Rev.*, 2015, **44**, 5836-5860.

55. F. Jaouen, E. Proietti, M. Lefevre, R. Chenitz, J. P. Dodelet, G. Wu, H. T. Chung, C. M. Johnston and P. Zelenay, *Energy Environ. Sci.*, 2011, **4**, 114-130.

56. Q. Jia, E. Liu, L. Jiao, S. Pann and S. Mukerjee, *Adv. Mater.*, 2019, **31**, e1805157.

57. M. L. Xiao, J. B. Zhu, L. Ma, Z. Jin, J. Ge, X. J. Deng, Y. Hou, Q. G. He, J. K. Li, Q. Y. Jia, S. Mukerjee, R. Yang, Z. Jiang, D. S. Su, C. P. Liu and W. Xing, *ACS Catal.*, 2018, **8**, 2824-2832.

58. X. M. Ge, A. Sumboja, D. Wuu, T. An, B. Li, F. W. T. Goh, T. S. A. Hor, Y. Zong and Z. L. Liu, *ACS Catal.*, 2015, **5**, 4643-4667.

59. C. H. Choi, C. Baldizzone, J. P. Grote, A. K. Schuppert, F. Jaouen and K. J. J. Mayrhofer, *Angew. Chem. Int. Ed.*, 2015, **54**, 12753-12757.

60. X. Fu, P. Zamani, J. Y. Choi, F. M. Hassan, G. Jiang, D. C. Higgins, Y. Zhang, M. A. Hoque and Z. Chen, *Adv. Mater.*, 2017, **29**, 1604456.

61. G. Inoue and M. Kawase, *J. Power Sources*, 2016, **327**, 1-10.

62. S. Lee, D.-H. Kwak, S.-B. Han, Y.-W. Lee, J.-Y. Lee, I.-A. Choi, H.-S. Park, J.-Y. Park and K.-W. Park, *ACS Catal.*, 2016, **6**, 5095-5102.

63. H. W. Liang, W. Wei, Z. S. Wu, X. Feng and K. Mullen, *J. Am. Chem. Soc.*, 2013, **135**, 16002-16005.

64. S. W. Liu, H. M. Zhang, Q. Zhao, X. Zhang, R. R. Liu, X. Ge, G. Z. Wang, H. J. Zhao and W. P. Cai, *Carbon*, 2016, **106**, 74-83.

65. J. Tang, J. Liu, C. Li, Y. Li, M. O. Tade, S. Dai and Y. Yamauchi, *Angew. Chem. Int. Ed.*, 2015, **54**, 588-593.

66. H. Singh, S. Q. Zhuang, B. Ingis, B. B. Nunna and E. S. Lee, *Carbon*, 2019, **151**, 160-174.

67. R. Sharma and S. M. Andersen, *ACS Catal.*, 2018, **8**, 3424-3434.

68. D. Banham, S. Ye, K. Pei, J. Ozaki, T. Kishimoto and Y. Imashiro, *J. Power Sources*, 2015, **285**, 334-348.

69. G. Zhang, R. Chenitz, M. Lefèvre, S. Sun and J.-P. Dodelet, *Nano Energy*, 2016, **29**, 111-125.

70. R. Chenitz, U. I. Kramm, M. Lefevre, V. Glibin, G. X. Zhang, S. H. Sun and J. P. Dodelet, *Energy Environ. Sci.*, 2018, **11**, 365-382.

71. D. Eisenberg, T. K. Slot and G. Rothenberg, *ACS Catal.*, 2018, **8**, 8618-8629.

72. R. F. Zhou, Y. Zheng, M. Jaroniec and S. Z. Qiao, *ACS Catal.*, 2016, **6**, 4720-4728.

73. S. Kattel and G. Wang, *J. Mater. Chem. A*, 2013, **1**, 10790–10797.

74. Y. Jiao, Y. Zheng, M. Jaroniec and S. Z. Qiao, *J. Am. Chem. Soc.*, 2014, **136**, 4394-4403.

75. E. F. Holby and P. Zelenay, *Nano Energy*, 2016, **29**, 54-64.

76. K. X. Liu, G. Wu and G. F. Wang, *J. Phys. Chem. C*, 2017, **121**, 11319-11324.

77. M. Busch, N. B. Halck, U. I. Kramm, S. Siahrostami, P. Krtil and J. Rossmeisl, *Nano Energy*, 2016, **29**, 126-135.

78. Y. H. Han, Y. G. Wang, R. R. Xu, W. X. Chen, L. R. Zheng, A. J. Han, Y. Q. Zhu, J. Zhang, H. B. Zhang, J. Luo, C. Chen, Q. Peng, D. S. Wang and Y. D. Li, *Energy Environ. Sci.*, 2018, **11**, 2348-2352.

79. Y. Mun, S. Lee, K. Kim, S. Kim, S. Lee, J. W. Han and J. Lee, *J. Am. Chem. Soc.*, 2019, **141**, 6254-6262.

80. S. S. A. Shah, T. Najam, C. Cheng, L. Peng, R. Xiang, L. Zhang, J. Deng, W. Ding and Z. Wei, *Chem-Eur. J.*, 2018, **24**, 10630-10635.

81. H. Shen, E. Gracia-Espino, J. Ma, K. Zang, J. Luo, L. Wang, S. Gao, X. Mamat, G. Hu, T. Wagberg and S. Guo, *Angew. Chem. Int. Ed.*, 2017, **56**, 13800-13804.

82. Y. C. Wang, Y. J. Lai, L. Song, Z. Y. Zhou, J. G. Liu, Q. Wang, X. D. Yang, C. Chen, W. Shi and Y. P. Zheng, *Angew. Chem. Int. Ed.*, 2015, **54**, 9907-9910.

83. N. Ramaswamy, U. Tylus, Q. Jia and S. Mukerjee, *J. Am. Chem. Soc.*, 2013, **135**, 15443-15449.

84. W. Liang, J. X. Chen, Y. W. Liu and S. L. Chen, *ACS Catal.*, 2014, **4**, 4170-4177.

85. H. Zhang, S. Hwang, M. Wang, Z. Feng, S. Karakalos, L. Luo, Z. Qiao, X. Xie, C. Wang, D. Su, Y. Shao and G. Wu, *J. Am. Chem. Soc.*, 2017, **139**, 14143-14149.

86. A. Zitolo, V. Goellner, V. Armel, M. T. Sougrati, T. Mineva, L. Stievano, E. Fonda and F. Jaouen, *Nat. Mater.*, 2015, **14**, 937-942.

87. Q. Jia, N. Ramaswamy, H. Hafiz, U. Tylus, K. Strickland, G. Wu, B. Barbiellini, A. Bansil, E. F. Holby, P. Zelenay and S. Mukerjee, *ACS Nano*, 2015, **9**, 12496-12505.

88. Y. X. Peng, Z. P. Li, D. G. Xia, L. R. Zheng, Y. Liao, K. Li and X. Zuo, *J. Power Sources*, 2015, **291**, 20-28.

89. U. I. Kramm, I. Herrmann-Geppert, J. Behrends, K. Lips, S. Fiechter and P. Bogdanoff, *J. Am. Chem. Soc.*, 2016, **138**, 635-640.

90. A. S. Varela, N. Ranjbar Sahraie, J. Steinberg, W. Ju, H.-S. Oh and P. Strasser, *Angew. Chem. Int. Ed.*, 2015, **127**, 10908-10912.

91. J. Li, H. Zhang, W. Samarakoon, W. Shan, D. A. Cullen, S. Karakalos, M. Chen, D. Gu, K. L. More, G. Wang, Z. Feng, Z. Wang and G. Wu, *Angew. Chem. Int. Ed.*, 2019, **58,** 18971-18980.

92. J. P. McClure, O. Borodin, M. Olguin, D. Chu and P. S. Fedkiw, *J.Phys. Chem. C*, 2016, **120**, 28545-28562.

93. D. Malko, A. Kucernak and T. Lopes, *Nat. Commun.*, 2016, **7**, 13285.

94. N. R. Sahraie, U. I. Kramm, J. Steinberg, Y. Zhang, A. Thomas, T. Reier, J. P. Paraknowitsch and P. Strasser, *Nat. Commun.*, 2015, **6**, 8618.

95. R. Z. Snitkoff, N. Levy, I. Ozery, S. Ruthstein, L. Elbaz, *Carbon*, 2019, **143**, 223-229.

96. J. H. K. Zagal, M. T. M. Kopper, *Angew. Chem. Int. Ed.* , 2016, **55**, 14510-14521.

97. R. R. Venegas, F. J.; Riquelme, J.; Neira, K.; Marco, J. F.; Ponce, I.; Zagal, J. H.; Tasca, F., *J. Mater. Chem. A*, 2017, **24**, 12054-12059.

98. G. Wu and P. Zelenay, *Acc. Chem. Res.*, 2013, **46**, 1878-1889.

99. G. Wu, N. H. Mack, W. Gao, S. Ma, R. Zhong, J. Han, J. K. Baldwin and P. Zelenay, *ACS Nano*, 2012, **6**, 9764-9776.

100. G. Wu, C. M. Johnston, N. H. Mack, K. Artyushkova, M. Ferrandon, M. Nelson, J. S. Lezama-Pacheco, S. D. Conradson, K. L. More, D. J. Myers and P. Zelenay, *J. Mater. Chem.*, 2011, **21**, 11392-11405.

101. H. Zhang, H. T. Chung, D. A. Cullen, S. Wagner, U. I. Kramm, K. L. More, P. Zelenay and G. Wu, *Energy Environ. Sci.*, 2019, **12**, 2548-2558.

102. E. Proietti, F. Jaouen, M. Lefevre, N. Larouche, J. Tian, J. Herranz and J. P. Dodelet, *Nat. Commun.*, 2011, **2**, 416.

103. J. K. Li, S. Ghoshal, W. T. Liang, M. T. Sougrati, F. Jaouen, B. Halevi, S. McKinney, G. McCool, C. R. Ma, X. X. Yuan, Z. F. Ma, S. Mukerjee and Q. Y. Jia, *Energy Environ. Sci.*, 2016, **9**, 2418-2432.

104. X. X. Wang, D. A. Cullen, Y. T. Pan, S. Hwang, M. Wang, Z. Feng, J. Wang, M. H. Engelhard, H. Zhang, Y. He, Y. Shao, D. Su, K. L. More, J. S. Spendelow and G. Wu, *Adv. Mater.*, 2018, **30**, 1706758.

105. Y. He, S. Hwang, D. A. Cullen, M. A. Uddin, L. Langhorst, B. Li, S. Karakalos, A. J. Kropf, E. C. Wegener, J. Sokolowski, M. Chen, D. Myers, D. Su, K. L. More, G. Wang, S. Litster and G. Wu, *Energy Environ. Sci.*, 2019, **12**, 250-260.

106. M. Liu, L. Wang, K. Zhao, S. Shi, Q. Shao, L. Zhang, X. Sun, Y. Zhao and J. Zhang, *Energy Environ. Sci.*, 2019, **12**, 2890-2923.

107. T. Sharifi, E. Gracia-Espino, A. Chen, G. Hu and T. Wågberg, *Adv. Energy Mater.*, 2019, **10**, 1902084.

108. U. I. Kramm, J. Herranz, N. Larouche, T. M. Arruda, M. Lefevre, F. Jaouen, P. Bogdanoff, S. Fiechter, I. Abs-Wurmbach, S. Mukerjee and J. P. Dodelet, *Phys. Chem. Chem. Phys.*, 2012, **14**, 11673-11688.

109. N. Ramaswamy, U. Tylus, Q. Jia and S. Mukerjee, *J. Amer. Chem. Soc.*, 2013, **135**, 15443-15449.

110. K. Mamtani, D. Singh, D. Dogu, D. Jain, J. M. M. Millet and U. S. Ozkan, *Energy Fuel*, 2018, **32**, 11038-11045.

111. K. X. Liu, S. Kattel, V. Mao and G. F. Wang, *J. Phys. Chem. C*, 2016, **120**, 1586-1596.

112. C. Zhu, Q. Shi, B. Z. Xu, S. Fu, G. Wan, C. Yang, S. Yao, J. Song, H. Zhou and D. Du, *Adv. Energy Mater.*, 2018, **8**, 1801956.

113. M. Rauf, Y. D. Zhao, Y. C. Wang, Y. P. Zheng, C. Chen, X. D. Yang, Z. Y. Zhou and S. G. Sun, *Electrochem. Commun.*, 2016, **73**, 71-74.

114. Q. Lai, L. Zheng, Y. Liang, J. He, J. Zhao and J. Chen, *ACS Catal.*, 2017, **7**, 1655-1663.

115. V. P. Glibin and J. P. Dodelet, *J. Electrochem. Soc.*, 2017, **164**, P948-P957.

116. X. X. Wang, V. Prabhakaran, Y. H. He, Y. Y. Shao and G. Wu, *Adv. Mater.*, 2019, **31**, 1805126.

117. X. Sun, K. Li, C. Yin, Y. Wang, F. He, H. Tang and Z. Wu, *Phys. Chem. Chem. Phys.*, 2017, **19**, 17670-17676.

118. J. Huang, Q. Lu, X. Ma and X. Yang, *J. Mater. Chem. A*, 2018, **6**, 18488-18497.

119. X. Liu, Y. Jiao, Y. Zheng, M. Jaroniec and S.-Z. Qiao, *J. Am. Chem. Soc.*, 2019, **141**, 9664-9672.

120. X. Yang, Y. Wang, G. Zhang, L. Du, L. Yang, M. Markiewicz, J.-Y. Choi, C. Régis and S. Sun, *Appl. Catal. B: Environ.*, 2019, **264**, 118523.

121. F. Jaouen, F. Charreteur and J. P. Dodelet, *J. Electrochem. Soc.*, 2006, **153**, A689-A698.

122. L. Osmieri, A. H. A. Monteverde Videla, P. Ocón and S. Specchia, *J. Phys. Chem.*, 2017, **121**, 17796-17817.

123. Y. Mun, S. Lee, K. Kim, S. Kim, S. Lee, J. W. Han and J. Lee, *J. Am. Chem. Soc.*, 2019, **141**, 6254-6262.

124. H. Shen, E. Gracia-Espino, J. Ma, K. Zang, J. Luo, L. Wang, S. Gao, X. Mamat, G. Hu and T. Wagberg, *Angew. Chem. Int. Ed.*, 2017, **56**, 13800-13804.

125. F. Pan, B. Li, E. Sarnello, S. Hwang, Y. Gang, X. Feng, X. Xiang, N. M. Adli, T. Li, D. Su, G. Wu, G. Wang and Y. Li, *Nano Energy*, 2020, **68**, 104384.

126. Y. Wang, C. Zhu, S. Feng, Q. Shi, S. Fu, D. Du, Q. Zhang and Y. Lin, *ACS Appl. Mater. Inter.*, 2017, **9**, 40298-40306.

127. S. Guo, P. Yuan, J. Zhang, P. Jin, H. Sun, K. Lei, X. Pang, Q. Xu and F. Cheng, *Chem. Commun.*, 2017, **53**, 9862-9865.

128. J. C. Li, H. Zhong, M. Xu, T. Li, L. Wang, Q. Shi, S. Feng, Z. Lyu, D. Liu and D. Du, *Sci. China Mater.*, 2019, **169**,1-7.

129. L. S. Panchakarla, K. S. Subrahmanyam, S. K. Saha, A. Govindaraj, H. R. Krishnamurthy, U. V. Waghmare and C. N. R. Rao, *Adv. Mater.*, 2009, **21**, 4726-4730.

130. D. W. Wang and D. S. Su, *Energy Environ. Sci.*, 2014, **7**, 576-591.

131. Y. Qiao, P. Yuan, Y. Hu, J. Zhang, S. Mu, J. Zhou, H. Li, H. Xia, J. He and Q. Xu, *Adv. Mater.*, 2018, **30**, e1804504.

132. C. Zhang, B. An, L. Yang, B. B. Wu, W. Shi, Y. C. Wang, L. S. Long, C. Wang and W. B. Lin, *J. Mater. Chem.*, 2016, **4**, 4457-4463.

133. J. Zhang, M. Zhang, Y. Zeng, J. Chen, L. Qiu, H. Zhou, C. Sun, Y. Yu, C. Zhu and Z. Zhu, *Small*, 2019, **15**, e1900307.

134. K. Hu, L. Tao, D. Liu, J. Huo and S. Wang, *ACS Appl. Mater. Interfaces*, 2016, **8**, 19379-19385.

135. E. G. Luo, M. L. Xiao, Y. M. Wang, J. J. Ge, C. P. Liu and W. Xing, *Chemcatchem*, 2018, **10**, 3653-3658.

136. J. C. Li, X. P. Qin, P. X. Hou, M. Cheng, C. Shi, C. Liu, H. M. Cheng and M. H. Shao, *Carbon*, 2019, **147**, 303-311.

137. T. Y. Ma, J. R. Ran, S. Dai, M. Jaroniec and S. Z. Qiao, *Angew. Chem. Int. Edit.*, 2015, **54**, 4646-4650.

138. W. Lei, Y. P. Deng, G. R. Li, Z. P. Cano, X. L. Wang, D. Luo, Y. S. Liu, D. L. Wang and Z. W. Chen, *ACS Catal.*, 2018, **8**, 2464-2472.

139. S. Guo, P. Yuan, J. Zhang, P. Jin, H. Sun, K. Lei, X. Pang, Q. Xu and F. Cheng, *Chem. Commun.*, 2017, **53**, 9862-9865.

140. M. Xiao, Y. Chen, J. Zhu, H. Zhang, X. Zhao, L. Gao, X. Wang, J. Zhao, J. Ge, Z. Jiang, S. Chen, C. Liu and W. Xing, *J. Am. Chem. Soc.*, 2019, **141**, 17763-17770.

141. K. Yuan, S. Sfaelou, M. Qiu, D. Lutzenkirchen-Hecht, X. D. Zhuang, Y. W. Chen, C. Yuan, X. L. Feng and U. Scherft, *ACS Energy Lett.*, 2018, **3**, 252-260.

142. U. Martinez, E. F. Holby, S. K. Babu, K. Artyushkova, L. Lin, S. Choudhury, G. M. Purdy and P. Zelenay, *J. Electrochem. Soc.*, 2019, **166**, F3136-F3142.

143.. E. F. Holby, G. Wu, P. Zelenay and C. D. Taylor, *J. Phys. Chem.*, 2014, **118**, 14388-14393.

144. C. H. Choi, H. K. Lim, M. W. Chung, J. C. Park, H. Shin, H. Kim and S. I. Woo, *J. Am. Chem. Soc.*, 2014, **136**, 9070-9077.

145. X. Wan, X. Liu, Y. Li, R. Yu, L. Zheng, W. Yan, H. Wang, M. Xu and J. Shui, *Nat. Catal.*, 2019, **2**, 259-268.

146. P. Chen, T. Zhou, L. Xing, K. Xu, Y. Tong, H. Xie, L. Zhang, W. Yan, W. Chu, C. Wu and Y. Xie, *Angew. Chem. Int. Ed.*, 2017, **56**, 610-614.

147. Y. F. Ye, H. B. Li, F. Cai, C. C. Yan, R. Si, S. Miao, Y. S. Li, G. X. Wang and X. H. Bao, *ACS Catal.*, 2017, **7**, 7638-7646.

148. K. Singh, F. Razmjooei and J. S. Yu, *J. Mater. Chem.*, 2017, **5**, 20095-20119.

149. E. F. Holby and C. D. Taylor, *Sci. Rep.*, 2015, **5**, 9286.

150. D. Zhang, W. Chen, Z. Li, Y. Chen, L. Zheng, Y. Gong, Q. Li, R. Shen, Y. Han and W.-C. Cheong, *Chem. Commun.*, 2018, **54**, 4274-4277.

151. X. R. Zhu, J. X. Yan, M. Gu, T. Y. Liu, Y. F. Dai, Y. H. Gu and Y. F. Li, *J. Phys. Chem. Lett.*, 2019, **10**, 7760-7766.

152. J. Wang, Z. Huang, W. Liu, C. Chang, H. Tang, Z. Li, W. Chen, C. Jia, T. Yao and S. Wei, *J. Am. Chem. Soc.*, 2017, **139**, 17281-17284.

153. X. G. Fu, Y. R. Liu, X. P. Cao, J. T. Jin, Q. Liu and J. Y. Zhang, *Appl. Catal. B: Environ.*, 2013, **130**, 143-151.

154. J. H. Reed, Y. Shi, Q. Zhu, S. Chakraborty, E. N. Mirts, I. D. Petrik, A. Bhagi-Damodaran, M. Ross, P. Moenne-Loccoz, Y. Zhang and Y. Lu, *J. Am. Chem. Soc.*, 2017, **139**, 12209-12218.

155. Y. Li, W. Zhou, H. Wang, L. Xie, Y. Liang, F. Wei, J.-C. Idrobo, S. J. Pennycook and H. Dai, *Nat. Nanotech.*, 2012, **7**, 394.

156. X. G. Fu, N. Li, B. H. Ren, G. P. Jiang, Y. R. Liu, F. M. Hassan, D. Su, J. B. Zhu, L. Yang, Z. Y. Bai, Z. P. Cano, A. P. Yu and Z. W. Chen, *Adv. Energy Mater.*, 2019, **9**, 201706758.

157. T. Ikeda, Z. F. Hou, G. L. Chai and K. Terakura, *J. Phys. Chem. C*, 2014, **118**, 17616-17625.

158. D. H. Guo, R. Shibuya, C. Akiba, S. Saji, T. Kondo and J. Nakamura, *Science*, 2016, **351**, 361-365.

159. R. Jiang, L. Li, T. Sheng, G. Hu, Y. Chen and L. Wang, *J. Am. Chem. Soc.*, 2018, **140**, 11594-11598.

160. Y. Zheng, Y. Jiao, Y. H. Zhu, Q. R. Cai, A. Vasileff, L. H. Li, Y. Han, Y. Chen and S. Z. Qiao, *J. Am. Chem. Soc.*, 2017, **139**, 3336-3339.

161. J. Wu, H. Zhou, Q. Li, M. Chen, J. Wan, N. Zhang, L. Xiong, S. Li, B. Y. Xia, G. Feng, M. Liu and L. Huang, *Adv. Energy Mater.*, 2019, **9**, 1900149.

162. H. Shen, T. Thomas, S. A. Rasaki, A. Saad, C. Hu, J. Wang and M. Yang, *Electrochem. Energy Rev.*, 2019, **2**, 252-276.

163. Z. Miao, X. Wang, M.-C. Tsai, Q. Jin, J. Liang, F. Ma, T. Wang, S. Zheng, B.-J. Hwang, Y. Huang, S. Guo and Q. Li, *Adv. Energy Mater.*, 2018, **8**, 1801226.

164. J. A. Varnell, J. S. Sotiropoulos, T. M. Brown, K. Subedi, R. T. Haasch, C. E. Schulz and A. A. Gewirth, *ACS Energy Lett.*, 2018, **3**, 823-828.

165. J. A. Varnell, E. C. Tse, C. E. Schulz, T. T. Fister, R. T. Haasch, J. Timoshenko, A. I. Frenkel and A. A. Gewirth, *Nat. Commun.*, 2016, **7**, 12582.

166. S. H. Ahn, X. Yu and A. Manthiram, *Adv. Mater.*, 2017, **29**, 1606534.

167. Y. Qu, L. Wang, Z. Li, P. Li, Q. Zhang, Y. Lin, F. Zhou, H. Wang, Z. Yang, Y. Hu, M. Zhu, X. Zhao, X. Han, C. Wang, Q. Xu, L. Gu, J. Luo, L. Zheng and Y. Wu, *Adv. Mater.*, 2019, **31**, e1904496.

168. Y. T. Qu, Z. J. Li, W. X. Chen, Y. Lin, T. W. Yuan, Z. K. Yang, C. M. Zhao, J. Wang, C. Zhao, X. Wang, F. Y. Zhou, Z. B. Zhuang, Y. Wu and Y. D. Li, *Nat. Catal.*, 2018, **1**, 781-786.

169. L. Jiao, G. Wan, R. Zhang, H. Zhou, S. H. Yu and H. L. Jiang, *Angew. Chem. Int. Edit.*, 2018, **57**, 8525-8529.

170. L. Zhao, Y. Zhang, L.-B. Huang, X.-Z. Liu, Q.-H. Zhang, C. He, Z.-Y. Wu, L.-J. Zhang, J. Wu and W. Yang, *Nat. Commun.*, 2019, **10**, 1-11.

171. S. Dilpazir, H. Y. He, Z. H. Li, M. Wang, P. L. Lu, R. J. Liu, Z. J. Xie, D. L. Gao and G. J. Zhang, *ACS Appl. Energy Mater.*, 2018, **1**, 3283-3291.

172. Y. Yang, K. Mao, S. Gao, H. Huang, G. Xia, Z. Lin, P. Jiang, C. Wang, H. Wang and Q. Chen, *Adv. Mater.*, 2018, **30**, e1801732.

173. X. Xiong, Y. Li, Y. Jia, Y. Meng, K. Sun, L. Zheng, G. Zhang, Y. Li and X. Sun, *Nanoscale*, 2019, **11**, 15900-15906.

174. G. Han, Y. Zheng, X. Zhang, Z. Wang, Y. Gong, C. Du, M. N. Banis, Y.-M. Yiu, T.-K. Sham and L. Gu, *Nano Energy*, 2019, **66**, 104088.

175. X. Lyu, G. Li, X. Chen, B. Shi, J. Liu, L. Zhuang and Y. Jia, *Small Methods*, 2019, **3**, 484.

176. C. Tang and Q. Zhang, *Adv. Mater.*, 2017, **29**, 1604103.

177. S. J. Tauster, S. C. Fung and R. L. Garten, *J. Am. Chem. Soc.*, 1978, **100**, 170-175.

178. W. Wei, X. Shi, P. Gao, S. Wang, W. Hu, X. Zhao, Y. Ni, X. Xu, Y. Xu, W. Yan, H. Ji and M. Cao, *Nano Energy*, 2018, **52**, 29-37.

179. X. Han, X. Ling, Y. Wang, T. Ma, C. Zhong, W. Hu and Y. Deng, *Angew. Chem. Int. Ed.*, 2019, **58**, 5359-5364.

180. S. Mukherjee, D. A. Cullen, S. Karakalos, K. Liu, H. Zhang, S. Zhao, H. Xu, K. L. More, G. Wang and G. Wu, *Nano Energy*, 2018, **48**, 217-226.

181. G. Wu, K. L. More, C. M. Johnston and P. Zelenay, *Science*, 2011, **332**, 443-447.

182. J. Woo, S. Y. Yang, Y. J. Sa, W. Y. Choi, M. H. Lee, H. W. Lee, T. J. Shin, T. Y. Kim and S. H. Joo, *Chem. Mater.*, 2018, **30**, 6684-6701.

183. L. Shang, H. Yu, X. Huang, T. Bian, R. Shi, Y. Zhao, G. I. Waterhouse, L. Z. Wu, C. H. Tung and T. Zhang, *Adv. Mater.*, 2016, **28**, 1668-1674.

184. Q. Liu, X. Liu, L. Zheng and J. Shui, *Angew. Chem. Int. Ed.*, 2018, **57**, 1204-1208.

185. I. S. Amiinu, Liu, X. B., Pu, Z. H., Li, W. Q., Li, Q. D., Zhang, J., Tang, H. L., Zhang, H. N., Mu, S. C., *Adv. Energy Mater.*, 2017, **28**, 1704638.

186. V. Yarlagadda, M. K. Carpenter, T. E. Moylan, R. S. Kukreja, R. Koestner, W. Gu, L. Thompson and A. Kongkanand, *ACS Energy Lett.*, 2018, **3**, 618-621.

187. S. H. Lee, J. Kim, D. Y. Chung, J. M. Yoo, H. S. Lee, M. J. Kim, B. S. Mun, S. G. Kwon, Y. E. Sung and T. Hyeon, *J. Am. Chem. Soc.*, 2019, **141**, 2035-2045.

188. B. W. Wang, X. X. Wang, J. X. Zou, Y. C. Yan, S. H. Xie, G. Z. Hu, Y. G. Li, A. G. Dong, *Nano Letters*, 2017, **17**, 2003-2009.

189. G. W. Sun, J. T. Wang, X. J. Liu, D. H. Long, W. M. Qiao and L. H. Ling, *J. Phys. Chem. C*, 2010, **114**, 18745-18751.

190. T. Sun, S. Zhao, W. Chen, D. Zhai, J. Dong, Y. Wang, S. Zhang, A. Han, L. Gu, R. Yu, X. Wen, H. Ren, L. Xu, C. Chen, Q. Peng, D. Wang and Y. Li, *Proc. Natl. Acad. Sci. U. S. A.*, 2018, **115**, 12692-12697.

191. W. Zhang, Z. Y. Wu , H. L. Jiang, S. H. Yu, *J. Am. Chem. Soc.*, 2014, **136**, 14385-14388.

192. A. Kong, X. Zhu, Z. Han, Y. Yu, Y. Zhang, B. Dong and Y. Shan, *ACS Catal.*, 2014, **4**, 1793-1800.

193. C. H. Wang, H. C. Huang, S. T. Chang, Y. C. Lin and M. F. Huang, *RSC Adv.*, 2014, **4**, 4207-4211.

194. H. T. Chung, G. Wu, Q. Li and P. Zelenay, *Int. J. Hydrog. Energy*, 2014, **39**, 15887-15893

195. M. P. Karthikayini, T. Thirupathi, G. Wang, V. K. Ramani and R. K. Raman, *J. Electrochem. Soc.*, 2016, **163**, F539-F547.

196. L. Chong, G. A. Goenaga, K. Williams, H. M. Barkholtz, L. R. Grabstanowicz, J. A. Brooksbank, A. B. Papandrew, R. Elzein, R. Schlaf and T. A. Zawodzinski, *ChemElectroChem*, 2016, **3**, 1541-1545.

197. X. X. Wang, D. A. Cullen, Y. T. Pan, S. Hwang, M. Wang, Z. Feng, J. Wang, M. H. Engelhard, H. Zhang and Y. He, *Adv. Mater.*, 2018, **30**, 1706758.

198. Y. Li, X. Liu, L. Zheng, J. Shang, X. Wan, R. Hu, X. Guo, S. Hong and J. Shui, *J. Mater. Chem.*, 2019, **7**, 26147-26153.

199. X. Fu, F. M. Hassan, P. Zamani, G. Jiang, D. C. Higgins, J.-Y. Choi, X. Wang, P. Xu, Y. Liu and Z. Chen, *Nano Energy*, 2017, **42**, 249-256.

200. X. Wan, X. Liu, Y. Li, R. Yu, L. Zheng, W. Yan, H. Wang, M. Xu and J. Shui, *Nat. Catal.*, 2019, **2**, 259-268.

201. J. H. Zagal, F. Bedioui and J.-P. Dodelet, *N_4-macrocyclic metal complexes*, Springer, New York, 2007.

202. G. Goenaga, S. Q. Ma, S. W. Yuan and D. J. Liu, *ECS Trans.*, 2010, **33**, 579-586.

203. L. Yang, N. Larouche, R. Chenitz, G. Zhang, M. Lefèvre and J. P. Dodelet, *Electrochim. Acta*, 2015, **159**, 184-197.

204. J. Shui, C. Chen, L. Grabstanowicz, D. Zhao and D. J. Liu, *PANS*, 2015, **112**, 10629-10634.

205. Y. Mun, M. J. Kim, S.-A. Park, E. Lee, Y. Ye, S. Lee, Y.-T. Kim, S. Kim, O.-H. Kim and Y.-H. Cho, *Appl. Catal. B: Environ.*, 2018, **222**, 191-199.

206. M. Rauf, J.-W. Wang, P. Zhang, W. Iqbal, J. Qu and Y. Li, *J. Power Sources*, 2018, **408**, 17-27.

207. Q. Cheng, S. Han, K. Mao, C. Chen, L. Yang, Z. Zou, M. Gu, Z. Hu and H. Yang, *Nano Energy*, 2018, **52**, 485-493.

208. A. Serov, K. Artyushkova and P. Atanassov, *Adv. Energy Mater.*, 2014, **4**, 1301735.

209. A. Serov, M. H. Robson, M. Smolnik and P. Atanassov, *Electrochim. Acta*, 2012, **80**, 213-218.

210. A. Serov, M. J. Workman, K. Artyushkova, P. Atanassov, G. McCool, S. McKinney, H. Romero, B. Halevi and T. Stephenson, *J. Power Sources*, 2016, **327**, 557-564.

211. M. J. Workman, A. Serov, L.-k. Tsui, P. Atanassov and K. Artyushkova, *ACS Energy Lett.*, 2017, **2**, 1489-1493.

212. Y. F. Zhan, H. B. Zeng, F. Y. Xie, H. Zhang, W. H. Zhang, Y. S. Jin, Y. L. Zhang, J. Chen, H. Meng, *J. Power Sources*, 2019, **431**, 31-39.

213. Q. Li, G. Wu, D. A. Cullen, K. L. More, N. H. Mack, H. T. Chung and P. Zelenay, *ACS Catal.*, 2014, **4**, 3193-3200.

214. G. Wu, A. Santandreu, W. Kellogg, S. Gupta, O. Ogoke, H. Zhang, H.-L. Wang and L. Dai, *Nano Energy*, 2016, **29**, 83-110.

215. P. Zelenay, *2017 U.S. DOE Annual Merit Review and Peer Evaluation Meeting*, 2017, https://www.hydrogen.energy.gov/pdfs/review17/fc160_zelenay_2017_o.pdf.

216. H. T. Chung, C. M. Johnston, K. Artyushkova, M. Ferrandon, D. J. Myers and P. Zelenay, *Electrochem. Commun.*, 2010, **12**, 1792-1795.

217. H. T. Chung, J. H. Won and P. Zelenay, *Nat. Commun.*, 2013, **4**, 1922.

218. A. Uddin, L. Dunsmore, H. G. Zhang, L. M. Hu, G. Wu and S. Litster, *ACS Appl. Mater. Interfaces*, 2020, **12**, 2216-2224.

219. D. Banham, J. Y. Choi, T. Kishimoto and S. Ye, *Adv. Mater.*, 2019, 1804846.

220. S. Litster and G. McLean, *J. Power Sources*, 2004, **130**, 61-76.

221. S. Stariha, K. Artyushkova, M. J. Workman, A. Serov, S. McKinney, B. Halevi and P. Atanassov, *J. Power Sources*, 2016, **326**, 43-49.

222. J.-Y. Choi, L. Yang, T. Kishimoto, X. Fu, S. Ye, Z. Chen and D. Banham, *Energy Environ. Sci.*, 2017, **10**, 296-305.

223. T. Kishimoto, T. Sato, Y. Kobayashi, K. Narizuka, D. Banham, Y. Zhou, E. Marquez, K. Bai and S. Ye, *Meeting Abstracts*, 2016, **MA2016-02**, 2824.

224. X. Yin, L. Lin, H. T. Chung, S. K. Babu, U. Martinez, G. M. Purdy and P. Zelenay, *ECS Tran.*, 2017, **77**, 1273-1281.

225. G. Wu and P. Zelenay, presented in part at *the 2009 Fuel Cell Seminar & Exposition*, Palm Spring, CA, 2009.

226. G. Wu, C. Dai, D. Wang, D. Li and N. Li, *J. Mater. Chem.*, 2010, **20**, 3059-3068.

227. S. K. Babu, H. T. Chung, P. Zelenay, S. Litster, *ACS Appl. Mater. Interfaces*, 2016, **8**, 32764-32777.

228. S. K. Babu, H. T. Chung, P. Zelenay and S. Litster, *ECS Trans.*, 2015, **69**, 23-33.

229. S. Stariha, K. Artyushkova, A. Serov and P. Atanassov, *Inter. J. Hydrogen Energy*, 2015, **40**, 14676-14682.

230. X. Yin, L. Lin, H. T. Chung, S. K. Babu, U. Martinez, G. M. Purdy and P. Zelenay, Selected Proceedings from the 231st ECS Meeting, 2017, **77**, 1273-1281.

231. D. Malko, T. Lopes, E. A. Ticianelli and A. Kucernak, *J. Power Sources*, 2016, **323**, 189-200.

232. R. Makharia, M. F. Mathias and D. R. Baker, *J. Electrochem. Soc.*, 2005, **152**, A970-A977.

233. S. Komini Babu, H. T. Chung, P. Zelenay and S. Litster, *ACS Appl. Mater. Interfaces*, 2016, **8**, 32764-32777.

234. S. Komini Babu, H. T. Chung, P. Zelenay and S. Litster, *ECS Trans.*, 2015, **69**, 23-33.

235. S. Ogawa, S. Komini Babu, H. T. Chung, P. Zelenay and S. Litster, *ECS Trans.*, 2016, **75**, 139-146.

236. S. Komini Babu, H. T. Chung, G. Wu, P. Zelenay and S. Litster, *ECS Trans.*, 2014, **64**, 281-292.

237. Y. C. Wang, L. Huang, P. Zhang, Y. T. Qiu, T. Sheng, Z. Y. Zhou, G. Wang, J. G. Liu, M. Rauf, Z. Q. Gu, W. T. Wu and S. G. Sun, *ACS Energy Lett.*, 2017, **2**, 645-650.

238. Y. C. Wang, P. F. Zhu, H. Yang, L. Huang, Q. H. Wu, M. Rauf, J. Y. Zhang, J. Dong, K. Wang, Z. Y. Zhou and S. G. Sun, *Chemelectrochem.*, 2018, **5**, 1914-1921.

239. M. Sansotera, M. Bianchi, G. Lecardi, G. Marchionni, P. Metrangolo, G. Resnati, W. Navarrini, *Chem. Mater.*, 2009, **21**, 4498-4504.

240. D. D. Do, H. D. Do, *Carbon*, 2000, **38**, 767-773.

241. Y. Tabe, Y. Aoyama, K. Kadowaki, K. Suzuki and T. Chikahisa, *J. Power Sources*, 2015, **287**, 422-430.

242. S. Ismadji and S. K. Bhatia, *Langmuir*, 2001, **17**, 1488-1498.

243. C. Y. Wang, *Chem. Rev.*, 2004, **104**, 4727-4765.

244. J. Slack, B. Halevi, G. McCool, J. Li, R. Pavlicek, R. Wycisk, S. Mukerjee and P. Pintauro, *ChemElectroChem*, 2018, **5**, 1537-1542.

245. J. M. Lee, H. Han, S. Jin, S. M. Choi, H. J. Kim, M. H. Seo and W. B. Kim, *Energy Technol.*, 2019, **7**, 1900312.

246. R. Pavlicek, S. C. Barton, N. Leonard, H. Romero, S. McKinney, G. McCool, A. Serov, D. Abbott, P. Atanassov and S. Mukerjee, *J. Electrochem. Soc.*, 2018, **165**, F589-F596.

247. L. Chen, G. Wu, E. F. Holby, P. Zelenay, W.-Q. Tao and Q. Kang, *Electrochim. Acta*, 2015, **158**, 175-186.

248. S. K. Babu, H. T. Chung, G. Wu, P. Zelenay and S. Litster, *ECS Trans.*, 2014, **64**, 281-292.

249. S. Ogawa, S. K. Babu, H. Chung, P. Zelenay and S. Litster, *ECS Trans.*, 2016, **75**, 139-146.

250. D. Bokach, S. ten Hoopen, N. Muthuswamy, M. E. M. Buan and M. Rønning, *Inter. J. Hydrogen Energy*, 2016, **41**, 17616-17630.

251. H. Schulenburg, S. Stankov, V. Schünemann, J. Radnik, I. Dorbandt, S. Fiechter, P. Bogdanoff and H. Tributsch, *J. Phys. Chem. B*, 2003, **107**, 9034-9041.

252. M. Ferrandon, X. Wang, A. J. Kropf, D. J. Myers, G. Wu, C. M. Johnston and P. Zelenay, *Electrochim. Acta*, 2013, **110**, 282-291.

253. G. Wu, K. Artyushkova, M. Ferrandon, A. J. Kropf, D. Myers and P. Zelenay, *ECS Trans.*, 2009, **25**, 1299-1311.

254. P. Xu, UWSPACE, 2019.

255. V. Goellner, V. Armel, A. Zitolo, E. Fonda, F. Jaouen, *J. Electrochem. Soc.*, 2015, **162**, H403-H414.

256. M. Lefèvre, J. P. Dodelet, *Electrochim. Acta*, 2003, **48**, 2749-2760.

257. C. H. Choi, H. K. Lim, M. W. Chung, G. Chon, N. R. Sahraie, A. Altin, M. T. Sougrati, L. Stievano, H. S. Oh, E. S. Park, F. Luo, P. Strasser, G. Drazic, K. J. J. Mayrhofer, H. Kim, F. Jaouen, *Energy Environ. Sci.*, 2018, **11**, 3176-3182.

258. H. L. Guo, X. F. Wang, Q. Y. Qian, F. B. Wang. X. H. Xia, *ACS Nano*, 2009, **3**, 2653-2659.

259. S. Cruz-Manzo, R. Chen, P. Rama, *Int. J. Hydrogen Energy*, 2013, **38**, 1702-1731.

260. S. Rasouli, R. A. Ortiz Godoy, Z. Yang, M. Gummalla, S. C. Ball, D. Myers, P. J.,Ferreira, *J. Power Sources*, 2017, **343**, 571-579.

261. P. Zelenay, *2017 Annual Merit Review and Peer Evaluation Meeting (AMR)*, 2017.

262. Z. Meng, S. Cai, R. Wang, H. Tang, S. Song and P. Tsiakaras, *Appl. Catal. B: Environ.*, 2019, **244**, 120-127.

263. H. Yang, X. Chen, W. T. Chen, Q. Wang, N. C. Cuello, A. Nafady, A. M. Al-Enizi, G. I. N. Waterhouse, G. A. Goenaga, T. A. Zawodzinski, P. E. Kruger, J. E. Clements, J. Zhang, H. Tian, S. G. Telfer and S. Ma, *ACS Nano*, 2019, **13**, 8087-8098.

264. H. W. Wei, X. G. Su, J. G. Liu, J. Tian, Z. W. Wang, K. Sun, Z. Y. Rui, W. W. Yang and Z. G. Zou, *Electrochem. Commun.*, 2018, **88**, 19-23.

265. L. Gubler, W. H. Koppenol, *J. Electrochem. Soc.*, 2011, **159**, B211-B218.

266. L. Zhang, J. J. Zhang, D. P. Wilkinson, H. J. Wang, *J. Power Sources*, 2006, **156**, 171-182.

267. S. Baranton, C. Coutanceau, C. Roux, F. Hahn, J.-M. Leger, *J. Electroanaly. Chem.*, 2005, **577**, 223-234.

268. C. H. Choi, C. Baldizzone, G. Polymeros, E. Pizzutilo, O. Kasian, A. K. Schuppert, N. Ranjbar Sahraie, M.-T. Sougrati, K. J. Mayrhofer and F. d. r. Jaouen, *ACS Catal.*, 2016, **6**, 3136-3146.

269. J. Chen, X. Yan, C. Fu, Y. Feng, C. Lin, X. Li, S. Shen, C. Ke, J. Zhang, *ACS Appl. Mater. Interfaces*, 2019, **11**, 37779-37786.

270. B. Kienitz, Pivovar, B., Zawodzinski, T.,Garzon, F. H. , *J. Electrochem. Soc.*, 2011, **158**, B1175- B1183.

271. T. Okada, Y. Ayato, H. Satou, M. Yuasa, I. Sekine, *J. Phys. Chem. B*, 2001, **105**, 6980-6986.

272. T. Ha, J. Cho, J. Park, K. Min, H.-S. Kim, E. Lee and J.-Y. Jyoung, *Inter. J. Hydrogen Energy*, 2011, **36**, 12436-12443.

273. V. Goellner, C. Baldizzone, A. Schuppert, M. T. Sougrati, K. Mayrhofer and F. Jaouen, *Phys. Chem. Chem. Phys.*, 2014, **16**, 18454-18462.

274. G. Wu, K. L. More, P. Xu, H.-L. Wang, M. Ferrandon, A. J. Kropf, D. J. Myers, S. Ma, C. M. Johnston and P. Zelenay, *Chem. Commun.*, 2013, **49**, 3291-3293.

275. P. Zamani, D. C. Higgins, F. M. Hassan, X. Fu, J.-Y. Choi, M. A. Hoque, G. Jiang and Z. Chen, *Nano Energy*, 2016, **26**, 267-275.

276. D. Xia, X. Yang, L. Xie, Y. Wei, W. Jiang, M. Dou, X. Li, J. Li, L. Gan and F. Kang, *Adv. Funct. Mater.*, 2019, **29**, 1906174.

277. X. Wang, Q. Li, H. Pan, Y. Lin, Y. Ke, H. Sheng, M. T. Swihart and G. Wu, *Nanoscale*, 2015, **7**, 20290-20298.

278. Y. Yu, H. Li, H. Wang, X.-Z. Yuan, G. Wang and M. U. Pan, *J. Power Sources*, 2012, **205**, 10-23.

279. T. Mittermeier, A. Weiß, F. Hasché, G. Hübner and H. A. Gasteiger, *J. Electrochem. Soc.*, 2017, **164**, F127-F137.

280. H. Li, Y. Tang, Z. Wang, Z. Shi, S. Wu, D. Song, J. Zhang, K. Fatih, J. Zhang and H. Wang, *J. Power Sources*, 2008, **178**, 103-117.

281. T. Wang, Q. Zhao, Y. Fu, C. Lei, B. Yang, Z. Li, L. Lei, G. Wu and Y. Hou, *Small Methods*, 2019, **3**, 1900210.

282. Y. Li, X. Li, H. S. Pillai, J. Lattimer, N. Mohd Adli, S. Karakalos, M. Chen, L. Guo, H. Xu, J. Yang, D. Su, H. Xin and G. Wu, *ACS Catal.*, 2020, **10**, 3945-3957.

283. X. X. Wang, J. Sokolowski, H. Liu and G. Wu, Chin. J. Catal., 2020, **41**, 739-755.

284. M. D. Hossain, Z. Liu, M. Zhuang, X. Yan, G.-L. Xu, C. A. Gadre, A. Tyagi, I. H. Abidi, C.-J. Sun, H. Wong, A. Guda, Y. Hao, X. Pan, K. Amine and Z. Luo, *Adv. Energy Mater.*, 2019, **9**, 1803689.

285. K. Ithisuphalap, H. Zhang, L. Guo, Q. Yang, H. Yang and G. Wu, *Small Methods*, 2019, **3**, 1800352.

286. H. Xu, K. Ithisuphalap, Y. Li, S. Mukherjee, J. Lattimer, G. Soloveichik and G. Wu, *Nano Energy*, 2020, **69**, 104469.

TOC

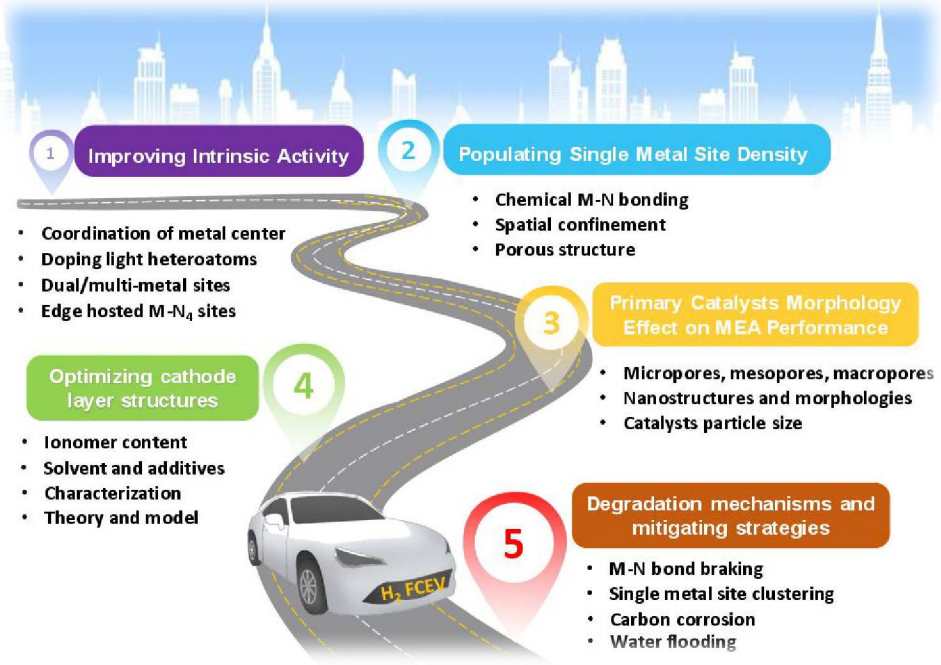

The review provides a comprehensive understanding of the atomically dispersed metal-nitrogen-carbon cathode catalysts for proton-exchange membrane fuel cell applications